Photovoltaic Module Characterization and Detection of Deterioration by using the Current and Voltage at Maximum Power Point for Module and System Performance Analysis

September 2021

MANIT SEAPAN

Photovoltaic Module Characterization and Detection of Deterioration by using the Current and Voltage at Maximum Power Point for Module and System Performance Analysis

Graduate School of Systems and Information Engineering
University of Tsukuba

September 2021

MANIT SEAPAN

Contents

Chapter 1

Introduction

1.1 Energy Resources and Global Energy Trends

The World Energy Outlook 2020 (WEO2020) Reported presented the Stated Policies Scenario (STEPS), the Delayed Recovery Scenario (DRS) which has deeper and more lasting economic and social impacts, the Sustainable Development Scenario (SDS), and the Net Zero Emissions by 2050 (NZE2050) Scenario, which was explored for the first time in the report [1]. The immediate effects of the Covid-19 pandemic on the energy system during 2020 are shown by falls of 5 % and 18 % in global energy demand and energy investment, respectively. A continuation of the current growth trends would raise overall demand. Renewable energy is expected to continue growing in all scenarios. All types of fuels, except coal and traditional–use biomass, will be required to meet demand growth, with the lead being taken by renewables.

The development of renewable sources is more striking; here, the annual capacity additions of solar photovoltaics (PVs) take place at double the peace of the last four years through to 2025 and to keep rising into 2030. However, demand for all sources of energy, except coal, continues to increase. The contrast between solar PVs and coal is stark, as shown in Fig. 1.1. Over the next decade, the share of coal in the global generation will fall. This rise of renewables which solar PV is the new king, as reported.

Solar PV capacities have been helped by its lower costs compared to traditional power plants in most markets; furthermore, it can be installed rapidly. Global manufacturing of solar modules has also proven that this technology can be rapidly scaled up, and its currently capacity is about 160 GW of available capacity. Some of the largest increases in PV installations can be seen in China, India, Southeast Asia, and the United States. All of these countries will very soon surpass their record annual PV capacity additions for 2030, as shown in Fig. 1.2. The installed capacity of solar PV worldwide is expected to increases by nearly 20 % each year from 2019 to 2030, as reported in NZE2050.

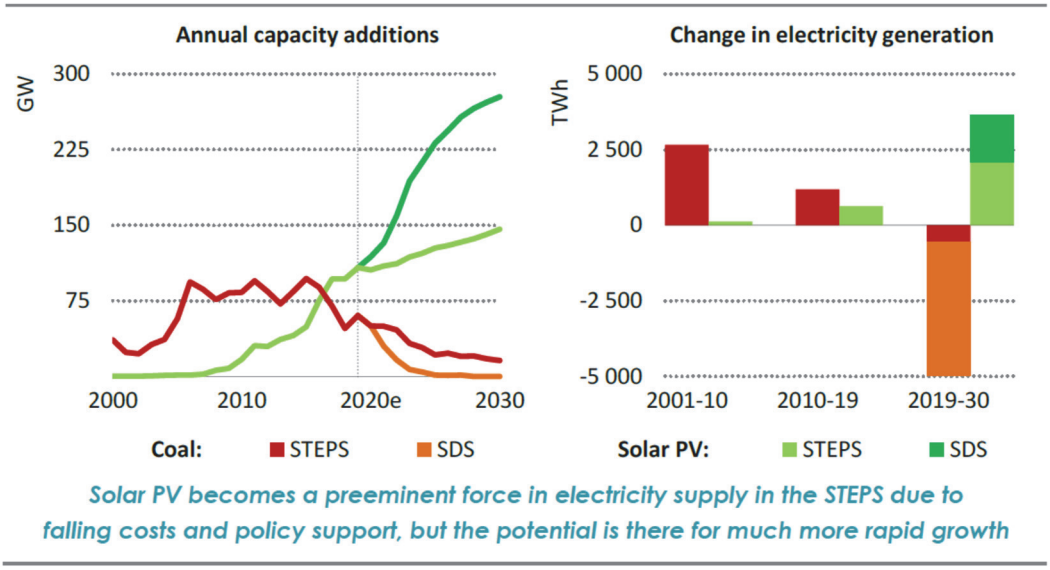

Note: 2020e = estimated values for 2020.

Figure 1.1. Average annual solar PV and coal capacity additions worldwide, and electricity generation by scenario [1].

Renewables and nuclear power, when combined, generated more electricity than coal for the first time in 2019 and are on track to open a permanent lead, as shown in Fig. 1.3. Electricity generation from renewables is set to overtake that from coal–fired power plants by 2025, with solar PV and wind power spearheading growth, aided by falling costs, widespread resource availability, and strong policy support; 166 countries now have targets for renewable power generation [2].

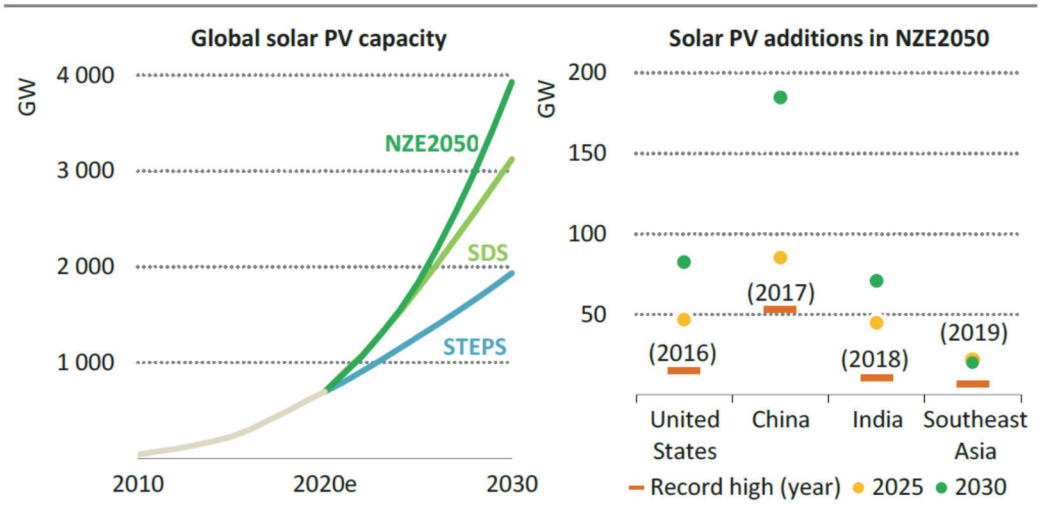

Note: 2020e = estimated values for 2020.

Figure 1.2. Globally installed PV capacity by scenario (2010 – 2030), and annual PV capacity additions in the NZE2050 [1].

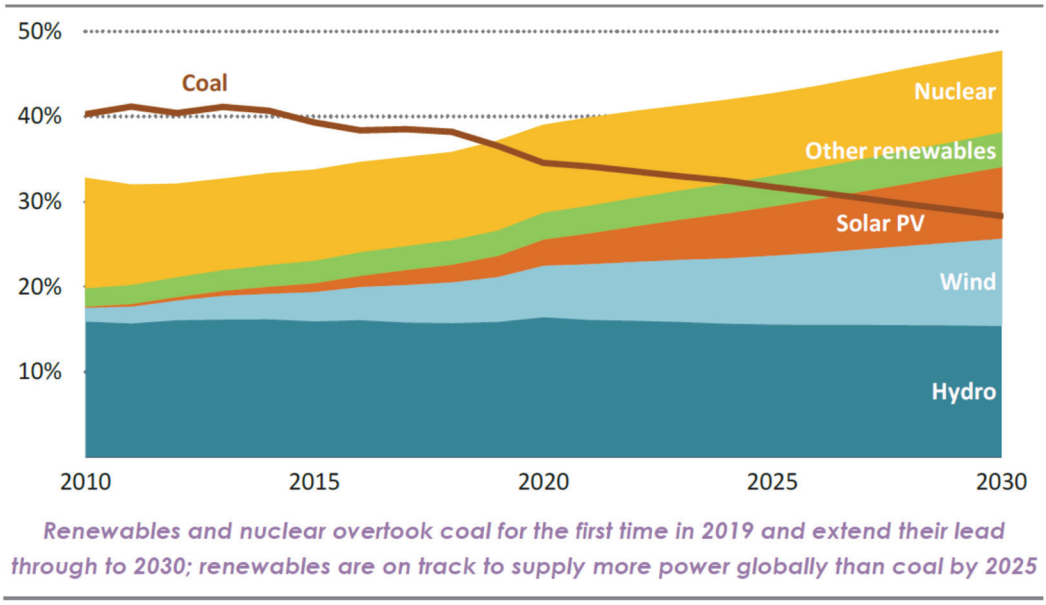

Figure 1.3. Renewables' shares of global electricity supply in the State Policies Scenario (2010 – 2030) [1].

1.2 Climate Change and Greenhouse Gasses

Climate change has become a major concern of the present century. The urgent response to that concern involves an energy transformation that swiftly reduces the carbon emissions that responsible for climate change. The Paris Agreement establishes a clear goal: to limit the increase of global temperature to "well below" 2 degrees Celsius (°C) and ideally to 1.5 °C compared to pre–industrial levels, and to do so during this century [2]. To realize this climate target, a profound transformation of the global energy landscape is required. Rapidly shifting the world away from the consumption of fossil–fuels and towards cleaner renewable forms of energy is critical to reach the climate goals agreed upon in Paris. Such a transformation is possible with the rapid replacement of conventional fossil–fuel generation and uses with low–carbon technologies. Decarbonizing the energy sector and reducing carbon emissions present key objectives in energy transformation roadmaps of the International Renewable Energy Agency (IRENA), which examines and provides an ambitious, yet technically and economically feasible, pathway for the deployment of low–carbon technologies towards a more sustainable clean energy future. However, the reduction of carbon emissions is not the only reason why the world should embrace the energy transformation.

The European Union is currently following a pathway towards greenhouse gas **(**GHG) reduction of 46 % by 2030 [3]. In order to increase the ambition towards 55 % GHG reduction by 2030. However, they only analyzed the need for additional PV power capacity, whereas realizing these golds will need accompanying measures such as additional electricity storage, power–demand and supply management, as well as complementing renewable electricity generation capacities from wind or biomass. The different decarbonization scenarios predicted to realize a 55 % GHG reduction require the installation of new PV capacities of between 325 and 375 GW_{DC} within the timeframe of 2020 – 2030. The PV market volume in the EU would have to grow between 3 – 5 times compared to its 2019 level to achieve this goal. Furthermore, these values could almost double if the electricity demand rises faster than currently projected.

1.3 Photovoltaic Trends

Photovoltaic (PV) continues to be a fast–growing market, with expected growth global installations. On a global basis, the total installation of PV power capacity at the end of 2020 was reported to exceed 760.4 GW_{DC} [4]. The International Energy Agency Photovoltaic Power Systems Programme (IEA-

PVPS T1-39, 2021) reports the cumulative installation capacity at the end 2020 represented which the leader totaled capacity installation is China reached to with 253.4 GW, followed by the European Union 151.3 GW, the USA 93.2 GW, Japan 71.4 GW, Germany 53.9 GW, and India 47.4 GW. In the European Union, Germany leads with 53.9 GW, follow by Italy 21.7 GW. PV contribution in the world totally amounts to close to 3.7 % of electricity demand. Australia had the highest installed PV capacity per capita in 2020 at 795 Watts/capita, followed by the Germany at 649 Watts/capita, and Japan ranks third at 565 Watts/capita. PV cell technologies are currently being developed in wafer–based, thin–film, and organic. However, wafer–based crystalline–silicon (c–Si) technology tack up the biggest market share for more than 96 % of overall PV module production in 2019 [5]. Silicon features a bandgap within the optimal range for efficient PV conversion, is the second most abundant material in the earth's crust (after oxygen). It is nontoxic and its technology is well mastered by chemical and semiconductor industrials [6, 7].

1.4 Scope of the Problem

The analysis of PV module lifetimes is important, because it impact the system's reliability, and service lifetime performance. Thus, fast data analysis techniques are required, to detect deteriorations and failures that might affect energy production is needed. This can help to reduce the severe effect on the payback period if the fault PV modules are replaced. The PV electricity production cost is reduced. The lifetime output is increased by improving the reliability, service lifetime performance, and system data analysis procedures.

Photovoltaic installations continue to be growth as aforementioned. The analysis of PV module lifetimes is also important because it impact the system's reliability and service lifetime performance. Reliability of a PV module means that it performs the promised productions for the expected lifetime. The promised function is the continued safe production of a specified amount of electricity. Typically, the PV module warranty the amount of power output retained of 80 % of the initial power, and the time period should retain this amount of power, often 25 years. The degradation rate is an essential factor used in evaluating potential financial payback from investment in the PV system. Investors want to know what degradation rate they can expect from their module type they purchased. The PV modules must be durable, because they are exposed to the stresses of the outdoor environment. The durability focuses on maintaining the output power level. Temperature and irradiance are among the influential factors on the performance of PV devices, which mainly affect their output voltage and output current of the PV devices. Usually, PV systems operate under various temperatures and irradiances. On the

other hand, the module specifications are usually defined at the standard test condition (STC) as follows: irradiance of 1 kW/m^2, air mass 1.5, and module temperature of 25 °C (IEC 60904-3, 2016) [8], and PV test–report usually report the performance at STC. Various kinds of mathematical models for the temperature and irradiance dependences of the current–voltage characteristics (*I–V* curves) and performance parameters of PV modules have been discussed so far [9-14]. They proposed novel models of the *I–V* curves, and used this to extract the performance parameters from the experimental curves, and predicted the *I–V* curves and maximum powers (P_{max}) under various temperature and irradiance conditions. For example, model parameter values extracted using statistical non-linear fit (SNF) were presented by Zaimi et al [13]. A plot of *I–V* experimental characteristics versus SNF method of extraction for poly–crystalline PV module at STC is shown in Fig 1.4.

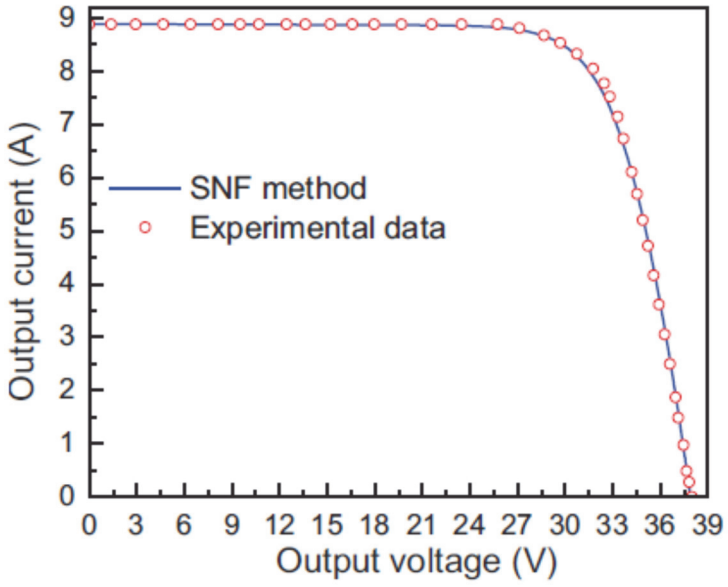

Figure 1.4. *I–V* experimental and SNF optimized method characteristics of PV module at STC [13].

The translation equations have also been analyzed by using numerical fitting of the parameters based on numerous outdoor data were also studied [15-21]. For example, King B.H. et al. [17] discussed a procedure for determining coefficients in the performance model. They conducted experiments under various temperature ranges for voltage at maximum power (V_{mp}) and current at maximum power (I_{mp}) to refine the parameter–fittings, expressed as

$$V_{\mathrm{mp}} = V_{\mathrm{mp0}} + C_2 N_{\mathrm{c}} \frac{nkT_{\mathrm{c}}}{q} \ln(E_{\mathrm{e}}) + C_3 N_{\mathrm{c}} [\frac{nkT_{\mathrm{c}}}{q} \ln(E_{\mathrm{e}})]^2 + \beta_{V_{\mathrm{mp}}} [T_{\mathrm{c}} - T_0], \quad (1.1)$$

$$I_{\mathrm{mp}} = I_{\mathrm{mp0}} [C_0 E_e + C_1 E_{\mathrm{e}}^2] \left[1 + \hat{a}_{I\mathrm{mp}} [T_{\mathrm{c}} - T_0]\right], \quad (1.2)$$

Here, T_0 is the temperature for reporting, typically 25 °C, T_{c} is the cell temperature, V_{mp0} is the value of V_{mp} at T_0, E_{e} is the effective irradiance, C_2 and C_3 are coefficients relating E_{e} to V_{mp}, N_{c} is the number of series–connected cells, and β_{Vmp} is the temperature coefficient of V_{mp}. I_{mp0} is the reference current at maximum power at T_0, C_0 and C_1 are coefficients relating E_{e} to I_{mp}, and $\hat{a}_{I\mathrm{mp}}$ is the temperature coefficient (TC) for I_{mp}.

During PV operation, the PV output voltage varies over a wide range during operation due to stage changing such as temperature, irradiance, and cells/modules connection. The controller's setpoint value can be used to track the actual maximum power point (MPP), by using an appropriate searching strategy for MPP tracking (MPPT). During the PV systems' MPPT operations, only the current at maximum power (I_{mp}) and the voltage at maximum power (V_{mp}) are measurable. Because the I_{mp} and V_{mp} are dependent on the module temperature and irradiance, translation equations for them are necessary for characterizing the performance of PV devices under MPPT operation. Previous studies [22-27] discussed I_{mp} and V_{mp}, based on the experimental results of the *I–V* curve. However, it requires a set of *I–V* curves under different irradiance (*G*) maintaining temperature (*T*) and under different *T* maintaining *G* to compute the correction parameters. Furthermore, they also required experimental *I–V* curves and the TCs of the short–circuit current (I_{sc}), open–circuit voltage (V_{oc}), and other correction factors. Recently, a novel formula for temperature translation was proposed by Hishikawa et al., 2018 [26]. It proposed the TCs of the *I–V* curves of PV devices as a function of temperature and voltage based on the one–diode model. Recently, a methodology called the Suns–Vmp method was proposed [28, 29], this enabled the monitoring and diagnosis of PV system degradation using only the values at the MPP. However, it requires datasheet information for the initial values. It requires the extraction of diode parameters by using numerical fitting in order to evaluate their performance, and also required data accumulation.

As mentioned above, there are previous conventional methodologies to characterize the PV module performance and reliability. Detection failures, degradation, and deterioration are essential for protecting against PV production problems, operation outages, and low productivity. This study presents a method for characterizing PV cells/modules without interrupting the PV module's operation. During PV modules' MPPT operations, measured data can be used to detect PV cell/module failures or

deterioration. The measured V_{mp} and I_{mp} value are used to correct at least for temperature. Thus, new formulas for temperature correction for V_{mp} and I_{mp} are developed for the proposed characterization. Next, a case study of detection failures and deterioration is presented by using the new formulas and I_{mp}–V_{mp} curve. The scope of the problem is depicted in Fig. 1.5, which shows the precise PV module performance characterization and detection of degradation or failures of this research compared with conventional methodologies.

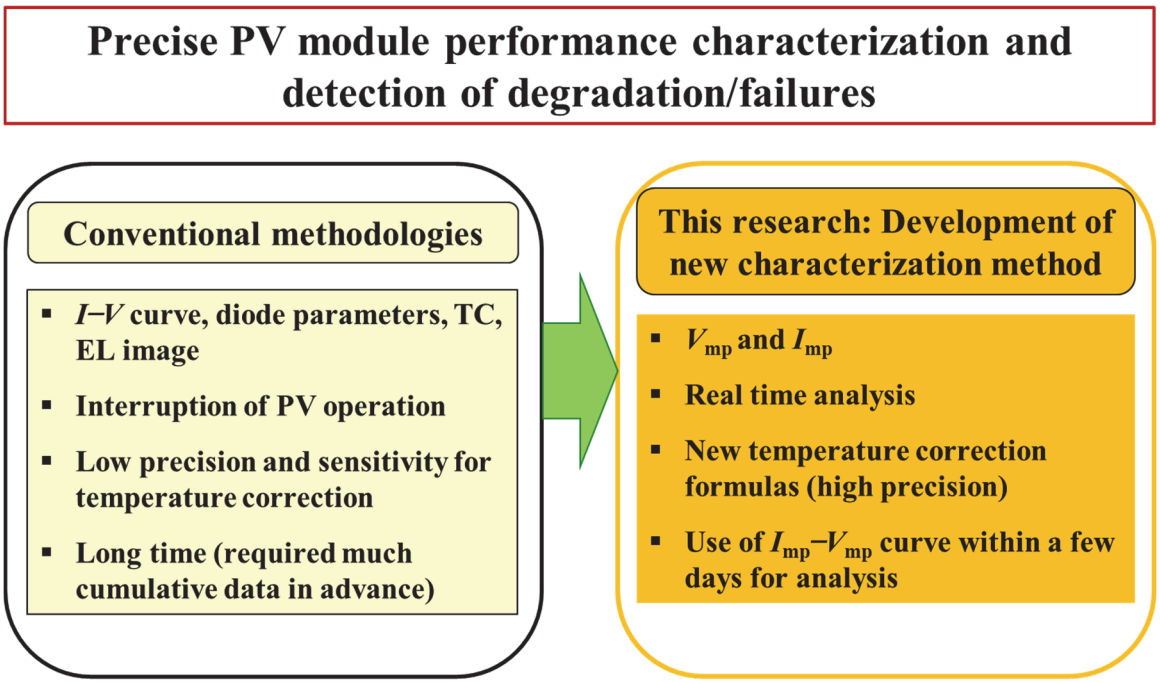

Figure 1.5. Research scope and problem and research flow chart.

1.5 Research Framework

The output of PV devices is affected by many factors such as the irradiance, temperature and shading, as well as degradation. The detection of PV module degradation is important, because degradation reduces the PV module's efficiency. Many techniques have been used to identify PV degradations, such as *I–V* curve measurements, infrared thermography, and electroluminescence (EL) images [30, 31]. Although the approach based on the *I–V* curves and *P–V* curves is useful for

determining the performance of the PV module and system, there is disadvantage that the *I–V* curve measurements interrupt the system's MPPT operation. Recently, a methodology called Suns–Vmp was proposed [28, 29], which enabled monitoring and diagnosis of PV system degradation using only the values obtained at the MPP. However, this method requires datasheet information for the initial values, and diode parameters must be extracted by numerical fitting in order to evaluate their performance.

This study analytically and experimentally investigated expressions for the temperature and irradiance dependences of I_{mp} and V_{mp} of commercial crystalline–silicon PV devices, without the need for parameter fitting. New formulas for the temperature correction of experimental V_{mp} data are investigated. The novelty of the present study is that these formulas do not require advance information of TC, diode parameters, or *I–V* curve parameters. The results lead to translation of the I_{mp} and V_{mp} with improved precision, which can then be utilized to analyze the maximum power from the monitoring data.

The electrical output of PV modules is affected by many factors such as *G*, *T*, and shading. Detection of the PV module degradation is important, because degradation reduces the PV module efficiency. The time–series data taken at various irradiances and temperatures should be systematically analyzed. The new formulas can accurately translate I_{mp} and V_{mp} for temperature and irradiance. The significance of using only I_{mp} and V_{mp} is to simplify the analyzed data. This technique is useful to be applied for partial shading detection. The experimental I_{mp} and V_{mp} are corrected for temperature by the formulas, which have enabled precise and straightforward analysis of the I_{mp}–V_{mp} curve with the shading effect (details in Chapter 5). The method for detecting the existence of shading is investigated by using the experiments and simulation results. This study clarifies the basic approach toward characterizing PV module performance by using I_{mp} and V_{mp}.

Some defects, such as cell cracks and increase in series resistance (R_s), which are caused by mechanical stresses, and solder bond failure, affect the reliability of PV modules and systems. An additional degradation is the potential–induced degradation (PID) caused by voltage stress. Today typical system voltage ranges of 700 – 1000 V [32]. These deteriorations reduce energy production and impose severe risks on the PV modules and systems over time [33, 34]. Previous studies have proposed several techniques, such as EL [33-35] and *I–V* curve measurements [36], to investigate cell cracks. An investigation the PID using *I–V* curves and EL measurement techniques, have been proposed [32, 37]. Although the *I–V* curves and *P–V* curves are useful for assessing failures of the PV modules and systems, they present significant disadvantages as well; the measurements need to interrupt the MPPT operation, and require additional test equipment (i.e., an *I–V* tester or EL camera). In order to solve the problem,

the present study measures I_{mp} and V_{mp} which are practically the only electrical parameters that can be measured without interrupting the MPPT operation. The present study also utilizes (for the first time) the new formulas for the temperature–corrected I_{mp}–V_{mp} curves instead of the I–V curve in order to analyze degradations. In Chapter 6, the effects of degradation, such as cell crack, increase in R_s, and PID, are investigated via numerical simulations to investigate the basic method for detecting degradations by using the I_{mp}–V_{mp} curve. The algorithm for this detection method is shown in Fig. 1.6. In the first step, the time–series data of I_{mp} over a few days are collected from the module; these include low-to-high I_{mp} or irradiance, V_{mp}, and module temperature (T_m). In the second step, the V_{mp} is corrected for temperature by using the new formulas. In the third step, the I_{mp}–V_{mp} curve is constructed. Then, analysis is performed to detection deteriorations such as shading effects, cell cracks, increases in R_s, and PID.

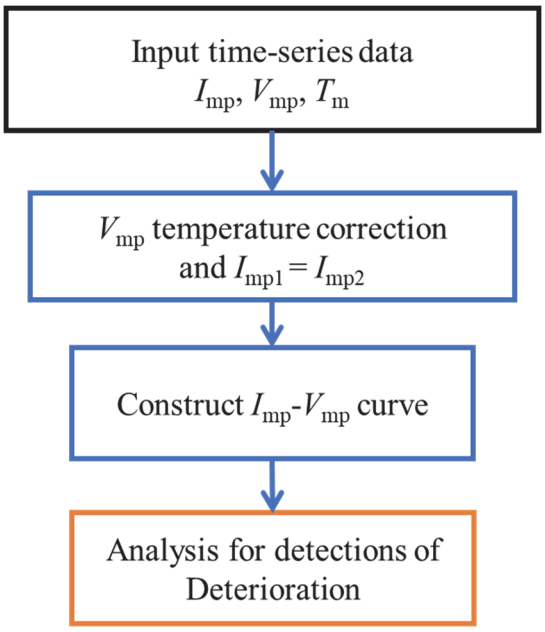

Figure 1.6. The flow chart of the method for detection deterioration.

1.6 Thesis Structure

This thesis is organized as follows: Chapter 1 presents the energy background, renewable energy outlook, global PV installation, scope of the problem, and research framework. In Chapter 2, the general

background of PV devices characteristics is introduced. Chapter 3 presents the objectives, methodology, and originality of the research. In Chapter 4, the new translation equations of I_{mp} and V_{mp} for crystalline–silicon PV devices are explained. Chapter 5 presents the novel method for detecting shading effect using I_{mp}, V_{mp}, T_m, and G. In Charpter 6, a failures–detections using only I_{mp}, V_{mp}, and T_m is presented. Finally, the research conclusions are presented in Chapter 7. The research structure is also shown in Fig. 1.7.

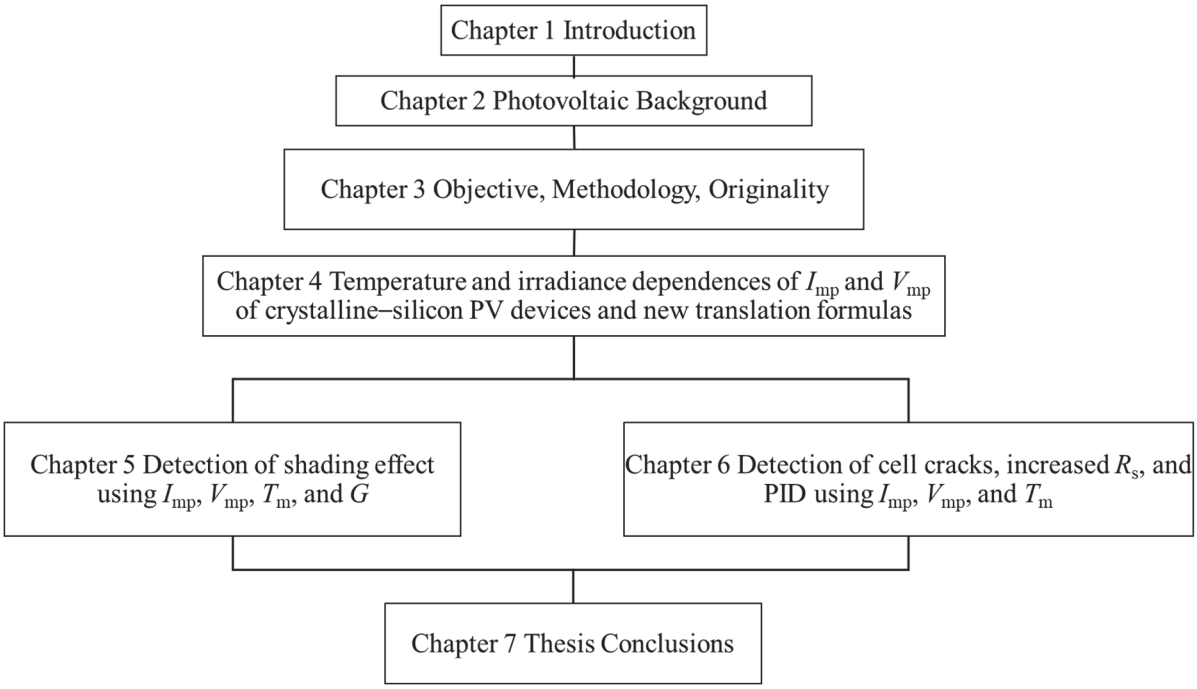

Figure 1.7. Research structure.

Chapter 2

Photovoltaic Background

2.1 Photovoltaic Module

2.1.1 Photovoltaic modules types

PV modules or cells can be manufactured from different materials. However, they perform to harvest solar energy and convert it to electricity. The most common material for PV module structure is silicon. Other higher efficiency technologies such as gallium arsenide and multijunction cells. There are also emerging PV cell technologies such as perovskite cells, organic cells, dye–sensitized cells, and quantum dots. Crystalline–silicon PV cells and modules have dominated PV technology from the beginning. They constitute more than 85 % of the current PV market. One reason for crystalline silicon to be dominant in PV cells is that microelectronics has developed silicon technologies greatly. In a PV module, the cells are usually connected in series. Thinned ribbons are soldered to the cell busbar to forms connection between the PV cells. The common PV module configuration uses series–connected cells to produce an appropriate voltage. Figure 2.1 shows a PV module which is the configuration of the cells comprising of 36 series–connected. For conventional silicon, the open–circuit voltage (V_{oc}) is about 0.6 V/cell; thus, the V_{oc} of the module is approximately of 21.6 V.

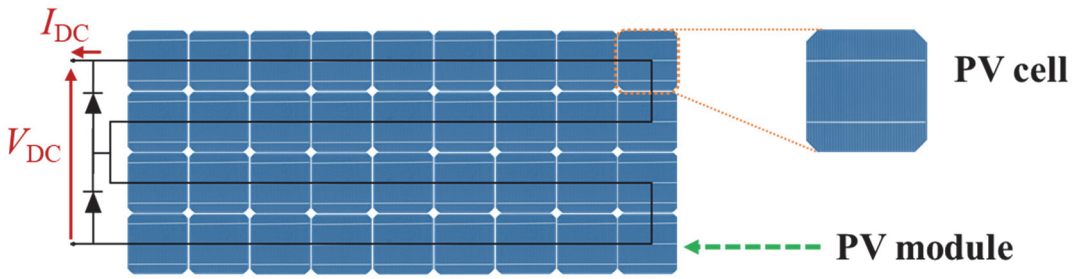

Figure 2.1. PV module with 36 series–connected cells, including two bypass diodes.

2.1.2 Photovoltaic module in the system and other components

The main components in a PV system are consist of the PV module(s), DC–to–AC power inverter/controller (included the MPPT), monitoring system, battery bank, utility meter, and so on. Figure 2.2 shows an example of the PV string system. PV systems typically contain on–grid and off–grid application; however, they have distinctly different needs. Although off–grid PV systems are typically expensive and of low efficiency, they often great solutions compared with the traditional option of fueled generators for extending grid services into a remote area. On–grid systems, for which the energy is either used on–site or injected into the utility grid, are almost always less expensive in term of installation, maintenance, operation, and they are more efficient than off–grid systems.

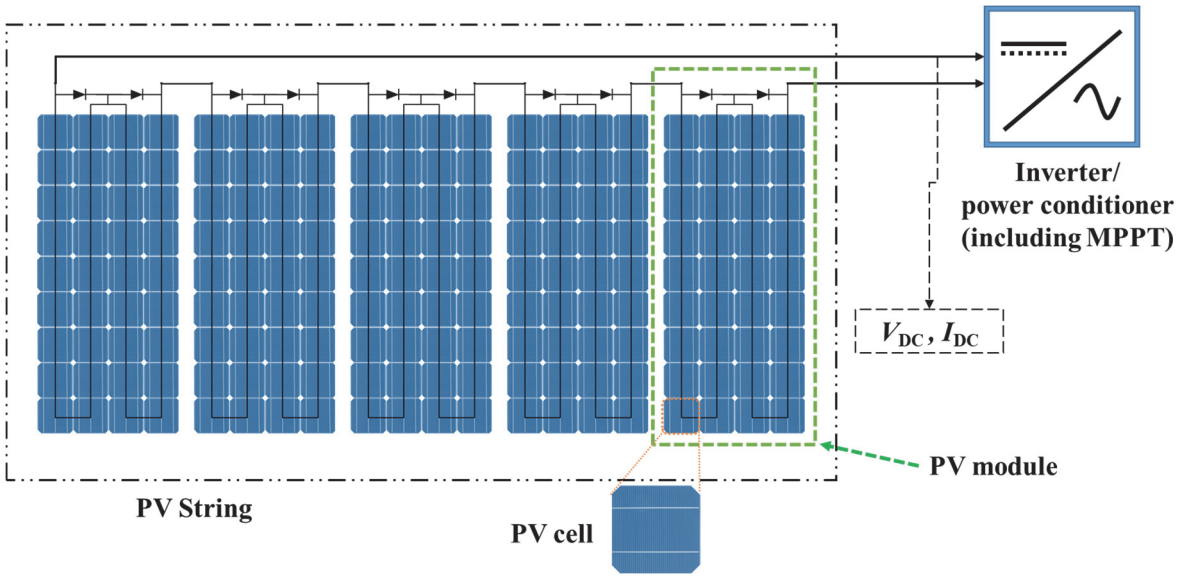

Figure 2.2. PV string configuration and component definitions.

2.1.3 Photovoltaic monitoring

PV data monitoring systems normally consist of a recorder, controller, and software functions. They need input data such as PV electrical output parameters, inverter status, energy consumption, and power quality, as well as weather conditions such as ambient temperature, irradiance, and wind speed.

System monitoring is important in PV systems because it can be used to optimize the system performance. There are quickly possible to access energy production, problems detection, and other appropriate actions in PV system operation. The PV's output production can be analyzed by using recording data and used to calculate the energy/economic profits and reduce the consumption problem.

2.1.4 Operations and maintenance

Operation and maintenance (O&M) present a major and effective approach toward reducing the costs, improving the availability, and increasing the productivity of PV systems. The minimal O&M for a PV systems involves inspected, such as PV modules, inverters, verification correct system operation, failure checks, cleaning, alarm checks, spare-parts listing, and where applicable components replacement.

PV modules inspection can be done by the operators. The inspection of PV modules includes physical damage such a delamination, cracks, microcracks or snail trails, burned connections or hot spots, corrosion, mounting weaknesses, soiling, and droppings or shading effects from nearby trees or leaves, amongst other characteristics.

2.2 Photovoltaic Characteristics

2.2.1 Photovoltaic output parameters

The one-diode model equivalent circuit of a silicon PV cell is shown in Fig. 2.3; it corresponds to the output current of the crystalline–silicon PV cell, which expressed as

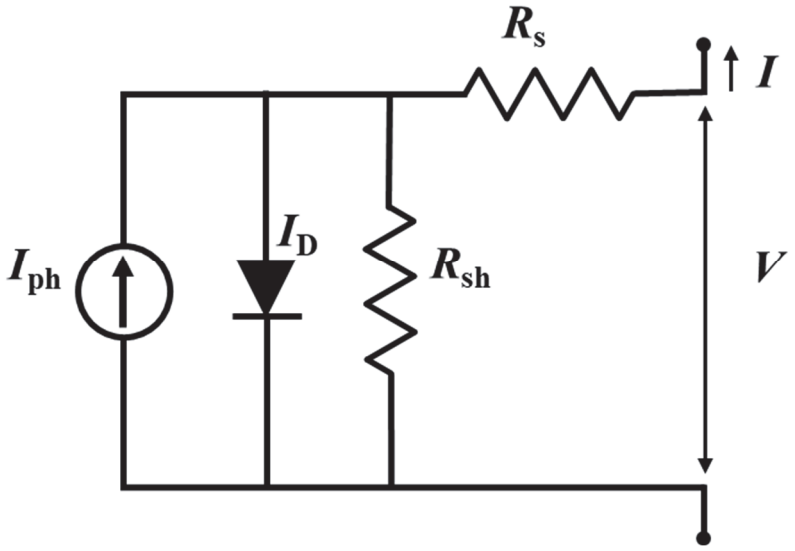

Figure 2.3. A PV cell circuit, including the series and shunt resistances.

$$I = I_{\text{ph}} - I_0 \left[\exp\left(\frac{q(V+IR_S)}{N_c nkT}\right) - 1\right] - \frac{V+IR_S}{R_{\text{sh}}}, \tag{2.1}$$

where I_{ph} is the photo–generated current. The second term is the diode current which consist of I_0 is the diode reverse–saturation current, q is the electron charge, V is the output voltage, R_s is the series resistance, N_c is the number of series–connected cells in the module, n is the diode ideality factor, k is the Boltzmann's constant, T is the device temperature in Kelvin, and the R_{sh} is the shunt resistance. The series resistance (R_s) has affected to reduce the short–circuit current (I_{sc}). Sources of R_s include metal contacts, particularly front grids, and transverse flow of current in the PV cell emitter to the front grid. The shunt resistance (R_{sh}) has no effect on the I_{sc}, but reduces the open–circuit voltage (V_{oc}).

The current–voltage (I–V) curve in which the PV cell produces current is shown in Fig. 2.4. The voltages and currents can be measured to calculate the V_{oc}, I_{sc}, and P_{max} ($I_{mp}\times V_{mp}$). The I_{sc} is linearly dependent upon the irradiance. Multiplying the current by the voltage yields the cell power. The P_{max} is especially important when considering maximizing power transferred to the load. In Fig. 2.4, there is one point on the I–V curve which the PV cell produces P_{max}. This point can also be determined by differentiating the power equation and setting the result equal to zero. Then, the voltage at maximum

power (V_{mp}) and the current at maximum power (I_{mp}) are found. The PV cell's maximum power can be expressed as

$$P_{max} = I_{mp}V_{mp} = FFI_{sc}V_{oc}, \tag{2.2}$$

where FF is the PV cell fill–factor, which is an index of the quality of the cell. It is a measure of the difference from the square shape of the I–V curve. FF determines the power output of the cell, and P_{max} is related to the diode–law equation. In addition, the effects from series resistance (R_s) and shunt resistance (R_{sh}) are added to the FF losses.

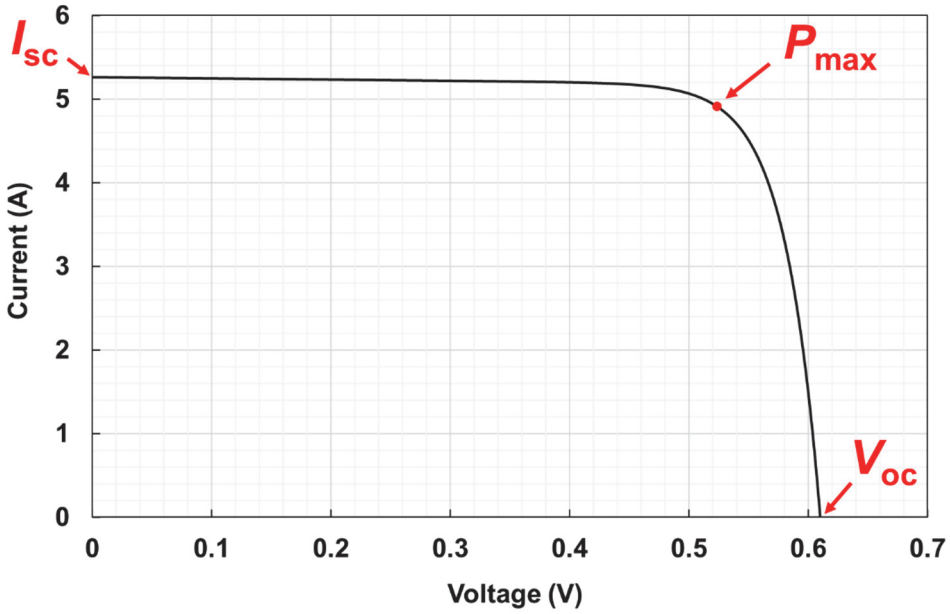

Figure 2.4. I–V curve of a PV cell.

2.2.2 Effect of parasitic resistances

PV cells generally have a parasitic resistance associated with them, as shown in Fig. 2.3. Both R_s and R_{sh} function to reduce *FF*. The major contributors to R_s are the bulk resistances of the semiconductor material, the metallic contact, and the interconnections. The effect of R_s is shown in Fig. 2.5.

The shunt resistance R_{sh} is produced by p–n–junction non–idealities and impurities near the junction; they cause the partial shorting of the junction, particularly near the cell edges. The effect of R_{sh} is shown in Fig. 2.6.

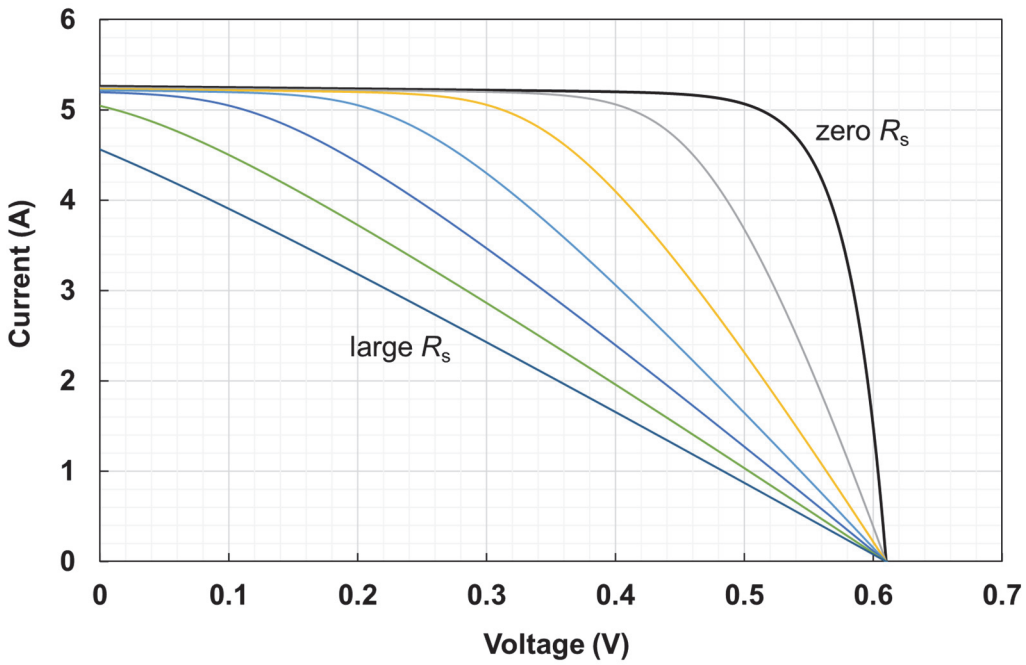

Figure 2.5. Effect of R_s on PV cell *I–V* curves.

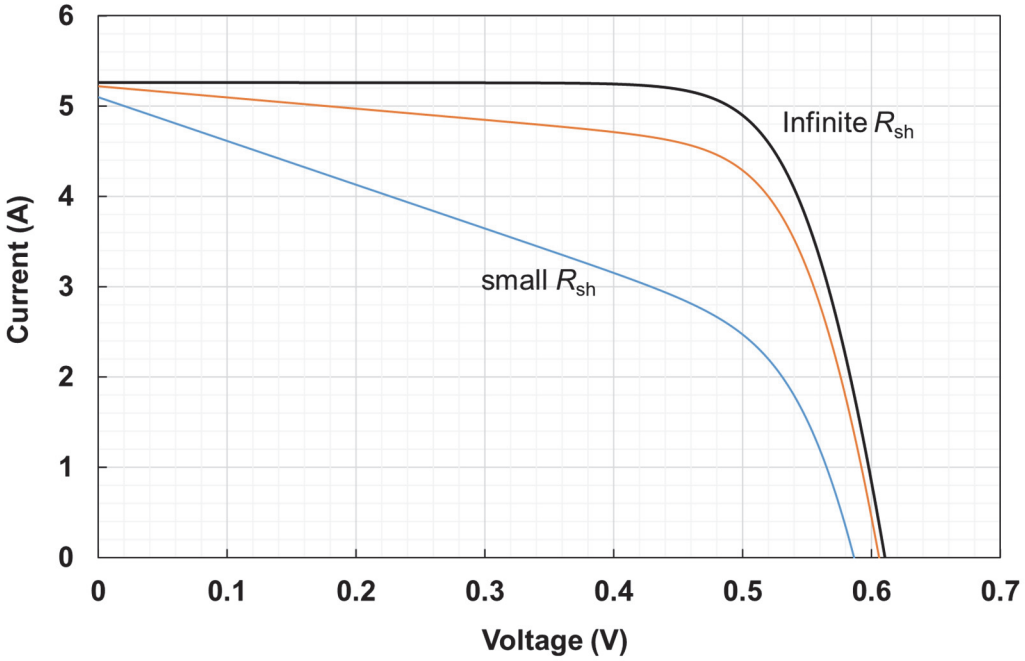

Figure 2.6. Effect of R_{sh} on PV cell *I–V* curves.

2.2.3 Conversion efficiency of photovoltaics

Efficiency is the most commonly used parameter for comparing the performances of PV cell to others. The conversion efficiency is defined as the ratio between the PV's output and the input from the sun. It depends on the spectrum and intensity of the sunlight and PV cell temperature. Terrestrial PV cells/modules are basically measured under STC conditions of irradiance 1 kW/m^2, air mass (AM) 1.5, and PV cell temperature at 25 °C. The conversion efficiency (η) of a PV cell is determined as the fraction of incident power which is converted into electricity, as illustrated in

$$\eta = \frac{P_{\text{out}}}{P_{\text{in}}} = \frac{V_{\text{mp}} I_{\text{mp}}}{P_{\text{in}}}, \tag{2.3}$$

where the P_{in} is the input power. The STC (1 kW/m^2, 25 °C) are usually used in the specifications of commercial products.

2.2.4 Effect of temperature

The PV cell *I–V* curve is also temperature sensitive. V_{oc} is directly proportional to the absolute temperature of the PV cell. The V_{oc} of a silicon PV cell decreases under a 2.3 mV/°C increase in temperature. The cell power also decreases by approximately 0.5 %/°C under such conditions [38]. Figure 2.7 shows the temperature dependence of the PV cell *I–V* curve.

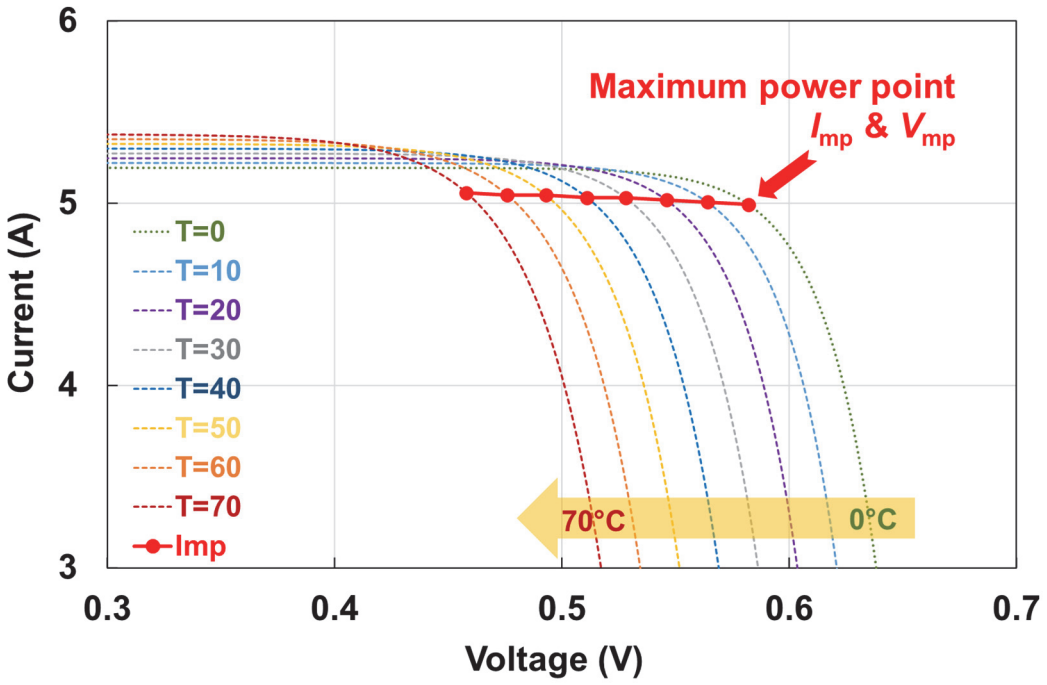

Figure 2.7. Temperature dependence of PV cell *I–V* curve.

2.2.5 Effect of irradiance

When the PV cell is illuminated, electron–hole pairs are generated by the interaction of the incident photons with atoms of the cell. The electron field created by the cell junctions causes the photon–generated–electron–hole pairs to separate, with the electrons drifting into the n–region of the PV cell and the holes drifting into the p–region. The output current and voltage of the cell depend upon the

illumination level. PV cells feature both a limiting voltage and current; hence, the PV cells are not damaged by operations under either open–circuit or short–circuit conditions. The PV cell short–circuit current (I_{sc}) is directly proportional to the cell surface irradiance. Figure 2.8 shows the *I–V* curves of the typical PV cell at irradiances between 0.2 kW/m^2 and 1 kW/m^2 in the black lines. The maximum power points are also shown along the red line. The I_{mp}–V_{mp} curve will be discussed in detail in Chapter 3.

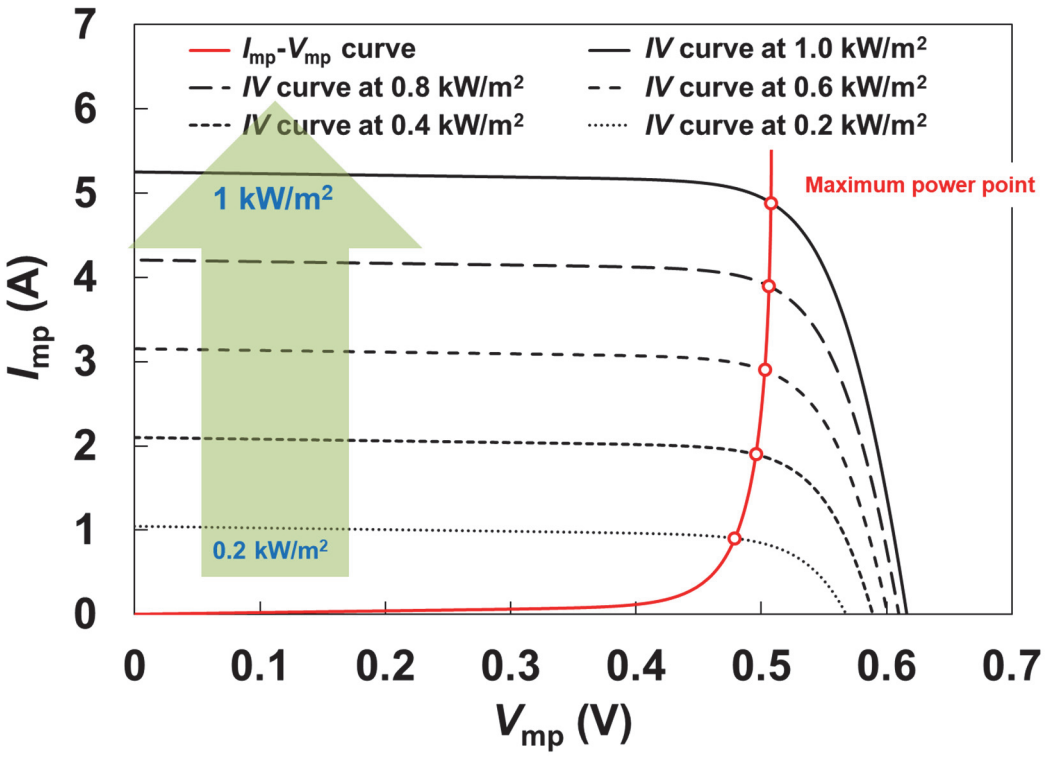

Figure 2.8. Irradiance dependence of PV cell *I–V* curves, the I_{mp}–V_{mp} curve is also shown in red.

2.3 Cell Interconnection

Several PV cells can be interconnected in order to achieve greater power. Two types are possible; series and parallel cell interconnections. PV cells are generally connected in series to create a higher voltage. The cell voltages increase while the current remains constant. Multiple cell strings are often connected in parallel, particularly in modules with higher–output. Here, the voltage remains constant and the current increases. Several PV cells are first connected in series to form a string; these strings

are then connected in parallel in a module. Figure 2.9 shows four PV cells connected in series, which increase the voltage by a factor of four. Figure 2.10 presents *I–V* curves that shown how the output voltage is increased when measured between one cell, two cells, three cells, and four cells, respectively.

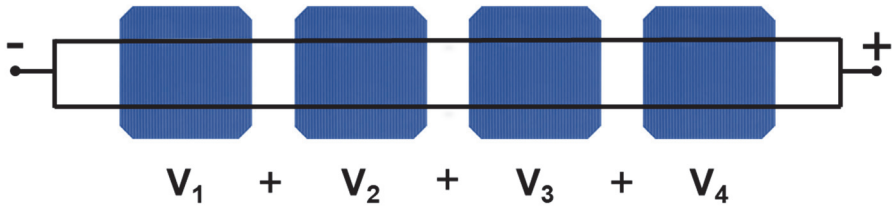

Figure 2.9. Four series–connected PV cells.

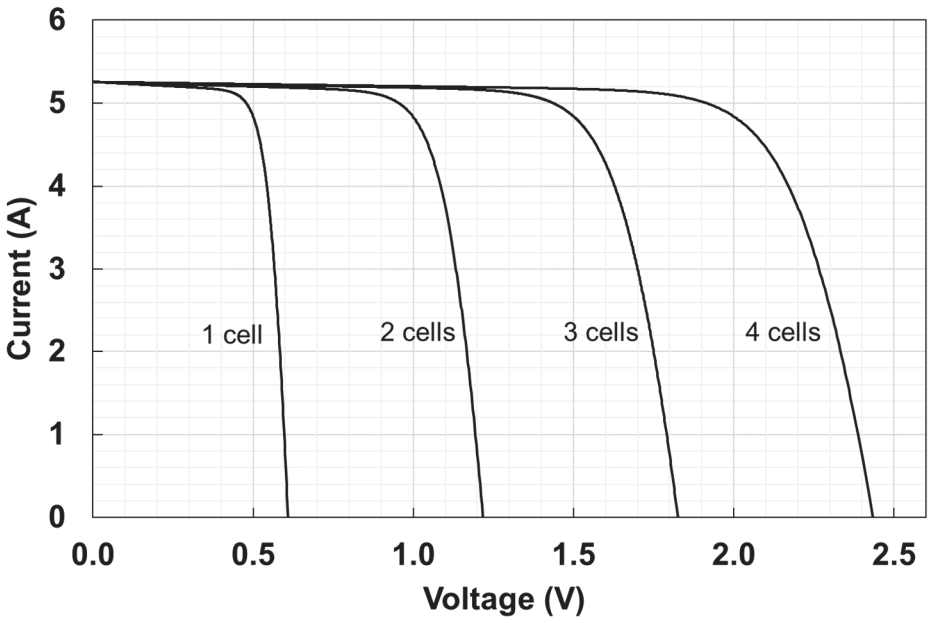

Figure 2.10. Output voltage increase as the sum of the individual cell output voltages in Fig. 2.8.

Chapter 3

Objective, Methodology, and Originality

The output power of a solar PV cell is a function of the irradiance falling upon the cell and the cell's operating temperature, and there exists a complex relationship among these parameters. The electrical characteristics of PV modules are usually provided by manufacturers and in general the characteristics are provided under STC. The *I–V* characteristics of solar cells are basically characterized by three parameters; short–circuit current (I_{sc}), open–circuit voltage (V_{oc}), and maximum power (P_{max}) that usually have temperature and irradiance dependence. Temperature plays a major factor in determining the solar cell efficiency. As the temperature increases, the output voltage of the solar cells is reduced. Even though the rate of photon–generation increases thus reverse current increases and reduces the bandgap. The current increases with temperature because the bandgap energy (E_g) decreases and more photons have enough energy to create electron–hole pairs. However, this is a small effect compared to the voltage temperature dependence. Normally, PV module operates under outdoor conditions, which are not included in the commercial module specifications provided by the manufacturer. Moreover, the factors of irradiance and temperature change according to location, time, and season.

3.1 Objective

The PV module is the principal component of the PV system. The PV systems must be reliable and cost–effective during their operating life period. The O&M of PV systems requires monitoring and data–analysis technique, to maintain, diagnose, and ensure the safety of the system. The PV module is a major piece of equipment and represents the main cost factor of the PV system. Normally, PV system performance is measured under operation temperatures and irradiances. The PV system output current at maximum power I_{mp} and voltage at maximum power V_{mp} are recorded during the PV system's MPPT operation. I_{mp} and V_{mp} are affected by temperature and irradiance. It can be helpful if these data are corrected to the target temperature and irradiance, such as to the STC. Thus, correction data for the PV output at least by temperature are important for PV performance analysis. Although, previous studies have discussed I_{mp} and V_{mp} based on experimental results of *I–V* curve and have also described *I–V* curve translation procedures, which require a set of *I–V* curves under different irradiances and temperatures. They also require experimental *I–V* curves and TCs of the *I–V* parameters, such as the

TCs of I_{sc} and V_{oc}. This is unsuitable for continuous monitoring, because the measurement interrupts the MPPT operation. Recently, a methodology called the Suns–Vmp method was proposed [28, 29], which enabled monitoring and diagnosis of PV system degradation, using only the MPP values. This method requires datasheet information for the initial values, and it requires to extract diode parameters by using numerical fitting in a specific program, in order to evaluate their performance. This study analytically and experimentally investigated expressions for the temperature and irradiance dependences of I_{mp} and V_{mp} of commercial crystalline–silicon PV devices, which do not require parameter fitting. The current approach is expected to be applicable to PV device performance characterization situations.

The first objective is to develop new formulas for the temperature correction of experimental V_{mp} data. The novelty of the present study is that these formulas do not require advanced information of TC, diode parameters, or *I–V* curve parameters. The results lead to translation of I_{mp} and V_{mp} with improved precision, which can be utilized for analysis of the maximum power from the monitoring data. Then, the I_{mp} and V_{mp} after correction can be analytically investigated. Advantageously, the experimental data analyzed in this study, including the formulas of I_{mp} and V_{mp} corrections, are obtained without interrupting system operation. This study is an advantage over an onsite *I–V* measurement included the TC described in previous studies. The simplified formulas can be applied for translate I_{mp} and V_{mp}. Moreover, the characterization of PV performance can be analytically investigated after I_{mp} and V_{mp} correction. Details are given in Chapter 4.

The second objective, the I_{mp}–V_{mp} curve technique is useful to be applied for partial–shading detection. The experimental V_{mp} and I_{mp} are corrected for temperature by the formulas, which have enabled precise and straightforward analysis of the I_{mp}–V_{mp} curve under the shading effect. The method for detecting the existence of shading is investigated by using experimental and simulation results. This study clarifies the basic approach for characterizing the module performance by using V_{mp} and I_{mp}. Details are explained in Chapter 5.

The third objective is to utilize the new formulas to accurately translate V_{mp} and I_{mp} for temperature and irradiance. The effects of degradation, such as cell cracks, an increase in series resistance (R_s), and PID, are investigated via numerical simulations, to investigate the basic method for detecting degradation by using the I_{mp}–V_{mp} curve. Details are explained in Chapter 6.

3.2 Methodology

The methodology employed for precise PV module performance characterization in this study focused on the new translation formulas for the temperature correction of experimental V_{mp} and I_{mp}, expressed as

$$V_{\mathrm{mp2}} = \left[V_{\mathrm{mp1}} + \frac{T_2 - T_1}{T_1}(V_{\mathrm{mp1}} - \frac{nE_g}{q} \cdot N_{\mathrm{c}})\right] \times [1 + \alpha(T_2 - T_1)] \,, \tag{3.1}$$

$$I_{\mathrm{mp2}} = I_{\mathrm{mp1}} \,, \tag{3.2}$$

where, T_1 and V_{mp1} are the measured temperature and measured V_{mp}, respectively. T_2 is the target temperature. V_{mp2} is the V_{mp} at T_2. N_c is the number of series–connected cells.

The above equations present the new temperature corrections for V_{mp} and I_{mp}. Details of their development are shown in Chapter 4. However, the temperature–independence of I_{mp} needs to review and to confirm by using simulations and experiments in the following sections.

3.2.1 Temperature and irradiance dependences of I_{mp}

Using one–diode model, and neglecting the R_{sh}, the output current I of a PV module can be approximately expressed as follows:

$$I = I_{sc} - I_0 \exp\left(\frac{q(V+IR_s)}{N_c nkT}\right). \tag{3.3}$$

Here, I_{sc} is the short–circuit current, I_0 is the diode reverse saturation current, q is the electron charge, V is the output voltage, R_s is the series resistance, N_c is the number of series–connected cells in the module, n is the diode ideality factor, k is the Boltzmann's constant, and T is the device temperature in Kelvin. At the MPP, the I–V and P–V curves and MPP, are shown in Fig. 3.1, and the equations are obtained as follows:

$$I_{sc} - I_{mp} = I_0 \exp\left(\frac{q(V_{mp}+I_{mp}R_s)}{N_c nkT}\right), \tag{3.4}$$

$$V_{mp} = \frac{N_c nkT}{q} \ln\left(\frac{I_{sc}-I_{mp}}{I_0}\right) - I_{mp}R_s \, . \tag{3.5}$$

Considering that the derivative of power at MPP, $d(\mathrm{P}) = d(IV)$, is $\left.\frac{d(IV)}{dV}\right|_{mp} = 0$; thus, the V_{mp} equation can be expressed by Eq. (3.6).

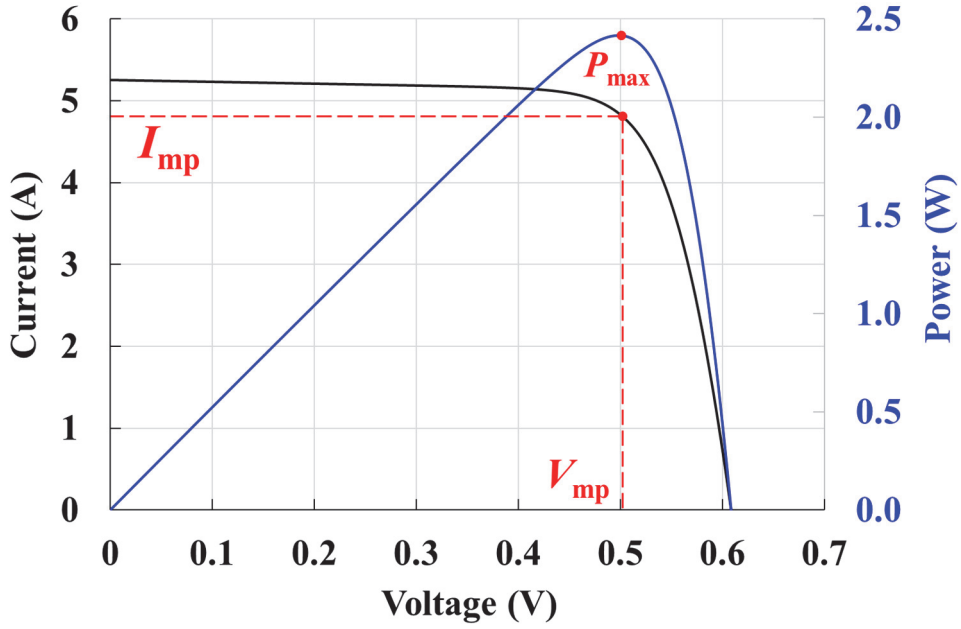

Figure 3.1. *I–V* and *P–V* curves, with MPPs indicated.

$$V_{mp} = \frac{N_c nkT}{q} \frac{1}{\frac{I_{sc}}{I_{mp}} - 1} + I_{mp}R_s \, . \tag{3.6}$$

From Eqs. (3.5) and (3.6), the relation among I_{mp} and the other parameters is obtained which does not include V_{mp} as

$$I_{mp} = \frac{\ln\left(\frac{I_{sc}-I_{mp}}{I_0}\right)}{\frac{1}{I_{sc}-I_{mp}}+\frac{2R_S}{N_c nkT/q}} \cdot \tag{3.7}$$

Figure 3.2 shows the temperature dependence of I_{mp} at 1 kW/m^2, which is normalized by its STC value for various values of R_s, n, and I_0; this can be calculated by explicitly considering the TC of I_{sc} (α) – using

$$I_{mp} = \frac{\ln\left(\frac{I_{sc}+\alpha I_{sc}(T-T_0)-I_{mp}}{I_0}\right)}{\frac{1}{I_{sc}+\alpha I_{sc}(T-T_0)-I_{mp}}+\frac{2R_S}{N_c nkT/q}} \cdot \tag{3.8}$$

Here, T_0 = 25 °C (298.15 K) and α is assumed to be 0.05 %/K.

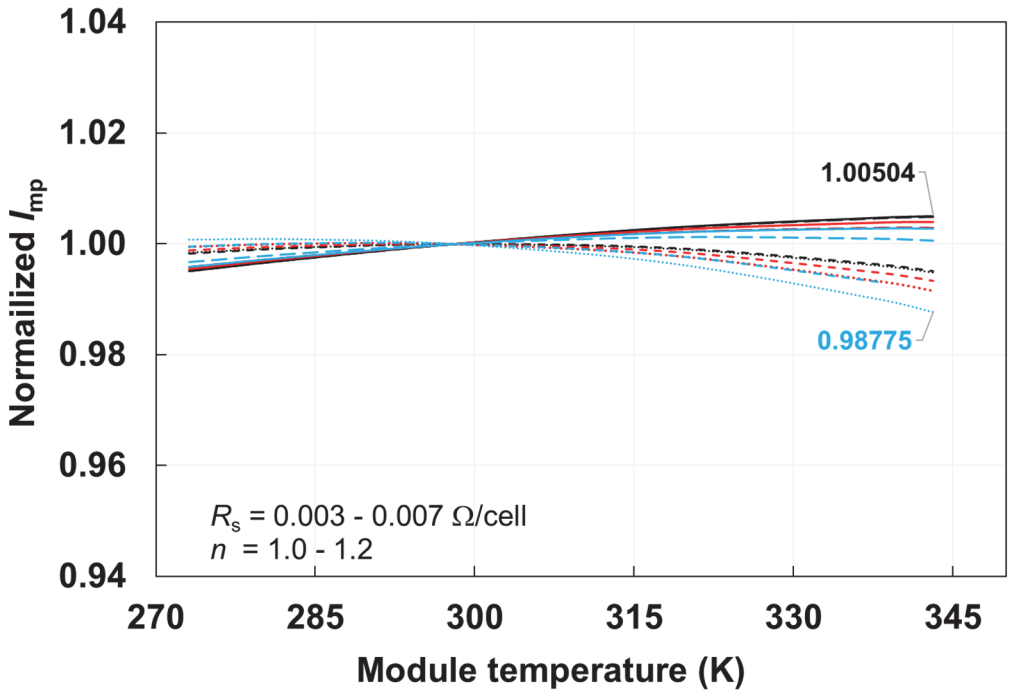

Figure 3.2. Normalized I_{mp} vs. module temperature at 1 kW/m^2, for R_s at 3 – 7 mΩ/cell, I_{01} between 1.965×10^{-10} and 1.075×10^{-8}, I_{02} between 2.021×10^{-10} and 1.207×10^{-8} at n between 1.0 and 1.2 respectively, and α = 0.05 %/K, calculated from Eq. (3.8) by using Microsoft Excel Solver. The results show that at maximum value = 1.00504 and minimum = 0.98775 then normalized ΔI_{mp} within ±1 %.

The results in Fig. 3.2 show that the temperature dependence of I_{mp} is less than ±1 % for temperature variations over 0 – 70 °C (273.15 – 343.15 K) for the ranges of R_s and n, which includes typical commercial crystalline–silicon PV modules. The simulation based on Eq. (3.8) also shows that the I_{mp} is nearly proportional to irradiance, and its non–linearity is within ±0.4 % in the irradiance range between 0.5 and 1.2 kW/m^2, as shown in the Fig. 3.3.

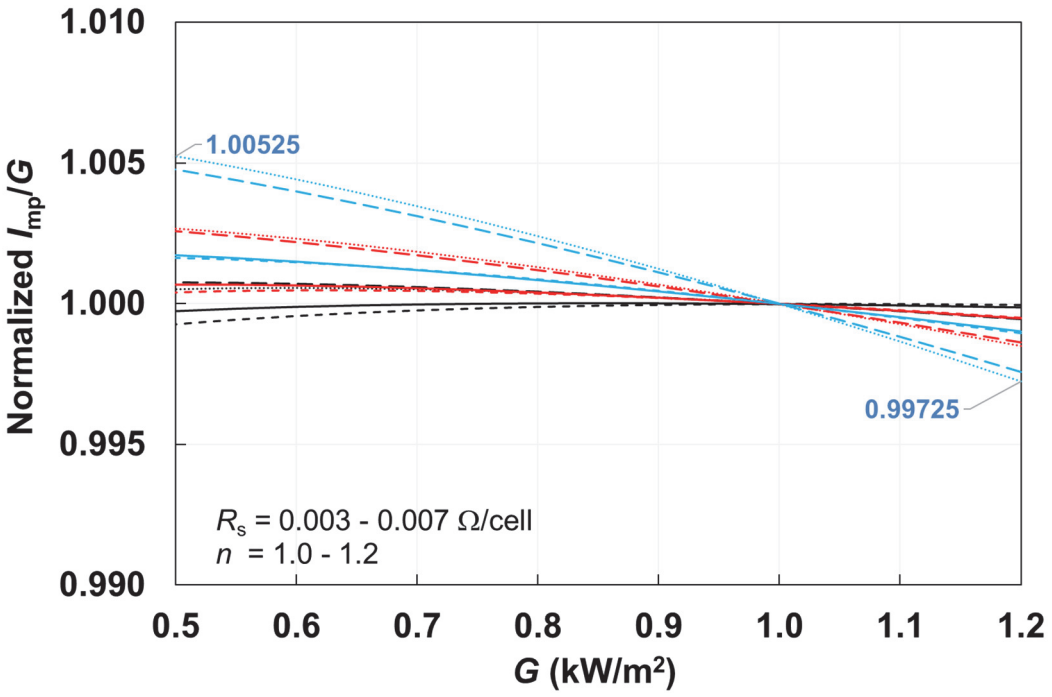

Figure 3.3. Normalized I_{mp}/G vs. G, for R_s at 3 – 7 mΩ/cell, I_{01} between 1.965×10^{-10} and 1.075×10^{-8}, I_{02} between 2.021×10^{-10} and 1.207×10^{-8} at n between 1.0 and 1.2 respectively, and α = 0.05 %/K. The results show that at maximum value = 1.00525 and minimum = 0.99725 then normalized $\Delta I_{mp}/G$ within ±0.4 %.

3.2.2 Temperature and irradiance dependences of I_{mp}/I_{sc}

From Eq. (3.4), the I_{mp} is obtained as follows,

$$I_{\mathrm{mp}} = I_{\mathrm{sc}} - A \cdot \exp\left(\frac{q(V_{\mathrm{mp}}+I_{\mathrm{mp}}R_{\mathrm{s}})}{N_{\mathrm{c}}nkT} - \frac{E_{\mathrm{g}}}{kT}\right). \tag{3.9}$$

The temperature and irradiance dependences of V_{mp} and I_{mp}/I_{sc} were simulated by Eq. (3.9) and the parameter settings of typical commercial crystalline–silicon PV module in the ranges of R_s at 3 – 7 mΩ/cell and n between 1.0 and 1.2. The results shows that V_{mp} decreases linearly under an increase in temperature. The temperature dependence of V_{mp} is mainly dependent on n. The results of V_{mp} decrease linearly with temperature within ±0.4 % for n = 1.0 and ±0.5 % for n = 1.2, in the temperature range between 0 °C and 70 °C. V_{mp} is nearly constant within ±1.6 % for irradiance range over 0.5 – 1.2 kW/m^2. Here, an empirical relation $I_{mp} \cong 0.95 \times I_{sc}$ was assumed. The I_{mp}/I_{sc} was experimentally measured in [12] and shown to be nearly constant for both temperature and irradiance changes for silicon solar cells. In this study, the I_{mp}/I_{sc} was simulated with respect to I_{sc} and irradiance (G). Figure 3.4 shows the relation between I_{mp}/I_{sc} and temperature. Figure 3.5 shows the relation between I_{mp}/I_{sc} and irradiance. Both the temperature and irradiance dependences of I_{mp}/I_{sc} are affected by n.

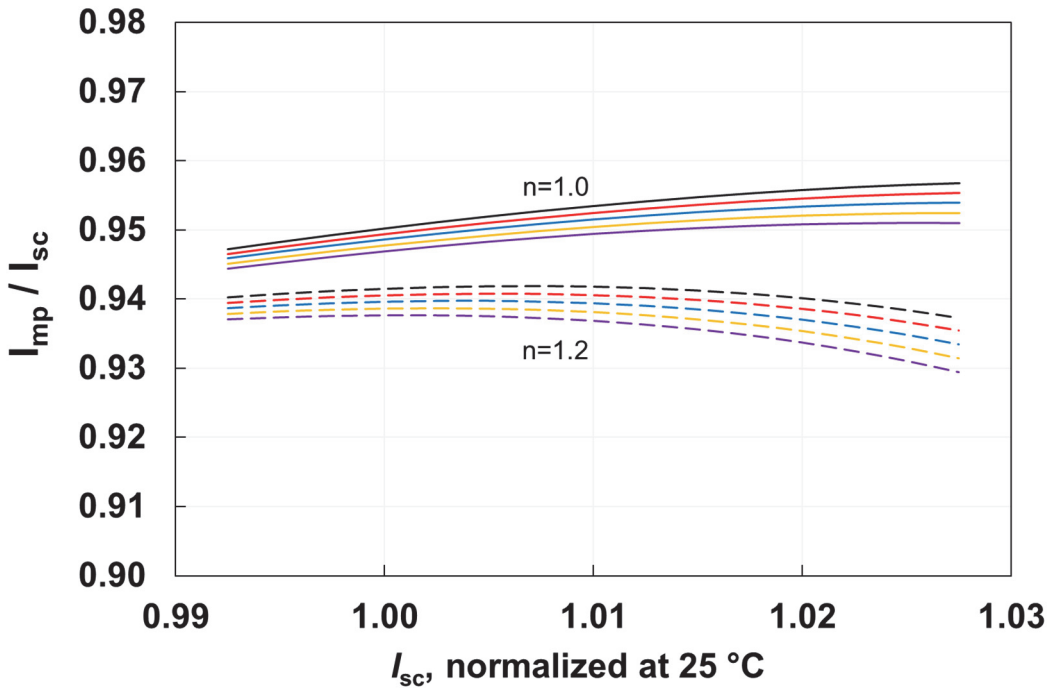

Figure 3.4. I_{mp}/I_{sc} vs. I_{sc} for R_s between 3 and 7 mΩ/cell, n between 1.0 and 1.2, and α = 0.05 %/K.

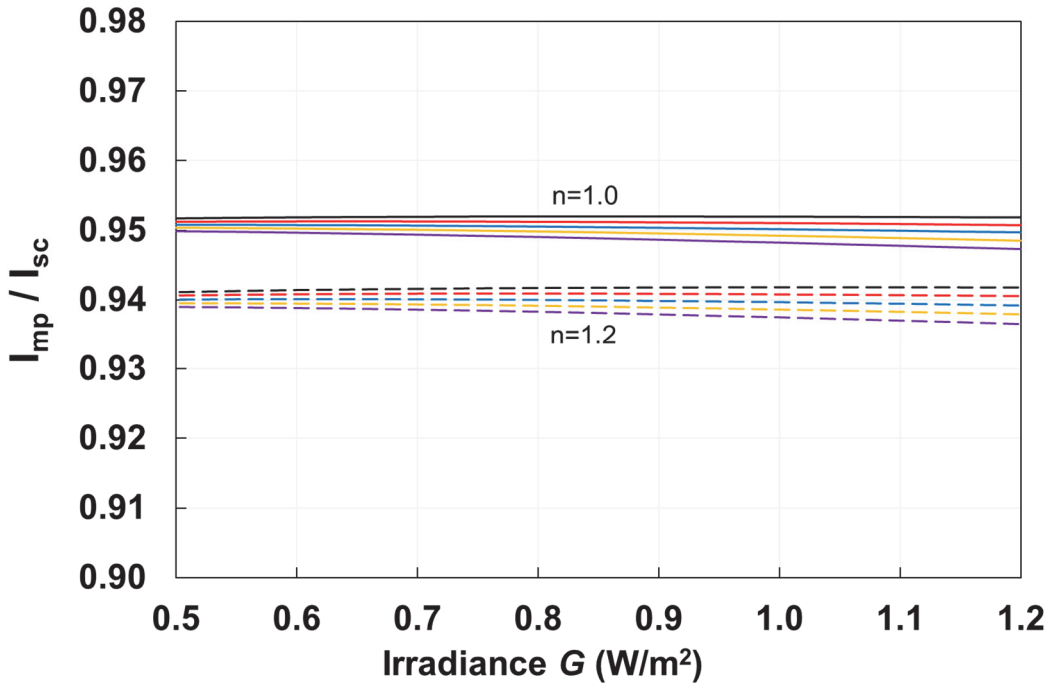

Figure 3.5. I_{mp}/I_{sc} vs. I_{sc}, for R_s between 3 and 7 mΩ/cell, n between 1.0 and 1.2, and α = 0.05 %/K.

3.2.3 The relation between P_{max} and G

The maximum power of a crystalline–silicon cell was simulated by Eq. (3.8) in the range of R_s between 3 and 7 mΩ/cell and n between 1.0 and 1.2. The results show that P_{max} is nearly proportional to irradiance within ±1.6 % in the irradiance range between 0.5 and 1.2 kW/m^2, as shown in Fig. 3.6.

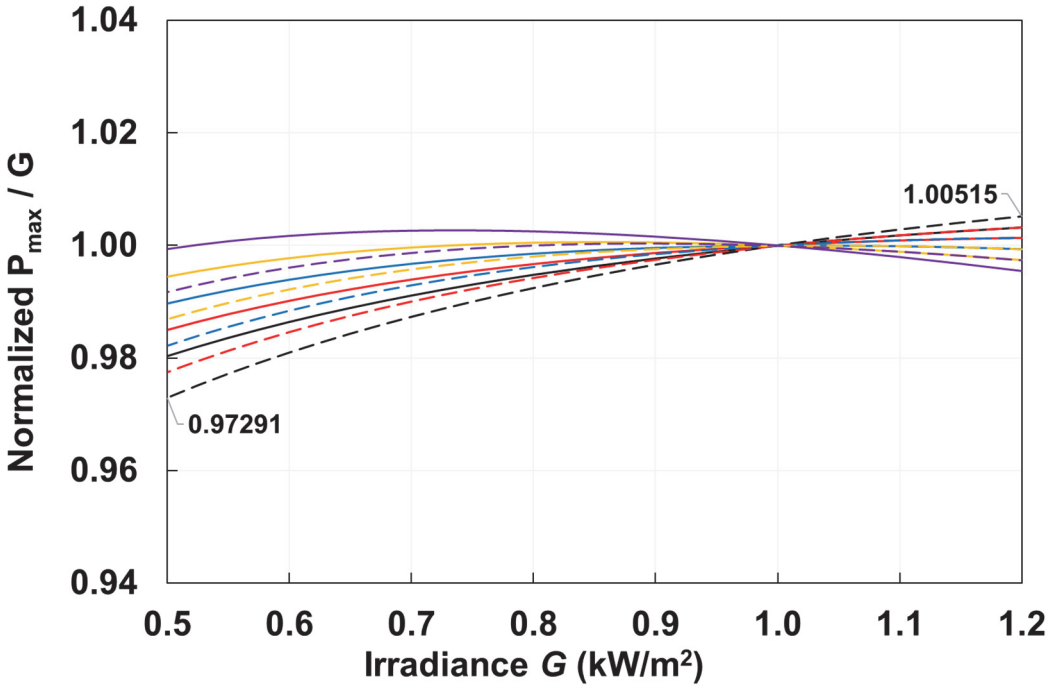

Figure 3.6. Normalized P_{max}/G vs. G, for R_s between 3 and 7 mΩ/cell, n between 1.0 and 1.2, and α = 0.05 %/K. The results show maximum value = 1.00515 and minimum value = 0.97291; then, normalized $\Delta P_{max}/G$ within ±1.6 %.

3.2.4 Temperature translation of voltage and comparison with experiment

As mentioned in the previous section, the I_{mp} was simulated by Eq. (3.8) with respect to temperature variation, and it was shown to be nearly constant in the range 0 – 70 °C. Thus, the translation equation for voltage provided by Hishikawa et. al [26] can be approximately used for the temperature correction of voltage, as follows:

$$I = I_{sc} + I_0 \left\{ \exp\left(\frac{qV}{nkT}\right) - 1 \right\}. \tag{3.10}$$

The temperature dependence of I_0 is expressed as $A \cdot \exp(-E_g/kT)$, which is related to the product of the electron and hole concentrations; hence, Eq. (3.10) can be rewritten as

$$I \approx I_{\mathrm{sc}} - I_0 \exp\left(\frac{qV}{nkT}\right) = I_{\mathrm{sc}} - A \cdot \exp\left(\frac{qV}{nkT} - \frac{E_{\mathrm{g}}}{kT}\right) = I_{\mathrm{sc}} - A \cdot \exp\left\{\frac{q}{nkT}\left(V - \frac{nE_{\mathrm{g}}}{q}\right)\right\}, \tag{3.11}$$

where E_{g} denotes the bandgap energy of silicon. Differentiating Eq. (3.11) under the assumption of constant I_{sc}, I, A, and E_{g} yields the following:

$$\frac{\partial}{\partial T} \exp\left\{\frac{q}{nkT}\left(V - \frac{nE_{\mathrm{g}}}{q}\right)\right\} = 0\ , \tag{3.12}$$

$$\therefore \frac{\partial V}{\partial T} = \frac{1}{T}\left(V - \frac{nE_{\mathrm{g}}}{q}\right). \tag{3.13}$$

In Eq. (3.14), nE_{g} is the only adjustable parameter because V_1 and T_1 are measurable and q is a fundamental parameter. Thus,

$$V_2 = V_1 + \frac{T_2 - T_1}{T_1}\left(V_1 - \frac{nE_{\mathrm{g}}}{q} \cdot N_{\mathrm{c}}\right), \tag{3.14}$$

where T_1 and V_1 are the measured temperature and the output voltage, respectively. T_2 is the target temperature. V_2 is the output voltage at T_2. N_{c} is the number of series–connected cells. Equation (3.14) is useful equation for temperature correction of the *I–V* curve without information on *I–V* curve parameters or diode parameters [26]. It is valid for solar cells which follow the one–diode model Eq. (3.3) under constant I_{sc} and output current [26, 39]. If the TCs of I_{mp} and I_{sc} are neglected, the voltage V'_2 can be expressed as

$$V'_2 = V_{\mathrm{mp1}} + \frac{T_2 - T_1}{T_1}\left(V_{\mathrm{mp1}} - \frac{nE_{\mathrm{g}}}{q} \cdot N_{\mathrm{c}}\right). \tag{3.15}$$

Here, T_1 and V_{mp1} are measured cell/module temperature and V_{mp}, respectively. T_2 is 25 °C (298.15 K). V'_2 is the output voltage at 25 °C.

Equation (3.15) is useful for temperature correction of the experimental V_{mp}. The experimental V_{mp} and I_{mp} of a commercial mono–crystalline–silicon PV module were measured in April 2015. The data were collected on a clear sunny day and on a cloudy day. The V'_2 after correction was obtained by the following equation,

$$V'_2 = V_{mp1} + \frac{T_2 - T_1}{T_1}(V_{mp1} - 1.1 \cdot N_c). \tag{3.16}$$

Here, the value of nE_g/q = 1.1 V was chosen from the best–fit to experimental data, and N_c = 36 cells. The band gap energy is about 1.12 eV for silicon [40]. Therefore, n is almost equal to one.

Figures 3.7 and 3.8 show the example data plots on a clear sunny day and a cloudy day, respectively; a) shows the experimental irradiance G and module temperature, b) shows the experimental I_{mp} versus V_{mp} plot, c) shows the I_{mp} versus V'_2 plot corrected to 25 °C by using Eq. (3.16), and d) shows the $P_{max,corrected}/G$ versus G plot. The $P_{max,corrected}$ was calculated by $P_{max,corrected.} = V'_2 \times I_{mp}$. The data between 6:00 and 6:30 am and data after 3:30 pm on the clear sunny day were neglected, because they were affected by shading from nearby objects. Details of the data analysis including the shading effect will be discussed later. The irradiance G was calculated from I_{SC} using $G = (I_{SC}/I_{SC,STC})$ kW/m^2. Here, $I_{SC,STC}$ is the short–circuit current at STC.

Although Eq. (3.16) is an advantage because it does not require advanced information on the I–V curve parameters or diode parameters, it is only valid when the I_{sc} and output current are constant. In fact, the I_{sc} is temperature dependent. Thus, a new formula for V_{mp} temperature correction is developed and presented in the next chapter.

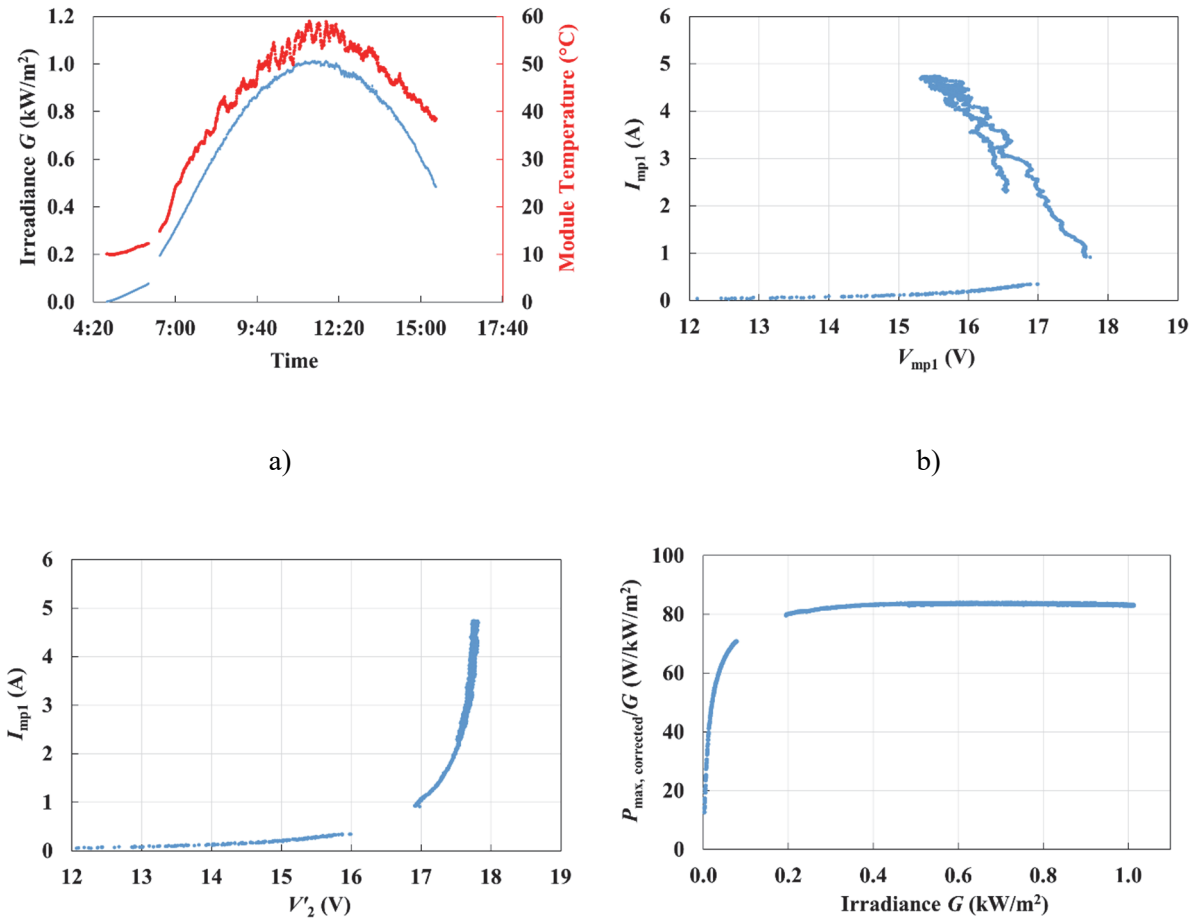

Figure 3.7. a) Experimental I_{sc} and module temperature on a clear sunny day, b) experimental I_{mp} vs. V_{mp} plot, c) I_{mp} vs. V_{mp} plot corrected to 25 °C (V'_2) by using Eq. (3.16), and d) $P_{max,corrected}/G$ vs. G plot. $P_{max,corrected}$ was calculated using $P_{max,corrected.} = V'_2 \times I_{mp}$.

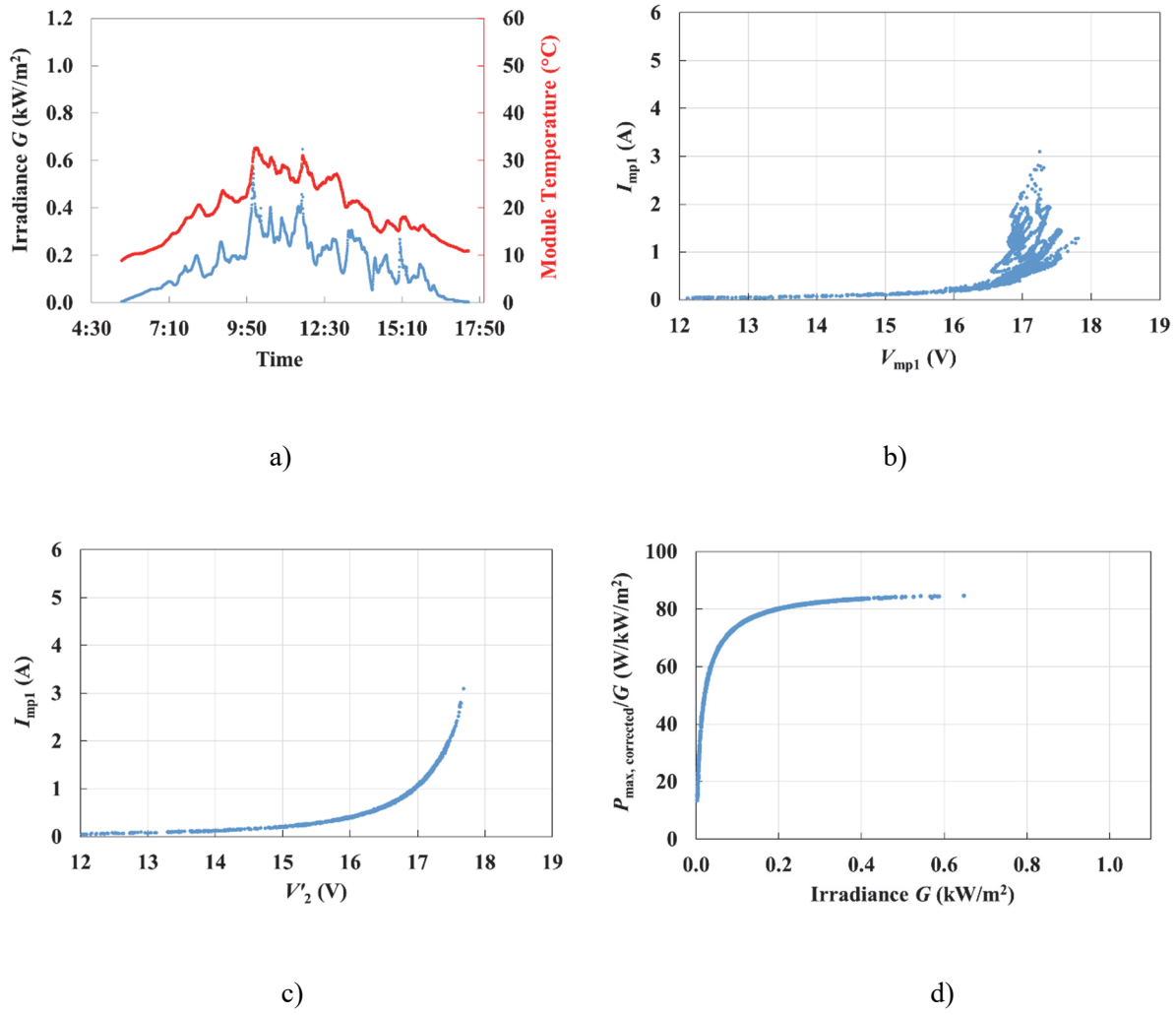

Figure 3.8. a) Experimental I_{sc} and module temperature on a cloudy day, b) experimental I_{mp} vs. V_{mp} plot, c) I_{mp} vs. V_{mp} plot corrected to 25 °C (V'_2) by using Eq. (3.16), and d) $P_{max,corrected}/G$ vs. G plot. $P_{max,corrected}$ was calculated using $P_{max,corrected.} = V'_2 \times I_{mp}$.

3.3 Research Originality

In Chapter 4, the temperature and irradiance dependences of the current at maximum power I_{mp} and the voltage at maximum power V_{mp} of crystalline–silicon PV devices are investigated by experiments and numerical simulations based on a one–diode model. It is shown that the experimental I_{mp} is nearly constant for temperature variations at fixed irradiances, which agrees with the simulation results being within ±0.02 %/K over the range 273.15 – 343.15 K (0 – 70 °C) for the range of parameter settings that represent a typical commercial–crystalline silicon PV device. The experimental I_{mp} is nearly proportional to irradiance G at fixed temperatures, which also agrees with the simulation results indicating that the I_{mp}/G is nearly constant within ±1.3 % for the irradiances range between 0.5 and 1.2 kW/m^2. Based on these results, new formulas for the temperature correction of V_{mp} are proposed. The importance of the new formula is that it does not require advanced information of diode parameters, temperature coefficients, and no specific software is required for parameter fitting. The I_{mp}–V_{mp} curves, which are measured outdoors and corrected to 25 °C by using the formulas, show good reproducibility within ±0.13 % for many days, which confirm the validity of the formula. The maximum power P_{max} can also be precisely estimated from the temperature correction of V_{mp}. These results are useful for characterizing the performance of crystalline–silicon PV devices by using the I_{mp} and V_{mp} values, which can be measured during their MPPT operation. Here, the originality of the present study is the development of new formulas for the temperature correction of V_{mp}, based on the consideration by using theoretical expressions of the I–V curve of p–n–junction diodes, as well as experimental evidence that I_{mp} is practically independent of temperature.

In Chapter 5, detection of shading effect by using the I_{mp} and V_{mp} for crystalline–silicon PV module was investigated. Estimating of the performances of PV modules and systems by using continuous monitoring data is an important issue, because the output power of PV modules is changeable, affected by the irradiance, module temperature, and shading effect, as well as degradation. This work proposes a method to detect partial shading on a module during its MPPT operation. It identifies, whether there is shading on a module or not, by analyzing data of the voltage at the V_{mp} and the I_{mp}. The developed temperature correction formulas for the V_{mp} and I_{mp} are used, in order to analyze them under various temperatures and irradiances. The experimental and simulation results show that the shading effect usually results in larger V_{mp} than the shadeless case, compared at the same I_{mp}. Therefore, the I_{mp}–V_{mp} curve is shifted toward higher voltages by the shading effect, thereby enabling detection of the existence of the shading effect. A method to identify the shading effects on a PV module from the I_{mp}–V_{mp} curve has been clarified, without requiring I–V curve measurements. Slight partial shading such as a drop in the photocurrent of a single cell in a module by about 5 – 10 % is possibly detected. The present results

are also applicable to PV systems that include multiple modules. These are expected to be useful for accurately monitoring the performances of PV modules and systems under operating conditions, because V_{mp} and I_{mp} can be measured without interrupting the MPPT operation. In Chapter 5, the originality of the present study is the finding of an increase in V_{mp} under slight partial shading, as well as the experimental method to detect such slight partial shading by using an I_{mp}–V_{mp} plot.

In Chapter 6, various types of deteriorations and failures that occur in PV modules during their outdoor operation including cell cracks, increase in series resistance, and PID are considered. Sensitive detection of them is essential to improve the efficiency and reliability of PV modules and systems. Previous detection techniques such as the *I–V* curve measurements have a problem because they needed to interrupt the MPPT operation of the PV system. This section proposes a new method to detect those degradations and failures without interrupting the MPPT operation by using the time–series data of the V_{mp} and I_{mp}. The V_{mp} and I_{mp} are corrected for temperature using the recently developed temperature correction formulas, and they are analyzed using the I_{mp}–V_{mp} curves. It is shown that the existence of a cracked cell in a PV module can be sensitively detected using the I_{mp}–V_{mp} curve, because the decrease in the photocurrent of a cracked cell tends to shift a part of the I_{mp}–V_{mp} curve of the module toward higher voltages. The experimental and simulation results indicate that a small cell crack, less than 10% of the cell area, can be detected. The simulation results also show that the increase in series resistance can be detected by the distortion of the I_{mp}–V_{mp} curve toward a lower voltage in the high I_{mp}, or high irradiance, region. In addition, the simulation results illustrate that PID affects the I_{mp}–V_{mp} curves. These simulation results indicate that the present method is very powerful for detecting the degradation and failure of PV modules and systems. The originality of the present study related to this chapter 6 is the proposal and demonstration of the usefulness of the I_{mp}–V_{mp} curve for detecting frequently–observed degradation modes of PV modules, such as cell crack, increase in R_s, and PID.

Chapter 4

Temperature and irradiance dependences of the I_{mp} and V_{mp} of crystalline–silicon PV devices and new translation formulas

4.1 Introduction

Temperature and irradiance are among the influential factors upon the performance of PV devices, which mainly affect the output voltage and output current of the PV devices. Usually, PV systems operate under various temperatures and irradiances. On the other hand, the module specifications are usually defined at the STC; irradiance of 1 kW/m^2 and module temperature of 25 °C (IEC 60904-3, 2016). Various kinds of mathematical models for the temperature and irradiance dependences of the *I–V* characteristics and performance parameters of PV modules have been discussed so far [9-14]. They proposed novel models of the *I–V* curves, and extracted the performance parameters from the experimental curves by using the models, and predicted the *I–V* curves and maximum power (P_{max}) under various temperature and irradiance conditions. Models for extracting diode parameters based on the data–sheet specifications and predicting the temperature and irradiance dependencies of PV devices have also been proposed [41-43]. Analysis of the translation equations by using numerical fitting of parameters based on numerous outdoor data were also studied [15-21].

During the PV systems' MPPT operations, only the I_{mp} and V_{mp} are measurable. Because the I_{mp} and V_{mp} are dependent on the module temperature and irradiance, translation equations for them are necessary for characterizing the performance of PV devices under MPPT operation. Previous studies [22-27] discussed I_{mp} and V_{mp}, based on the experimental results of the *I–V* curve. The IEC standard (IEC 60891, 2009) also describes the *I–V* curve translation procedures for irradiance and temperature [25]. However, they require a set of *I–V* curves under different irradiance (G) maintaining temperature (T) and under different T maintaining G to compute the correction parameters. They also require experimental *I–V* curves and the TC of the short–circuit current (I_{sc}), open–circuit voltage (V_{oc}) and other correction factors. Recently, a novel formula for temperature translation was proposed by Hishikawa et al., 2018 [26]. They proposed the TC of the *I–V* curves of PV devices as a function of temperature and voltage, based on the one–diode model.

There have also been many studies of I_{mp} and V_{mp} based on numerous experiments [11, 12, 14-16, 17-21, 40, 44]. The I_{mp} is usually expressed as a quasi–bilinear function of module temperature and

solar irradiance [14]. Some of these studies have discussed the TC of I_{mp} and V_{mp} based on empirical equations. For example, Moser et al., 2014 [40], discussed the TC of I_{mp} and V_{mp} for various PV technologies based on onsite data. They usually required many of data to empirically derive the TC for each PV module or each PV system. Recently, a methodology called Suns–Vmp method was proposed [28, 29], which enabled monitoring and diagnosis of PV system degradation using only the values at MPP. This method requires datasheet information for the initial values, and it must also extract the diode parameters by using specific software for numerical–fitting in order to evaluate their performance.

This chapter analytically and experimentally investigates expressions for the temperature and irradiance dependences of I_{mp} and V_{mp} of commercial crystalline–silicon PV devices, which do not need parameter fitting. New formulas for the temperature correction of experimental V_{mp} data have also been investigated. The novelty of the present study is that these formulas do not require advanced information of TC, diode parameters, or *I–V* curve parameters, and no specific software is required. The results lead to translation of the I_{mp} and V_{mp} values with improved its precision, and these can be utilized to analyze the maximum output power from the system–monitoring data.

This chapter describes the experiments and simulations of I_{mp}, which discusses the experimental TC of the I_{mp} for both outdoor and indoor experiments. The formulas for I_{mp} and V_{mp} are expressed by using the one–diode model. The simulations of temperature and irradiance dependences of I_{mp} are described. Then, the new translation formulas are proposed, and these formulas are utilized for outdoor experimental data. Finally, a chapter summary is presented.

4.2 Experiments and Simulations of I_{mp}

4.2.1 Experimental TCs of I_{mp}

Although the TC of I_{mp} has not been well established in previous studies and is not specified in the standards such as the IEC 60891, 2009, many previous experimental results on the temperature dependence of I_{mp} have shown small values of TC in the range between -0.0402 %/K and 0.0339 %/K [14, 16, 17, 19, 20, 27]. Therefore, the TC of I_{mp} should not be considered equal to the TC of the short–circuit current I_{sc}.

Figures 4.1 and 4.2 show the temperature dependence of the experimental I_{mp} for a 36–cell series–connected mono–crystalline–silicon PV module (Sharp, model: NT-84L5H). The outdoor experiment

was carried out at the National Institute of Advanced Industrial Science and Technology (AIST), Tsukuba, Japan. An experimental *I–V* data–set, recorded with a sampling interval of 20 seconds during the period April 1 – 30, 2015, has been investigated. The PV module temperature was measured at six points at the back side of the module, of which the average represents as the module temperature. Details of the measurements are described in references [45-47]. Figures 4.1(a) and 4.1(b) show the outdoor measurement results of the I_{mp} versus module temperature. The experimental results of I_{mp} for irradiance levels around 1 kW/m^2 (between 0.995 and 1.005 kW/m^2) for 15 days, and irradiance levels around 0.5 kW/m^2 (between 0.495 and 0.505 kW/m^2) over 19 days, are plotted versus the module temperature. The figure indicates that the I_{mp} is nearly constant in the range of temperature. The TCs of the I_{mp} based on the outdoor measurements are estimated to be -0.0028 and -0.0014 A/K (or relative -0.06 %/K) for irradiance levels of around 1 and 0.5 kW/m^2, respectively. Indoor measurements of the same module were performed at an irradiance of 1 kW/m^2 after the module was stabilized by outdoor exposure, as shown in Fig. 4.2. The result shows that the I_{mp} is nearly constant with a TC of -0.0014 A/K (or relative -0.03 %/K) for the temperature range between 283.15 K (10 ºC) and 338.15 K (65 ºC). These results agree with those previously obtained results [20, 27].

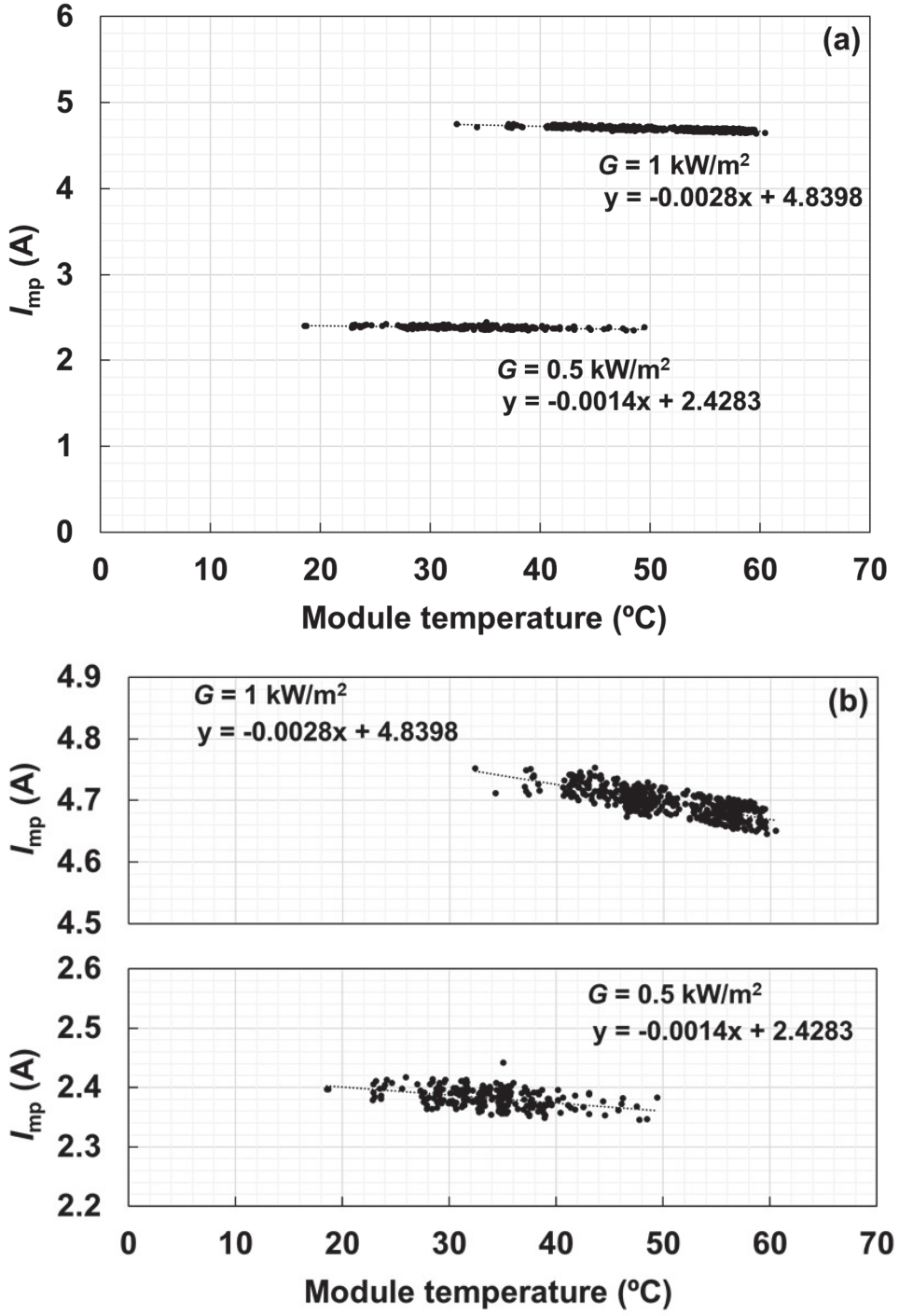

Figure 4.1. (a) Outdoor experimental results of I_{mp} vs. module temperature at irradiance levels around 1 kW/m^2 and 0.5 kW/m^2. See the text for details. Linear regression lines are also shown. (b) Expansion of (a)

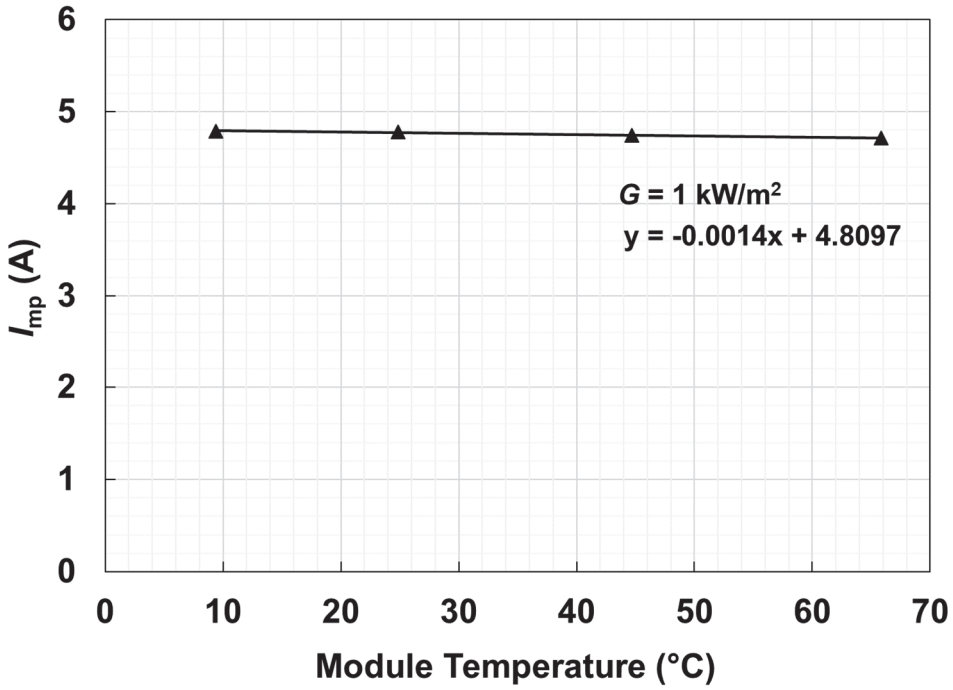

Figure 4.2. Indoor experimental results of I_{mp} vs. module temperature at irradiance level equal to 1 kW/m^2. A linear regression line is also shown.

4.2.2 Formulas for I_{mp} and V_{mp}

The output current I of a PV device can be approximately expressed as follows based on the single diode model, when $I_{sc} >> I_0$ is satisfied:

$$I = I_{sc} - I_0 \exp\left(\frac{q(V+IR_s)}{N_c nkT}\right) - \frac{V+IR_s}{R_{sh}}. \quad (4.1)$$

Here, I_{sc} is the short–circuit current, I_0 is the diode reverse–saturation current, q is the electron charge, V is the output voltage, R_s is the series resistance, N_c is the number of series–connected cells in the module, n is the diode ideality factor, k is the Boltzmann's constant, T is the device temperature in Kelvin, and R_{sh} is the shunt resistance.

At the MPP, Eq. (4.1) can be expressed as follows:

$$I_{\mathrm{mp}} = I_{\mathrm{sc}} - I_0 \exp\left(\frac{q(V_{\mathrm{mp}}+I_{\mathrm{mp}}R_s)}{N_{\mathrm{c}}nkT}\right) - \frac{V_{\mathrm{mp}}+I_{\mathrm{mp}}R_{\mathrm{s}}}{R_{\mathrm{sh}}}. \tag{4.2}$$

The derivative of V with respect to I at the MPP leads to the following equation,

$$-\left.\frac{\partial V}{\partial I}\right|_{\mathrm{mp}} = \frac{1+\frac{q}{N_{\mathrm{c}}nkT}I_0R_{\mathrm{s}}.\exp\left(\frac{q(V_{\mathrm{mp}}+I_{\mathrm{mp}}R_{\mathrm{s}})}{N_{\mathrm{c}}nkT}\right)+\frac{R_{\mathrm{s}}}{R_{\mathrm{sh}}}}{\frac{1}{R_{\mathrm{sh}}}+\frac{qI_0}{N_{\mathrm{c}}nkT}.\exp\left(\frac{q(V_{\mathrm{mp}}+I_{\mathrm{mp}}R_{\mathrm{s}})}{N_{\mathrm{c}}nkT}\right)}. \tag{4.3}$$

At the MPP, the following are also satisfied:

$$\left.\frac{\partial(I\times V)}{\partial I}\right|_{\mathrm{mp}} = 0\,, \tag{4.4}$$

$$\therefore -\left.\frac{\partial V}{\partial I}\right|_{\mathrm{mp}} = \frac{V_{\mathrm{mp}}}{I_{\mathrm{mp}}}. \tag{4.5}$$

An implicit relation of I_{mp} and V_{mp} which excludes the I_{sc} is as follows:

$$I_{\mathrm{mp}} = V_{\mathrm{mp}} \cdot \frac{\frac{1}{R_{\mathrm{sh}}}+\frac{qI_0}{N_{\mathrm{c}}nkT}.\exp\left(\frac{q(V_{\mathrm{mp}}+I_{\mathrm{mp}}R_{\mathrm{s}})}{N_{\mathrm{c}}nkT}\right)}{1+\frac{R_{\mathrm{s}}}{R_{\mathrm{sh}}}+\frac{qI_0R_{\mathrm{s}}}{N_{\mathrm{c}}nkT}.\exp\left(\frac{q(V_{\mathrm{mp}}+I_{\mathrm{mp}}R_{\mathrm{s}})}{N_{\mathrm{c}}nkT}\right)}. \tag{4.6}$$

The plot of I_{mp} versus V_{mp} at 25 ºC is shown in Fig. 4.3 (red line). The I_{mp} is calculated by Eq. (4.6) with typical parameters of a five–inch crystalline–silicon PV cell at R_{s} = 5 mΩ/cell, R_{sh} = 5 Ω/cell, n =

1.1, and $I_0 = 1.743\times10^{-9}$ A. The *I–V* curves of the cell at five irradiance levels are also shown in the figure.

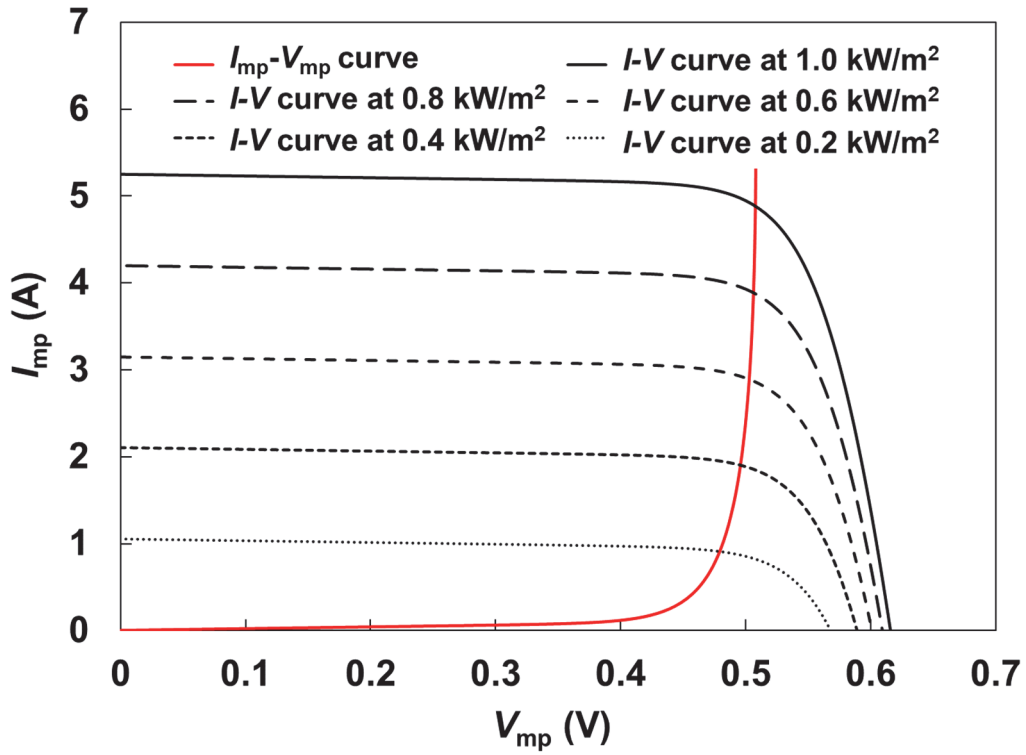

Figure 4.3. Example of the I_{mp} vs. V_{mp} curve (red line) at 25 °C of a crystalline–silicon PV cell, calculated from Eq. (4.6). The *I–V* curves at five irradiance levels for $R_s = 5$ mΩ/cell, $R_{sh} = 5$ Ω/cell, $n = 1.1$, and $I_0 = 1.743\times10^{-9}$ A at 25 °C are also shown.

4.2.3 Simulation of the temperature and irradiance dependences of I_{mp}

If the temperature dependence of I_{sc} is expressed as I_0 in Eq. (4.2), the I_{mp} can be obtained as follows:

$$I_{mp} = I_{sc} + \alpha I_{sc}(T - T_0) - A \cdot \exp\left(\frac{q(V_{mp}+I_{mp}R_s)}{N_c nkT} - \frac{E_g}{kT}\right) - \frac{V_{mp}+I_{mp}R_s}{R_{sh}}. \quad (4.7)$$

In Eq. (4.7), α is the relative temperature coefficient of I_{sc} (1/ºC), and T_0 is 25 °C (298.15 K). The temperature dependence of I_0 is expressed as $I_0 = A \cdot \exp\left(\frac{-E_g}{kT}\right)$ [48], which relates to the product of the electron and hole concentrations [23, 38]; in this study, A is assumed to be independent of temperature [49, 50]. E_g is the bandgap energy of silicon; it is also assumed to be constant at 1.12 eV, as described in the references Sze and Ng, 2006 [23] and Green, 1982 [50]. It is noted that because E_g is actually temperature dependent (e.g., between -2.58×10^{-4} and -4×10^{-4} eV/°C [51-53]), the assumption of constant E_g will affect the value of n in Eq. (4.7).

Figure 4.4 shows the simulation results for the temperature dependence of I_{mp} under an irradiance of 1 kW/m^2 for a PV module, which is normalized by its STC value, for various values of R_s, R_{sh}, and n, as calculated by Eq. (4.7). The I_{sc} and α were assumed to be 33.72 mA/cm^2 and 0.05 %/K, respectively. The parameters R_s, R_{sh}, and n were simultaneously varied in the matrix, and 1728 combinations were simulated. The corresponding values of fill factor FF and open–circuit voltage V_{oc} at STC ranged between 0.74 and 0.81 and between 0.62 V and 0.72 V, respectively, which cover the range of values of typical commercial crystalline–silicon PV devices. The results in Fig. 4.4 show that the maximum value is 1.01381 (R_s = 3 mΩ/cell, R_{sh} = 5 Ω/cell, n = 1, V_{oc} at STC = 0.72 V/cell, FF at STC = 0.81) and minimum value is 0.98498 (R_s = 7 mΩ/cell, R_{sh} = ∞ Ω/cell, n = 1.3, V_{oc} at STC = 0.62 V/cell, FF at STC = 0.74), this indicates that the variation of I_{mp} is within ±1.4 % over the range 273.15 – 343.15 K (0 – 70 °C), or TC of within ±0.02 %/K, for typical crystalline–silicon PV devices. These simulation results show small TC, which agree with experimental results shown in Figs. 4.1 and 4.2, and also with previous studies [14, 16, 17, 19, 20, 27]. Slight differences between the experimental results (-0.06 %/K and -0.03 %/K) and the simulation results (±0.02 %/K) possibly originate from their slight temperature dependence of parameters such as A, n, and E_g, which were neglected in the present simulation, as well as the experimental error.

Based on the Eq. (4.7), the irradiance dependence of I_{mp} was also simulated at T = 25 ºC, of which the results are shown in Fig. 4.5. Parameters R_s, R_{sh}, and n were simultaneously varied in a matrix, covering the same combinations as in Fig. 4.4. The maximum and minimum values of I_{mp}/G, which are normalized to their value at 1 kW/m^2, are 1.00374 at the irradiance of 1.2 kW/m^2 and 0.97745 at the irradiance of 0.5 kW/m^2 (R_s = 3 mΩ/cell, R_{sh} = 5 Ω/cell, n = 1, V_{oc} at STC = 0.72 V/cell, FF at STC = 0.81), respectively. This indicates that the I_{mp}/G is within ±1.3 % for the irradiance range between 0.5 and 1.2 kW/m^2. It is noted that the irradiance dependence of I_{mp} is mainly affected by R_{sh}, followed by R_s and n. The results show that the I_{mp} is nearly proportional to irradiance, which agrees with the results of previous experimental studies [12, 17-19, 44].

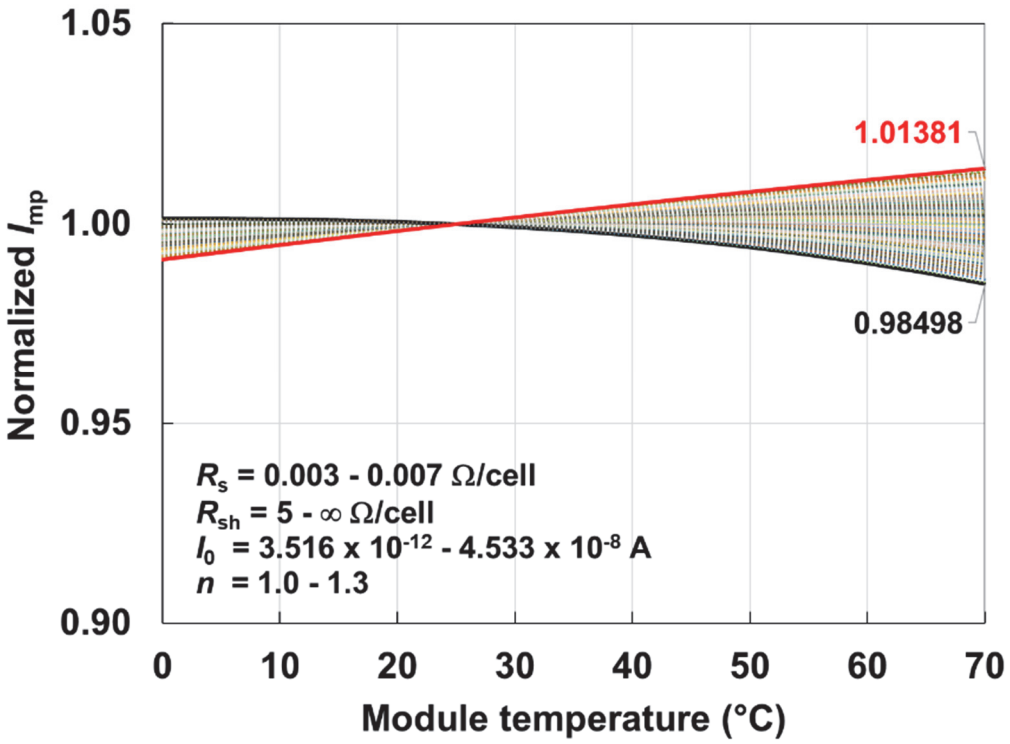

Figure 4.4. Normalized I_{mp} vs. module temperature for G = 1 kW/m^2, R_s between 3 and 7 mΩ/cell, R_{sh} between 5 Ω/cell and infinity, n between 1.0 and 1.3, and α = 0.05 %/K, calculated using Eq. (4.7). All parameters were varied simultaneously in the matrix, and 1728 combinations were simulated. The results show that the maximum value = 1.01381 and the minimum value = 0.98498. Therefore, the TC of I_{mp} is within ±0.02 %/K.

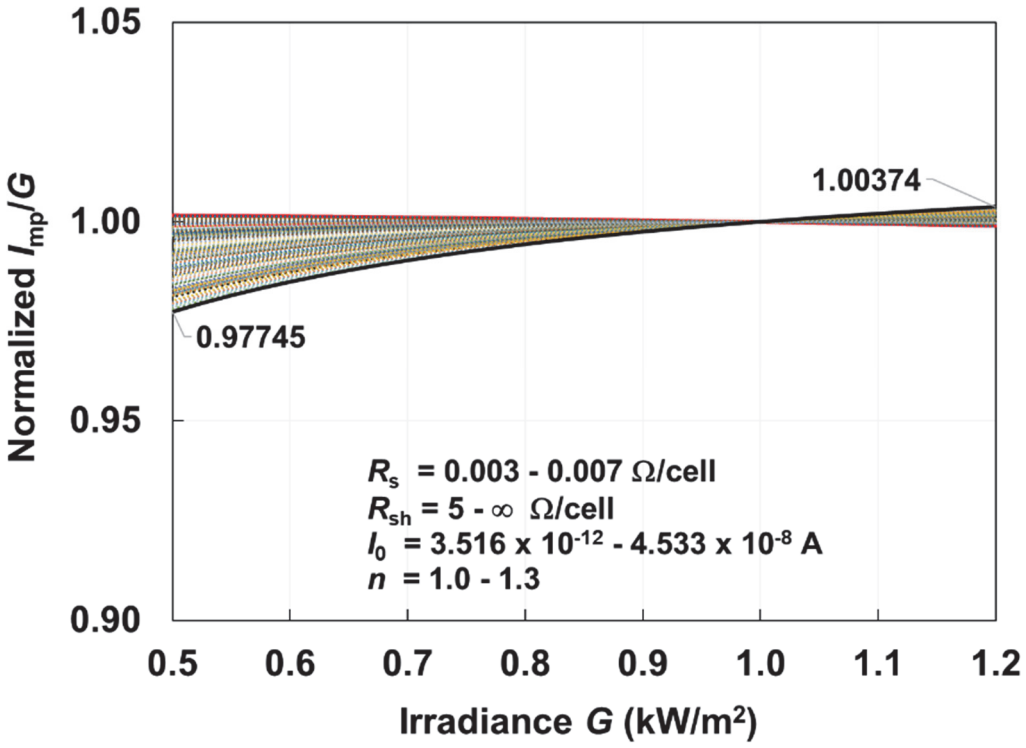

Figure 4.5. Normalized I_{mp}/G vs. irradiance G at 25 ºC, for R_s between 3 and 7 mΩ/cell, R_{sh} between 5 Ω/cell and infinity, and n between 1.0 and 1.3. All the parameters were simultaneously varied in the matrix, and 1728 combinations were simulated. The results show that the maximum value = 1.00374 and the minimum value = 0.97745. Therefore, the I_{mp}/G is within ±1.3 %.

4.3 Translation Equations of V_{mp} and I_{mp}

As discussed in Section 4.2, the experimental results of I_{mp} and the simulated I_{mp} by using Eq. (4.7) are both nearly constant under a wide range of temperatures (0 – 70 °C). Based on these results, the present study simply approximates that the TC of the I_{mp} is very small that can be neglected. The TC of the I–V curve has recently been shown to be expressible as follows [26]:

$$V_2 = V_1 + \frac{T_2 - T_1}{T_1}\left(V_1 - \frac{nE_g}{q} \cdot N_c\right). \tag{4.8}$$

In Eq. (4.8), T_1 and V_1 are the measured temperature and measured the output voltage, respectively. T_2 is the target temperature. V_2 is the output voltage at T_2. N_c is the number of series–connected cells. Equation (4.8) is useful for the temperature correction of *I–V* curves, because it does not require advance information on the *I–V* curve's parameters or diode's parameters. It is valid for solar cells which follow the one–diode model Eq. (4.1) when the I_{sc} and output current are constant [39]. However, the I_{sc} is temperature dependent, and it is significant as $I_{sc}\cdot\alpha\,(T_2\text{-}T_1)$. Here, α is the TC of I_{sc}, which is assumed to be 0.05 %/K [39, 50]. Figure 4.6 illustrates the *I–V* curves at temperatures of T_1 and T_2. The black and red lines are the curves at T_1 and T_2 under an irradiance of 1 kW/m^2, respectively. The blue line is the curve at T_2 under an irradiance of $1+\alpha\,(T_2\text{-}T_1)$ kW/m^2, this yields the curve for which I_{sc} is equal to I_{sc1} (I_{sc1}=I'_{sc2}). Therefore, the voltage of the blue curve at the output current of I_{mp1} can be expressed as V'_2, and V'_2 can be expressed as

$$V'_2 = V_{mp1} + \frac{T_2-T_1}{T_1}\left(V_{mp1} - \frac{nE_g}{q}\cdot N_c\right). \tag{4.9}$$

When slight differences between I_{sc1} and I_{sc2}, due to the temperature dependence of I_{sc} (α = 0.05 %/K), are considered, the relation of V_2' and V_{mp2}, which is the maximum power voltage at T_2 under 1 kW/m^2 irradiance, are expressed as follows. If the R_s and R_{sh} in Eq. (4.2) are neglected, the following relations hold:

$$V'_2 = \frac{N_c nkT_2}{q}\ln\left(\frac{I_{sc1}-I_{mp1}}{I_0}\right), \tag{4.10}$$

$$V_{mp2} = \frac{N_c nkT_2}{q}\ln\left(\frac{I_{sc2}-I_{mp1}}{I_0}\right), \tag{4.11}$$

$$\therefore V_{mp2} = V'_2 + \frac{N_c nkT_2}{q}\ln\left(\frac{I_{sc2}-I_{mp1}}{I_{sc1}-I_{mp1}}\right). \tag{4.12}$$

If the instability or degradation of the module is neglected, the I_{sc1} and I_{sc2} in Eq. (4.12) can be estimated from the temperature, irradiance *G*, and the module's specifications. However, The I_{sc} of PV

modules sometimes degrades due to various reasons in outdoor operation. Therefore, a formula without I_{sc} is preferable if the I_{sc} is considered that it possibly degrades. Therefore, a temperature–correction formula for V_{mp} which includes only measurable data is desirable. If the slope of the *I–V* curves around (V_{mp2}, I_{mp2}) and (V'_2, I'_2) in Fig. 4.6, are assumed that they are nearly the same, the following approximate equation is obtained:

$$-\frac{\partial V}{\partial I}\Big|_{V=V_{\mathrm{mp2}}} \cong \frac{V'_2}{I_{\mathrm{mp1}}}\Big|_{V=V'_2} \cong \frac{\Delta V}{\Delta I}, \tag{4.13}$$

$$\therefore \Delta V \equiv V'_2 - V_{\mathrm{mp2}} \cong V'_2 \frac{\Delta I}{I_{\mathrm{mp1}}}. \tag{4.14}$$

Here, the ΔI and ΔV are the difference of current and voltage, respectively, between the blue and red *I–V* curves in Fig. 4.6, which are depicted in Fig. 4.6 (b). The Eq. (4.14) corresponds to the approximate form of Eq. (4.12), in which the second and higher order terms in the Taylor expansion of ΔV are neglected as follows:

$$\Delta V \equiv V'_2 - V_{\mathrm{mp2}} = \frac{-N_{\mathrm{c}} n k T_2}{q} \ln\left(\frac{I_{\mathrm{sc2}} - I_{\mathrm{mp1}}}{I_{\mathrm{sc1}} - I_{\mathrm{mp1}}}\right) = \frac{N_{\mathrm{c}} n k T_2}{q} \ln\left(\frac{I_{\mathrm{sc1}} - I_{\mathrm{mp1}}}{I_{\mathrm{sc2}} - I_{\mathrm{mp1}}}\right)$$

$$= \frac{N_{\mathrm{c}} n k T_2}{q} \ln\left(1 + \frac{I_{\mathrm{sc1}} - I_{\mathrm{sc2}}}{I_{\mathrm{sc2}} - I_{\mathrm{mp1}}}\right) \cong \frac{N_{\mathrm{c}} n k T_2}{q} \left[\frac{\Delta I}{I_{\mathrm{sc2}} - I_{\mathrm{mp1}}} - \frac{1}{2}\left(\frac{\Delta I}{I_{\mathrm{sc2}} - I_{\mathrm{mp1}}}\right)^2 + \cdots\right]. \tag{4.15}$$

By using the relation of Eq. (3.9),

$$\therefore \Delta V \equiv V'_2 - V_{\mathrm{mp2}} \cong \frac{N_{\mathrm{c}} n k T_2}{q} \frac{\Delta I}{I_{\mathrm{sc2}} - I_{\mathrm{mp1}}} = V'_2 \frac{\Delta I}{I_{\mathrm{mp1}}}. \tag{4.16}$$

In this study, the I_{mp} is considered to be temperature independent. When the R_s is small, the ΔI can be expressed as follows,

$$\Delta I \cong I_{sc} \cdot \alpha(T_2 - T_1), \tag{4.17}$$

Therefore, the difference between the V'_2 and V_{mp2} is estimated by using the following relationship.

$$\therefore \Delta V \cong V'_2 \times \frac{I_{sc} \cdot \alpha(T_2 - T_1)}{I_{mp1}}. \tag{4.18}$$

Considering that I_{sc}/I_{mp} usually range between 1.05 and 1.07 [12, 39] in Eq. (4.18), it can be approximated as follows:

$$\frac{I_{sc}}{I_{mp}} \approx 1. \tag{4.19}$$

Therefore, the ΔV are expressed as follows.

$$\therefore \Delta V \cong V'_2 \times \alpha(T_2 - T_1). \tag{4.20}$$

Then, the temperature correction equation for V_{mp} is finally obtained as

$$V_{mp2} \cong V'_2 + V'_2 \times \alpha(T_2 - T_1), \tag{4.21}$$

$$\therefore V_{mp2} \cong \left[V_{mp1} + \frac{T_2 - T_1}{T_1}(V_{mp1} - \frac{nE_g}{q} \cdot N_c)\right] \times [1 + \alpha(T_2 - T_1)]. \tag{4.22}$$

As the previous section has discussed, the TC of I_{mp} is very small, and the I_{mp} can be written as follows:

$$I_{\mathrm{mp2}} \cong I_{\mathrm{mp1}}. \tag{4.23}$$

Equation (4.22) is a formula for temperature correction of V_{mp}, which is developed to improve the correction precision from the fundamental temperature dependence of silicon solar cell. The $[1+\alpha(T_2-T_1)]$ in Eq. (4.22) corresponds to the finding of this study that the I_{mp} is nearly independent of temperature. The equation indicates that the TC of V_{mp} is not constant and actually depends on V_{mp} itself. Although the variation in TC of V_{mp} has been discussed in the references [14, 16, 17, 20, 40, 44], the present study proposes a new formula that explicitly considers its voltage–dependence. This requires the values of nE_g/q and α, which can be reasonably estimated without previous experiments. The nE_g/q and α can be estimated from the fundamental characteristics of the silicon p–n–junction, which is discussed in this section in relation to the outdoor experiments. Because the I_{sc}/I_{mp} is not exactly unity, the approximation of Eq. (4.19) will cause slight error in ΔV. The derivation of Eq. (4.22) also includes other approximations such as assumption of negligible R_s and Eq. (4.14), as already discussed. However, the approximate formula has sufficient accuracy to be used in various kinds of analysis of V_{mp}, as demonstrated in this chapter and also in later chapters.

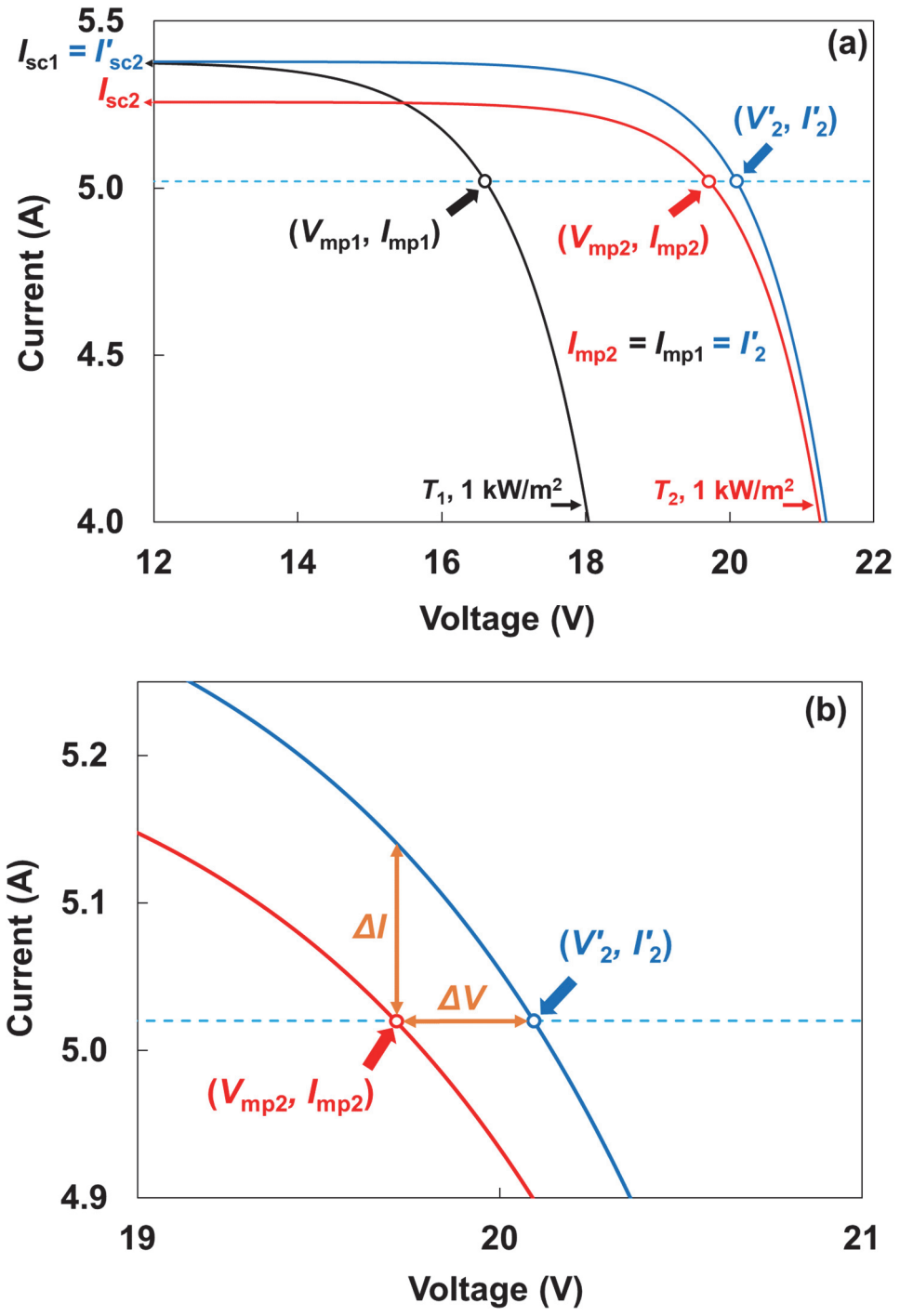

Figure 4.6. (a) The black and red lines illustrate the *I*–*V* curves of a PV modules under an irradiance of 1 kW/m^2 at 70 ºC and 25 ºC, respectively. The blue line shows the curve under 1+α(70-25) kW/m^2 at 25 ºC. (b) Expansion of (a) around (V_{mp2}, I_{mp2}).

The following discussion uses Eqs. (4.22) and (4.23), based on the outdoor experimental V_{mp} of the same mono–crystalline–silicon PV module as in Figs. 4.1 and 4.2, which was measured in April 2015. The value of nE_g/q is estimated to be 1.232 V [26], which also agrees with the best–fit to outdoor experimental data. This corresponds to an n of 1.1, when the silicon band–gap energy of 1.12 eV [23, 48] is assumed. It is noted that the value of n is affected by the assumption of a temperature–independent E_g, as mentioned in Section 4.2. However, the product of n and E_g is the only adjustable parameter, because other parameters are directly measurable such as V_{mp1}, V_{mp2}, T_1, T_2, q is a fundamental parameter, and α is typical TC of crystalline–silicon solar cell. Equation (4.22) is useful for crystalline–silicon p-n–junction technologies, because the calculation value of nE_g/q fixed to 1.232 V agrees well with the experimental result of TC of the crystalline–silicon PV modules [26].

The black and red lines in Fig. 4.7 show examples of the irradiance and module temperature, respectively, on a clear sunny day and a cloudy day. Figure 4.8 shows the measured I_{mp} (I_{mp1}) versus measured V_{mp} (V_{mp1}) and corrected V_{mp} (V_{mp2}) for those the same days in Fig. 4.7. The data between 6:00 and 6:30 am and data after 3:30 pm on the clear sunny day were neglected, because they were affected by shading from nearby objects. The curves show agree well for the clear sunny day and cloudy day after the temperature correction to 25 ºC, which are indicated by the red and purple lines. The standard deviation σ of V_{mp2} in the irradiance range of 1.0 ±0.05 kW/m^2 was 0.02 V, or relative 0.13 %. The figure also shows that the V_{mp2} is nearly constant in the I_{mp1} range between 2.4 and 4.7 A, which corresponds to the irradiance range of 0.50 – 1.01 kW/m^2, and its σ was 0.08 V, or relative 0.47 %. Figure 4.9 shows the timeline data of Fig. 4.8 for the clear sunny day. The data of I_{mp} and V_{mp} over 28 days in April 2015 after correction to 25 °C are shown in Fig. 4.10. The blue symbols show the I_{mp}–V'_2 curves corrected by the previous I–V curve translation Eq. (4.9). The red symbols show the I_{mp}–V_{mp2} curves corrected by using the developed Eq. (4.22) of this study. The standard deviations σ of voltage in the irradiance range of 1.0 ±0.05 kW/m^2 was improved from the 0.07 V (relative 0.38 %) of Eq. (4.9) to 0.02 V (relative 0.13 %) of Eq. (4.22). The importance of the σ was 0.02 V of V_{mp2} by Eq. (4.22) is not only the excellent reproducibility but also shows to agree well with the I_{mp}–V_{mp} point at STC is shown by a green diamond; I_{mp} = 4.80 A and V_{mp} = 17.82 V. Furthermore, the low relative reproducibility of the corrected values can more precisely identify I_{mp}–V_{mp} curve's distortions that will be present in the next chapters.

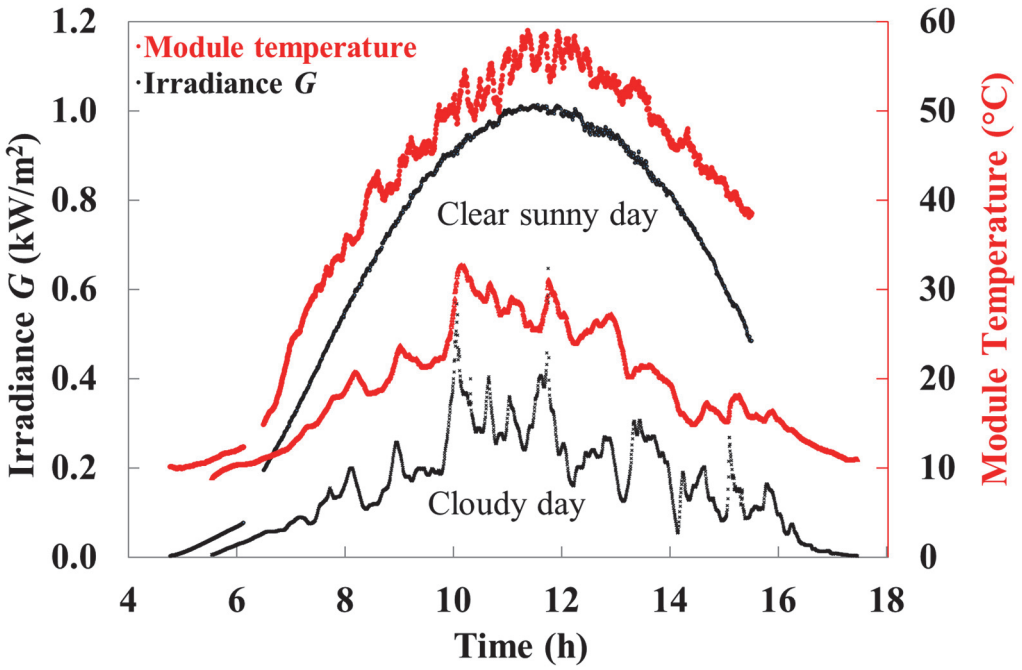

Figure 4.7. Irradiance G and module temperature on a clear sunny day and a cloudy day.

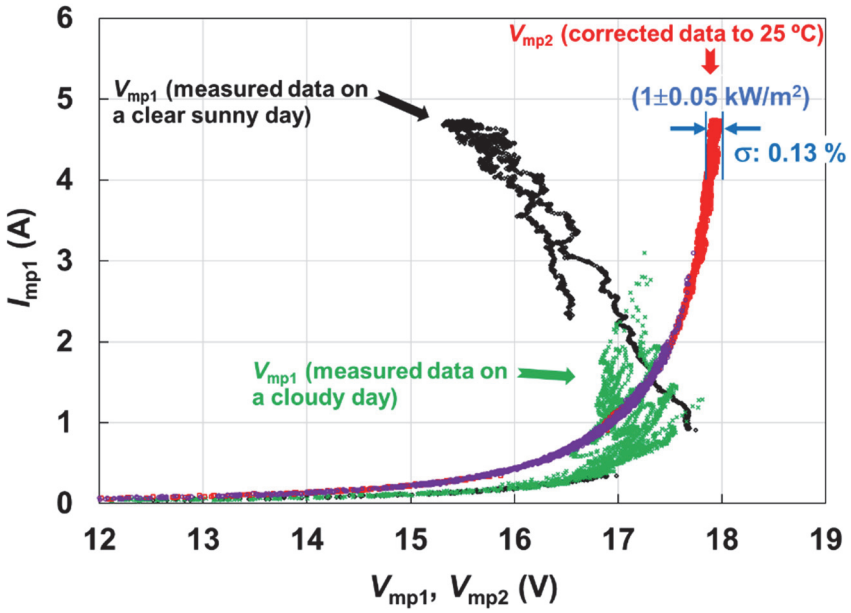

Figure 4.8. Experimental I_{mp} (I_{mp1}) vs. measured V_{mp} (V_{mp1}) and corrected V_{mp} (V_{mp2}) on the same days as in Fig. 4.7. The black and red symbols show the I_{mp1} vs. V_{mp1} and V_{mp2} on a clear sunny day, respectively. The green and purple symbols show the I_{mp1} vs. V_{mp1} and V_{mp2} on a cloudy day, respectively.

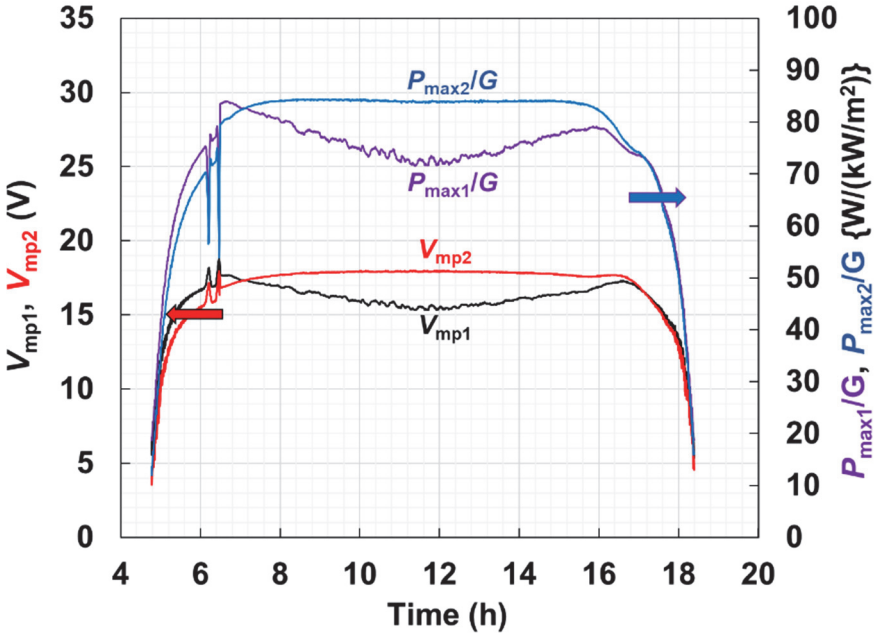

Figure 4.9. Experimental V_{mp1}, experimental P_{max1}/G, corrected V_{mp2}, and corrected P_{max2}/G plot as a function of time for the data on a clear sunny day in Fig. 4.8.

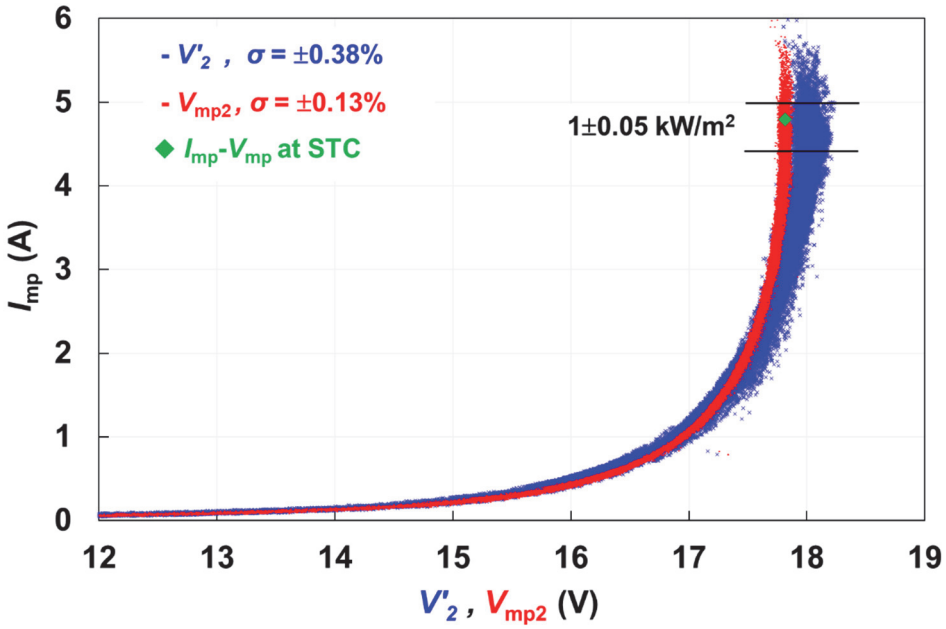

Figure 4.10 Experimental I_{mp}–V_{mp} curve results, the blue line is corrected by Eq. (4.9), the red line is corrected by the Eq. (4.22). Data for the I_{mp}–V_{mp} point at STC is shows in the green diamond.

Figure 4.11 shows P_{max2}/G at 25 °C versus irradiance of experimental data over 28 days in April 2015. Here, P_{max2} is the P_{max} after temperature correction, calculated as the product of V_{mp2} and I_{mp1} at 25 ºC. The σ of P_{max2} in the irradiance range of 1.0 ±0.05 kW/m^2 was 0.21 W, or relative 0.24 %. This good agreement confirms the validity of the correction formulas Eqs. (4.22) and (4.23).

Figure 4.12 shows a comparison of the data in Fig. 4.11 with the indoor measurement value of P_{max} at STC (P_{STC}), which shows good agreement of P_{max2} and P_{STC} about -1.5 % on average. The σ of (P_{max2}-P_{STC})/P_{STC} was 0.24 % in the irradiance range 1.0 ±0.05 kW/m^2. The possible origins of the remaining σ of 0.24 %, as well as the systematic deviation of (P_{max2}-P_{STC})/P_{STC} from 1.0, are the slight dependence of I_{mp} on temperature (as shown in Fig. 4.4), the approximate components of Eqs. (4.22) and (4.23), and deviations produced by differences in indoor and outdoor equipment, such as the *I–V* testers and their measurement connections with the PV module outdoor are longer, and more series' components. The significance of the present results over the previous works is that a good agreement with experiments such as Figs. 4.11 and 4.12 are obtained without information of TC or diode parameters based on advance measurements. It is noted that Equations (4.2) and (4.11) include diode parameters such as R_{sh} and I_0. However, the present results such as Eq. (4.22) require only the values of nE_g/q and α, which can be reasonably estimated without previous experiments, as discussed in the previous section. Although the assumption in Section 4.2 that the parameters are constant is an approximation, it is not a fundamental problem in this study, because the present results such as Eqs. (4.21) and (4.22) only includes nE_g/q and α. Furthermore, the very good correction reproducibility is observed by assuming constant values of nE_g/q = 1.232 V and α = 0.05 %/K. The uncertainty (k=2) of P_{max} determination from the I_{mp} and V_{mp} by using Eqs. (4.22) and (4.23), excluding that of PV reference device (~1.5 %, k=2), is tentatively estimated to be ~1.6 %, which mainly consists of element uncertainties (k=1) such as V_{mp} measurement (~0.5 %), I_{mp} measurement (~0.5 %), temperature measurement and temperature correction (~1 %). Detailed uncertainty analysis is left for future analysis.

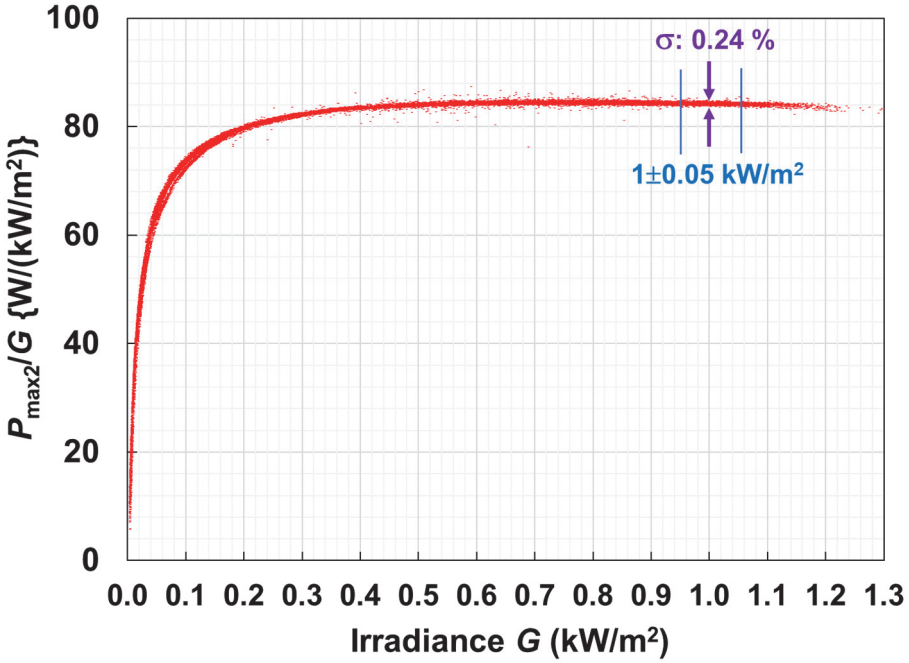

Figure 4.11. P_{max2}/G vs. irradiance G over 28 days. The standard deviation σ of P_{max2} is relative 0.24 % for the irradiance range of 1.0 ±0.05 kW/m^2.

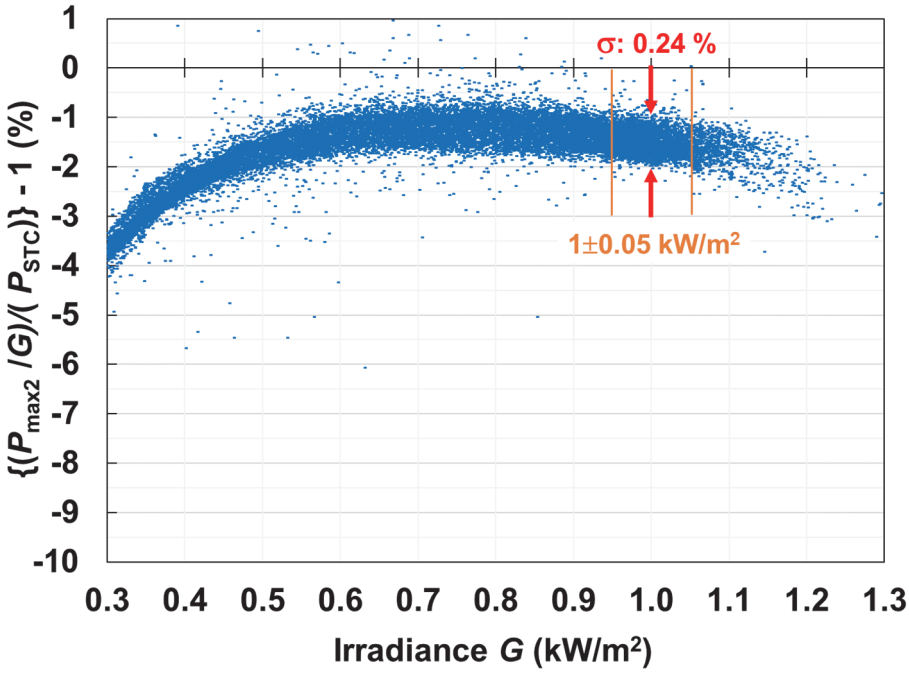

Figure 4.12. P_{max2}/G compared with the P_{STC} vs. irradiance G over 28 days. The typical reproducibility of P_{max2} is indicated by a standard deviation σ of 0.24 % for the irradiance levels 1.0 ±0.05 kW/m^2.

4.4 Chapter Summary

This study investigated the temperature dependence and irradiance dependence of I_{mp} and V_{mp} by using experiments and numerical simulations based on the one–diode model, and the following results were obtained.

The *I–V* curves were numerically simulated over the range of R_s, R_{sh}, I_0, n, and V_{oc} which are typical to commercial crystalline–silicon PV devices. The I_{mp} was shown to be nearly constant within ±0.02 %/K for temperature range between 273.15 and 343.15 K (0 – 70 °C), which qualitatively agrees with the indoor and outdoor experimental results. The simulation also showed that the I_{mp} is nearly proportional to irradiance G, and I_{mp}/G is constant within ±1.3 % in the irradiance range between 0.5 and 1.2 kW/m^2, which also agrees with previous experimental studies.

Based on the numerical simulations and experiments, new translation formulas for the temperature and irradiance of V_{mp} and I_{mp}, i.e., Eqs. (4.22) and (4.23), are proposed, wherein the voltage–dependence of TC is explicitly considered. The most important of the additional term is $[1 + \alpha(T_2 - T_1)]$, which is to improve for the precision. The I_{mp} versus V_{mp} curves corrected to 25 °C by the formulas, showed good reproducibility with a standard deviation σ of 0.13 % for many days of data, which confirms the validity of the correction formulas. The P_{max} corrected to STC (P_{max2}/G in Fig. 4.10), which was estimated by using the translation formulas, also showed a good standard deviation σ of 0.24 % in the irradiance range of 1.0 ±0.05 kW/m^2.

The novelty of the current study is that the developed formulas do not require advanced information of TC or diode parameters and no specific software is required. These results are useful for characterizing the performance of commercial crystalline–silicon PV devices by using the I_{mp} and V_{mp} values which are available without breaking the system's MPPT operation.

The present study used a conventional silicon back surface field (BSF) PV module. Nearly the same formulas are expected to be applicable to other types such as passivated emitter and rear contact (PERC), backside contact, and heterojunctions, either without modification or with only slight modification in nE_g/q and α, because the TCs of these modules are well described by the same equation, as described in Hishikawa et al., 2018 [26]. However, precise confirmation is left for further study.

Chapter 5

Detection of shading effect by using I_{mp}, V_{mp}, T_m, and G for crystalline–silicon PV modules

5.1 Introduction

The output power of PV devices is affected by many factors such as the irradiance G, temperature and shading effect, as well as degradation. Detection of the degradation of the PV modules is important, because the degradation reduces the PV module's efficiency. Many techniques have been used to identify PV degradations, such as the visual inspections, current–voltage (I–V) measurements, infrared thermography, and electroluminescence (EL) images [30, 31]. The shading effect is one of the major causes of energy losses of the PV module's output, and it is practically essential for many PV systems since it can be induced by many external factors such as buildings, wires, clouds, trees, weeds, and more. Such effects usually show complex time–dependent feature. The partial shading can lead to hot–spot phenomena and consequently to permanent damage, aging of module, and other severe risks, although the partial shading is caused on a small–area cell. Many previous studies have been published on experiments and simulations of the shading effects [54-61], which were mostly based on the I–V curve data. For example, the model and simulation of the characteristic output of PV systems under shading such as the I–V curves and power–voltage (P–V) curves have been extensively investigated [55, 62-64]. One proposed method to calculate the output for a PV system with several partial shading and mismatch conditions was evaluated by Bai et al., 2015 [55]. It uses the parameter extraction method to obtain five parameters. Then, simulated I–V and P–V characteristics have been compared with experimental results of a PV system. Hemza et al. [63] also compared the measured I–V and P–V characteristics of a PV module with a proposed model acquired given partial shading conditions. They conducted experiments with a crystalline silicon PV module that contains two bypass diodes for each of two PV cell strings, in which 18 cells are series–connected. The normal PV module operation and partial shading condition were tested and compared with mathematical model, in which single–diode model. The I–V curves of the PV module for normal operating both simulation results using the model and outdoor measurement are shown in Fig. 5.1. Then, they performed an experiment with partial shading effect such as three cells with 50 % shading on a single cell–string. The results were compared using I–V curves and P–V curves, as shown in Figs. 5.2 and 5.3, respectively. The shaded cells generated a lower photocurrent than the other non–shaded cells. However, the cell–sting contained a bypass diode, the current of shade–less–string can flow through the bypass diode. The results show that the P–V curves

show two peaks. The existence of shading can usually be detected by the step in the *I–V* curve, as presented in the references [65-66].

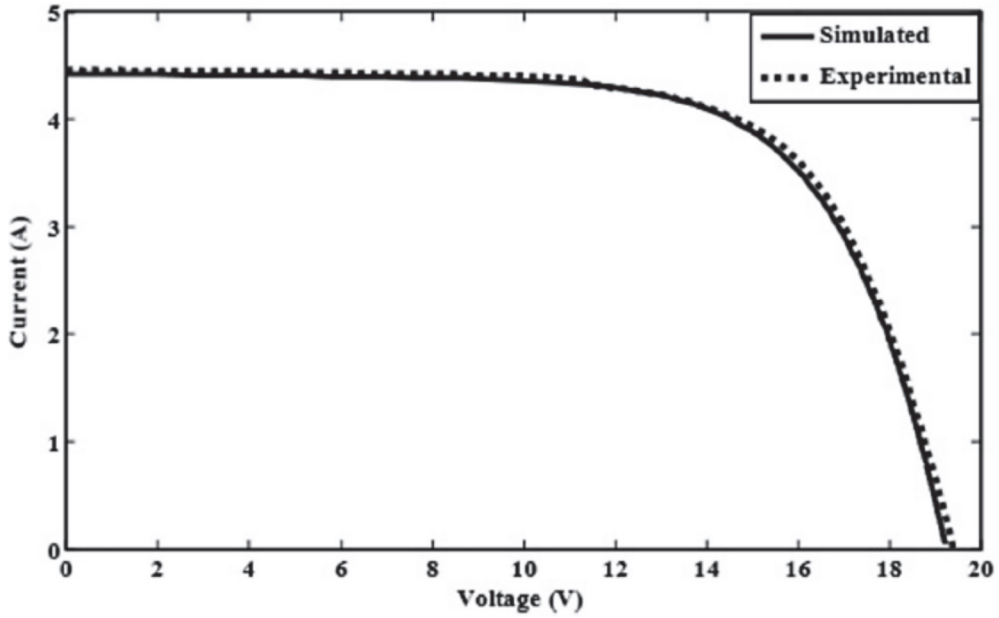

Figure 5.1. *I–V* curves for the module's normal operating: experiment and simulation [63].

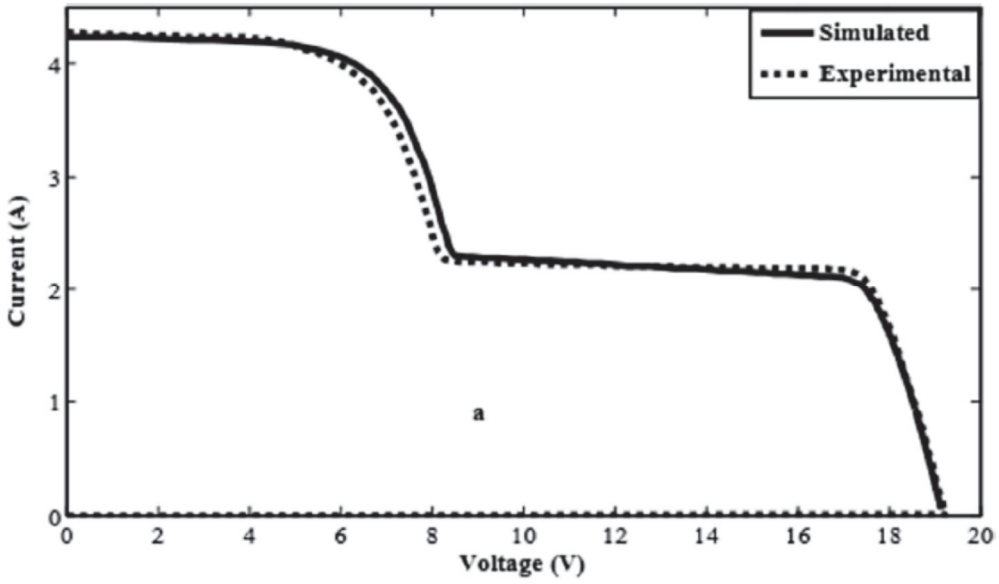

Figure 5.2. *I–V* curves for three cells under 50 % shading condition on one–string–cell: experiment and simulation [63].

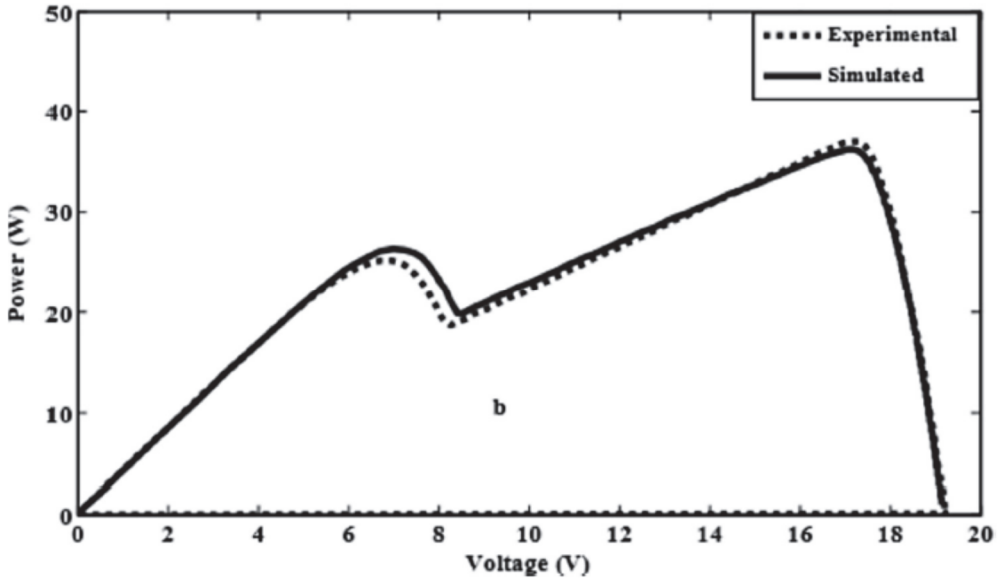

Figure 5.3. *P–V* curves for three cells under 50 % shading conditions on one–string–cell: experiment and simulation [63].

Another study proposed a simulation method with partial shading effect that they proposed a PV mathematical model, which was calculated by using MATLAB [67]. Then, the simulation results were compared with experimental results in the case of partial shading effect performed with a PV module. The module was manufactured by made–to–order which consists of 30 series–connected cells. The partial shading effect was performed with the shading ratio of 1/3 of the cell area for a single cell in the PV module. Then, they changed the shading ratio to 2/3 of the cell area. Finally, full shading on one cell was also tested. The experimental results and the simulation results are shown in Fig 5.4, with comparison for each shading ratio. These results have been observed that the knee points of the *I–V* curves move to higher voltages than in the normal *I–V* curves. However, the shading ratios of the study were performed on one cell that consists of about 33 %, 66 %, and 100 % of the cell area.

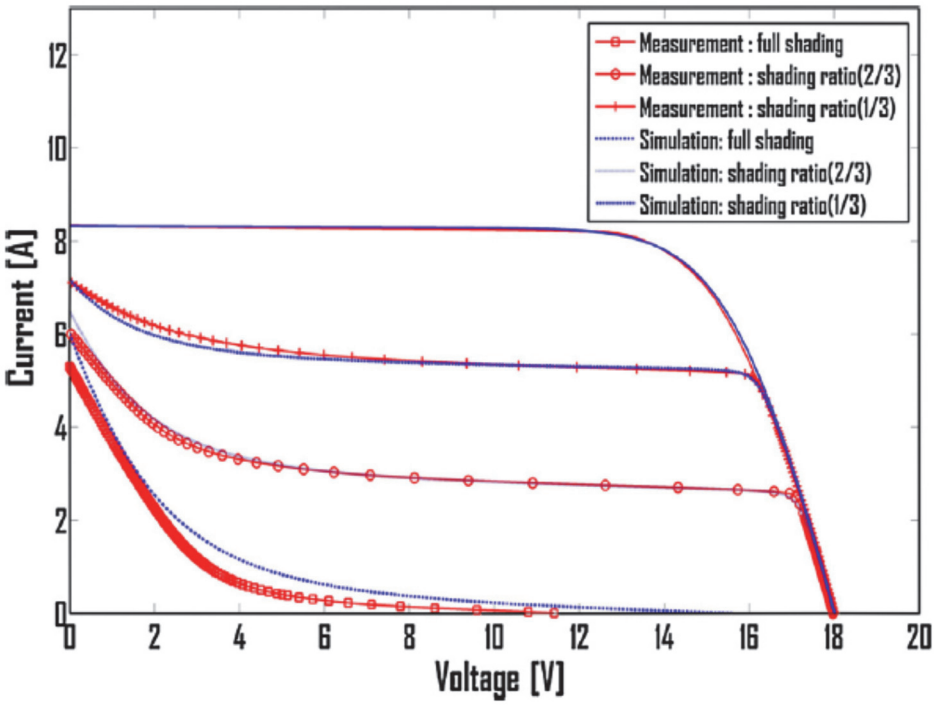

Figure 5.4. *I–V* curves for the module 30 series–connected cells with one cell shading in a module; the shading ratios of the experiment and simulation are shown [67].

Although the approach is based on the *I–V* and *P–V* curves are useful for extracting the performance of PV modules and systems, there is a disadvantage that the *I–V* curve measurement needs to interrupt the system's MPPT operation. Therefore, the ability to detect and investigate the shading effect, without requiring *I–V* curve measurements, is desired, for the purpose of real–time monitoring and precise diagnosis of the long–term performance production of PV modules. It is essential to utilize the information which is available without interrupting the MPPT. This study investigates the detection of the shading effect by using the V_{mp} and I_{mp} under maximum power conditions, which are the measurable electrical parameters during MPPT operation.

The analysis of the V_{mp} and I_{mp} is basically not straightforward, because only one pair of V_{mp} and I_{mp} is obtained at one time. Therefore, the time–series data taken at various irradiances and temperatures should be systematically analyzed. The authors have recently proposed new formulas which can accurately translate the V_{mp} and I_{mp} for temperature and irradiance [68]. This does not require advanced information of temperature coefficient and diode parameters. The significance of only using V_{mp} and

I_{mp} is to simplify analyzed data. This technique is useful to be applied for partial shading detection. In this study, the experimental V_{mp} and I_{mp} are corrected for temperature by the new formulas, which have enabled precise and straightforward analysis of the I_{mp}–V_{mp} curve with the shading effect. The method for detecting the existence of shading is investigated by using experiments and simulation results.

This chapter is organized as follows: (1) The experimental setup for PV module measurement is described. (2) The results and discussions are proposed, which describes the temperature correction of V_{mp} and I_{mp}, that they do not require advanced information of the *I–V* curve parameters. (3) The simulation results have expressed in order to clarify the partial shading effect. Finally, (4) the conclusion is presented.

5.2 Experiment

The outdoor experimental setup consisted of a 36–cell series–connected mono–crystalline–silicon PV module, which has the maximum power of 84 watts on its nameplate (Sharp NT-84L5H), was mounted at the AIST Tsukuba Center, Japan (36°04′N 140°08′E), as shown in Fig. 5.5. The module, which will be hereafter mentioned as the module under test (MUT), was installed on a rack. A PV module irradiance sensor (PVMS), which has an active PV cell and eight dummy cells around it, was used as the irradiance (*G*) sensor. It was mounted by the same azimuth and tilt angle with the MUT on the same rack, hence its angle of incidence of light is also the same as the MUT. It enables accurate measurement of *G* for the PV characterization on both clear sunny days and cloudy days [69]. The irradiance data from one of the three PVMSs was used in this study. The *I–V* curves of the MUT were recorded with a sampling interval of 20 seconds, and were acquired in 0.2 seconds and 100 points per curve. The MUT output measurement was synchronized with the output of PVMS. Although the variation of irradiance is not directly confirmed in the present study, the outdoor irradiance is usually nearly constant within ±0.4 % in 0.2 seconds, according to a recent result [46]. The V_{mp} and I_{mp} were determined from the *I–V* curve in this study. The temperature of the MUT (T_m) was measured at six points on the backsheet, of which the average represents the T_m. Details of the measurements are described in references [45-47]. The examples of measured *G*, I_{mp} (I_{mp1}), and V_{mp} (V_{mp1}) on a clear sunny day are shown in Fig. 5.6. The T_m on the same day is shown by the brown line in Fig. 5.7.

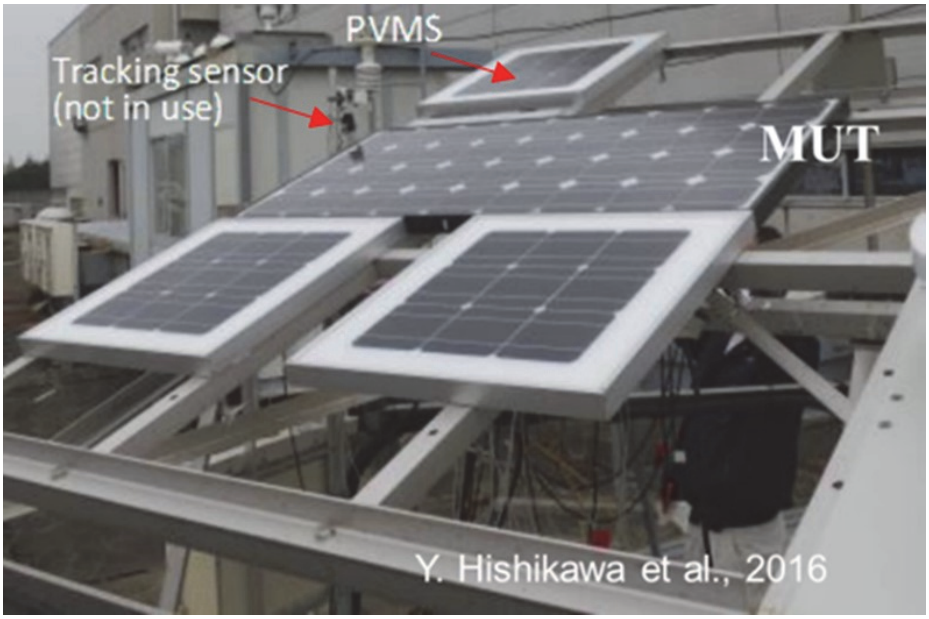

Figure 5.5. Outdoor PV module measurement and PVMS setup used in this study.

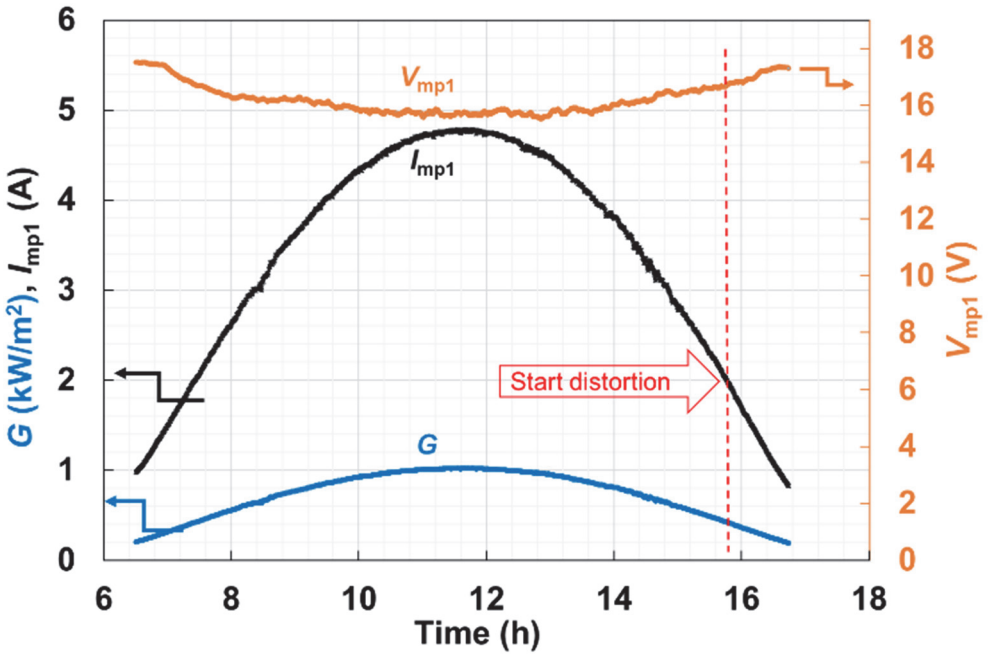

Figure 5.6. Measured I_{mp1}, V_{mp1}, and G on a clear sunny day (May 2, 2015).

5.3 Results and Discussions

5.3.1 Temperature correction of V_{mp} and I_{mp}

The timeline data of V_{mp}, presented by the orange line in Fig. 5.6, are strongly affected by the variation of module temperature T_m within a day, the measured raw data of the I_{mp}–V_{mp} curve has rather complex shape, as shown by the black line in Fig. 5.8. Precise analysis is difficult based on the raw I_{mp}–V_{mp} curve. Therefore, the measured V_{mp} and I_{mp} were corrected to 25 ºC by Eqs. (4.22) and (4.23), which were recently developed (details in Chapter 4) and were demonstrated to be able to precisely translate the V_{mp} and I_{mp} of crystalline–silicon PV module for any desired temperature [68]. An advantage of the equations over the previous proposed ones is that it explicitly considers the voltage–dependent feature of the output voltage of p–n–junction diodes, thereby enabling precise temperature correction in a wide voltage range. Another advantage of the equations is that they do not require advanced information of *I–V* curve parameters or diode parameters. In Eqs. (4.22) and (4.23), the parameters T_1 and T_2 are the measured and target T_m in Kelvin, respectively. V_{mp2} is the value of V_{mp} at T_2. E_g is the bandgap energy of silicon, which is assumed to be 1.12 eV [23, 48, 70]. n is the diode ideality factor, q is the electron charge, N_c is the number of series–connected cells, and α is the TC of I_{sc}. α is estimated to be a typical value of 0.05 %/K [26, 50]. I_{mp2} is the I_{mp} at T_2. The value of nE_g/q is estimated to be 1.232 V, which is known to reproduce the TC of the output voltage for various kinds of crystalline–silicon PV modules [26], and also agrees with the best–fit to the outdoor experimental data of this study. The TC of I_{mp} is known to be very small and typically ranges between -0.0402 %/K and 0.0339 %/K [14, 16, 17, 19, 20, 27]. Therefore, a temperature–independent I_{mp} (Eq. 4.23) is a reasonable assumption.

The I_{mp}–V_{mp} curve, corrected to 25 °C by using Eqs. (4.22) and (4.23), is shown by the red line in Fig. 5.8. It has a smoother shape than the measured curve, since the small variation of V_{mp} due to the fluctuation of T_1 is smoothed by the temperature correction. A more important feature of the corrected curve is that it exhibits two branches for I_{mp} lower than 2 A, which are indicated as A and B in the figure. The branch B exhibits a higher V_{mp2} than the branch A at the same I_{mp2}. The branch B corresponds to the time after 3:30 pm. It is noted that the existence of two branches is difficult to be detected in the experimental timeline data (Fig. 5.6) or the uncorrected I_{mp}–V_{mp} data (Fig. 5.8, black line). The corrected V_{mp} for temperature by using the previous *I–V* translation Eq. (4.8) is compared in the Figs. 5.8, 5.10, 5.12, and 5.14 (gray line). Furthermore, the I_{mp}–V_{mp} points at STC are also shown in the green diamond in the figures. This agrees well with the I_{mp}–V_{mp} curve corrected using the developed formulas for both clear sunny days and a partially sunny day. In case of overcast cloudy day in Fig. 5.12, there are no I_{mp} and V_{mp} data at G around 1 kW/m^2 but the results show good reproducibility using the developed formula.

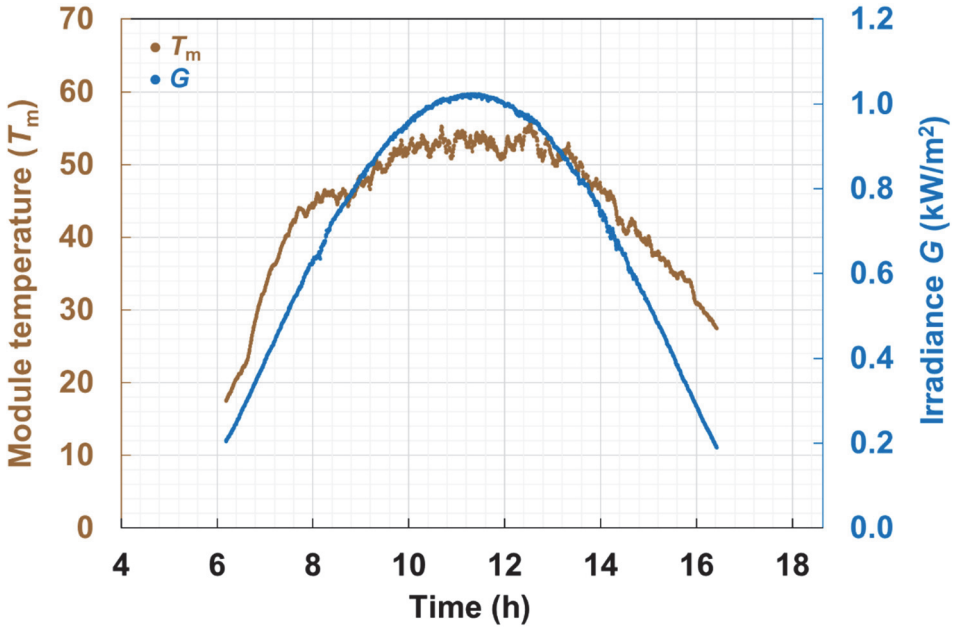

Figure 5.7. Measured T_m and G on a clear sunny day (May 2, 2015).

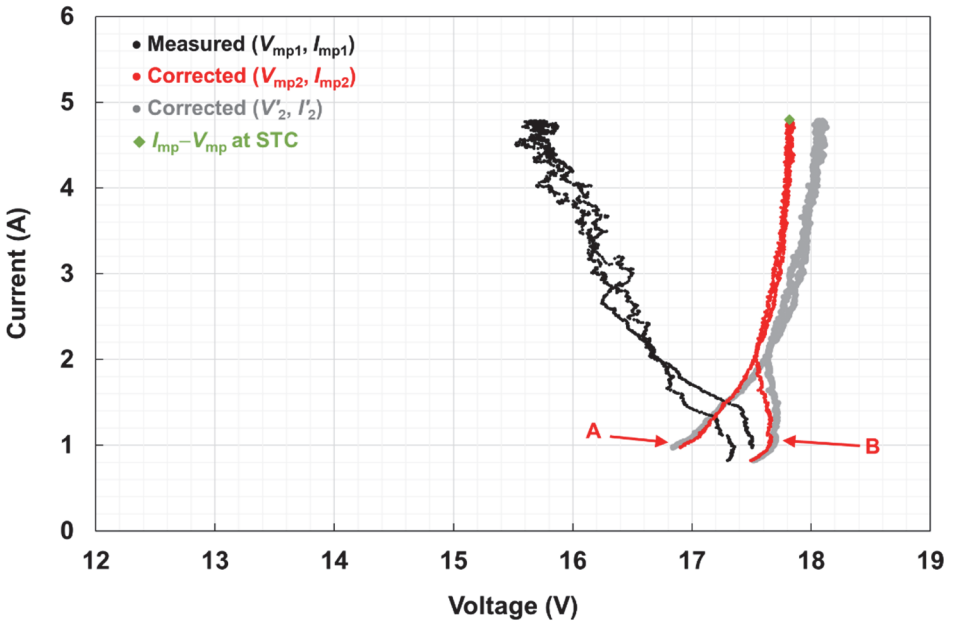

Figure 5.8. The black line (V_{mp1}, I_{mp1}) shows the measured I_{mp}–V_{mp} curve on the same day presented in Fig 5.7. The red line (V_{mp2}, I_{mp2}) shows the curve corrected to 25 ºC by Eqs. (4.22) and (4.23). The gray line is the V'_2 corrected by the previous I–V curve translation Eq. (4.8). Data for the I_{mp}–V_{mp} point at STC is shown in the green diamond.

Equations (4.22) and (4.23) are also applicable to various kinds of weather, even when the irradiance is unstable; this is because the irradiance is measured by the PVMS. It is noted that the irradiance measurement by PVMS can suppress the measurement error related to the variation of spectrum, incident angle, and unstable irradiance, thanks to its nearly the same spectral, angular, and fast temporal responses as the MUT [69]. Figure 5.9 shows the T_m and G for a partially sunny day when the irradiance is unstable (May 17, 2015). Figure 5.10 shows the I_{mp}–V_{mp} curves on the same day before (black symbols) and after (red symbols) correction to 25 °C using Eqs. (4.22) and (4.23). The corrected curve does not show apparent branches, although there is slight increase in V_{mp2} in some of the data in $I_{mp} < 2$ A. An extreme case is shown in Figs. 5.11 and 5.12, when the weather is overcast cloudy and occasional rainy (May 19, 2015); here, no branches are available in the corrected curve (red symbols) is appreciable. Figs. 5.13 and 5.14 are the data on another clear sunny day (April 27, 2015), which Fig. 5.14 also features two branches (red symbols). The branch A of Figs. 5.8 and 5.14 agrees with the results on a partially sunny day and overcast cloudy day. The V_{mp} in $I_{mp} < 2$ A is high on branch B of Fig. 5.8 and Fig. 5.14, moderate on the partially sunny day (Fig. 5.10), and low on the overcast cloudy day (Fig. 5.12). Figure 5.15 summarizes the corrected curves under different weather conditions. Considering that the data are taken within one month, and the intrinsic performance of the MUT is expected to be constant within the period, these results suggest that the difference in the corrected I_{mp}–V_{mp} curves is caused by other factors or failures such as cell crack, hotspot, and shading effect. The shading effect is one possible origin because it is time–dependent, reproducible, and not permanent degradation. Further detail is investigated by using numerical simulations of the shading effect, as described in the next section.

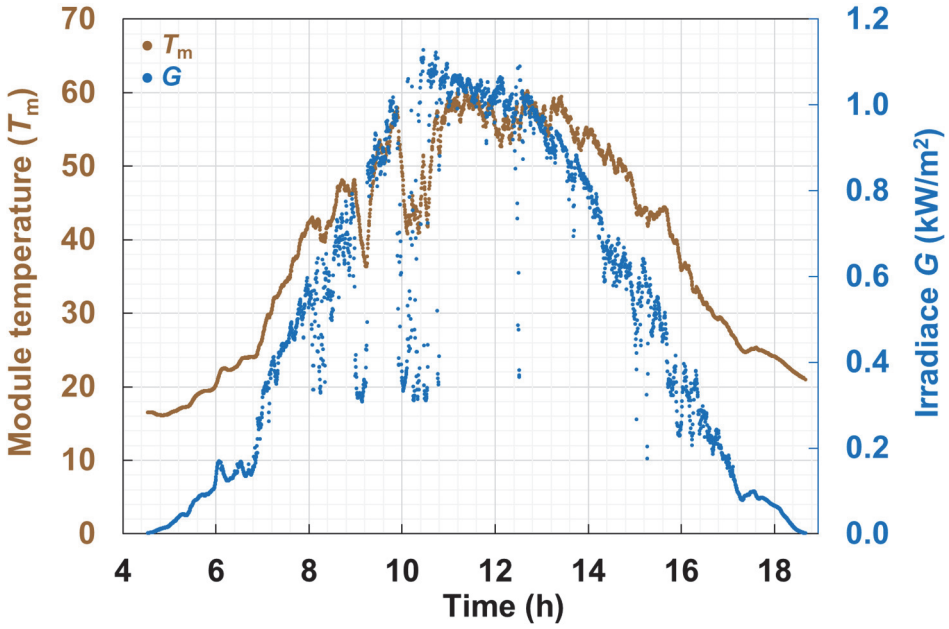

Figure 5.9. Measured T_m and G on a partially sunny day when the irradiance is unstable (May 17, 2015).

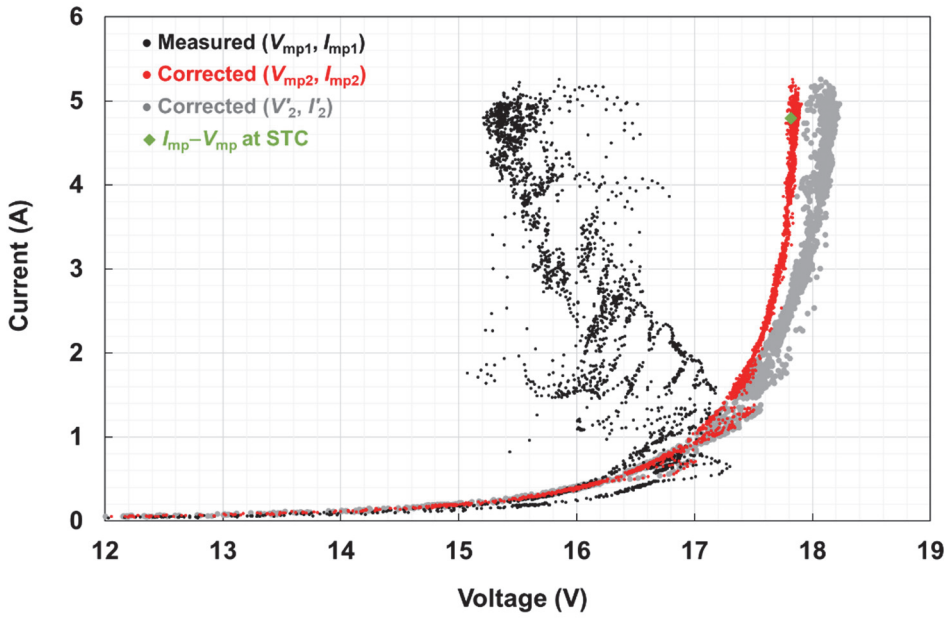

Figure 5.10. The black line (V_{mp1}, I_{mp1}) shows the measured I_{mp}–V_{mp} curve on the same day as Fig. 5.9. The red line (V_{mp2}, I_{mp2}) shows the curve corrected to 25 ºC by Eqs. (4.22) and (4.23). The gray line is the V'_2 corrected by the previous I–V curve translation Eq. (4.8). Data for the I_{mp}–V_{mp} point at STC is shown in the green diamond.

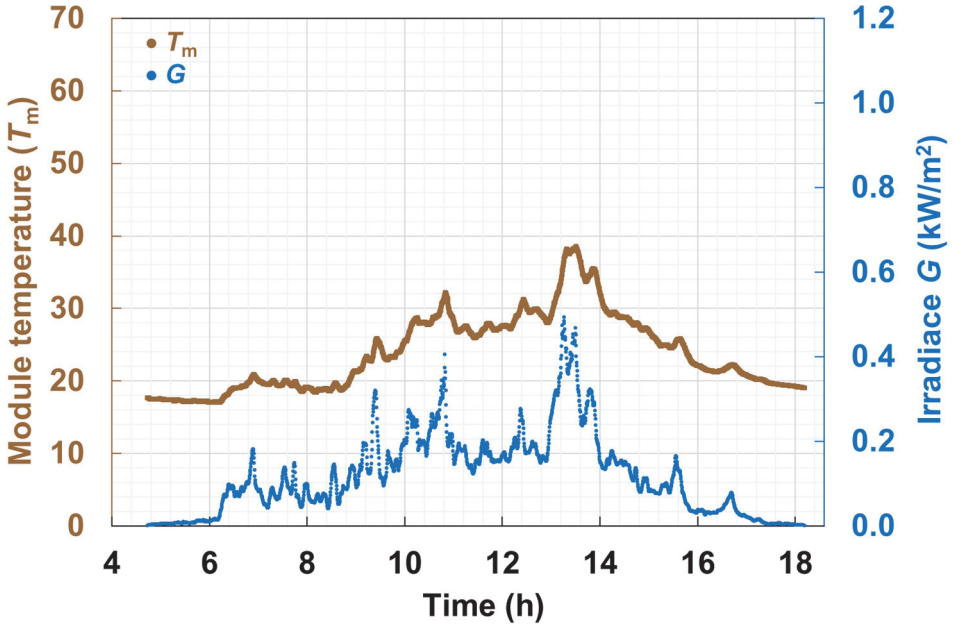

Figure 5.11. Measured T_m and G values on an overcast cloudy day (May 19, 2015).

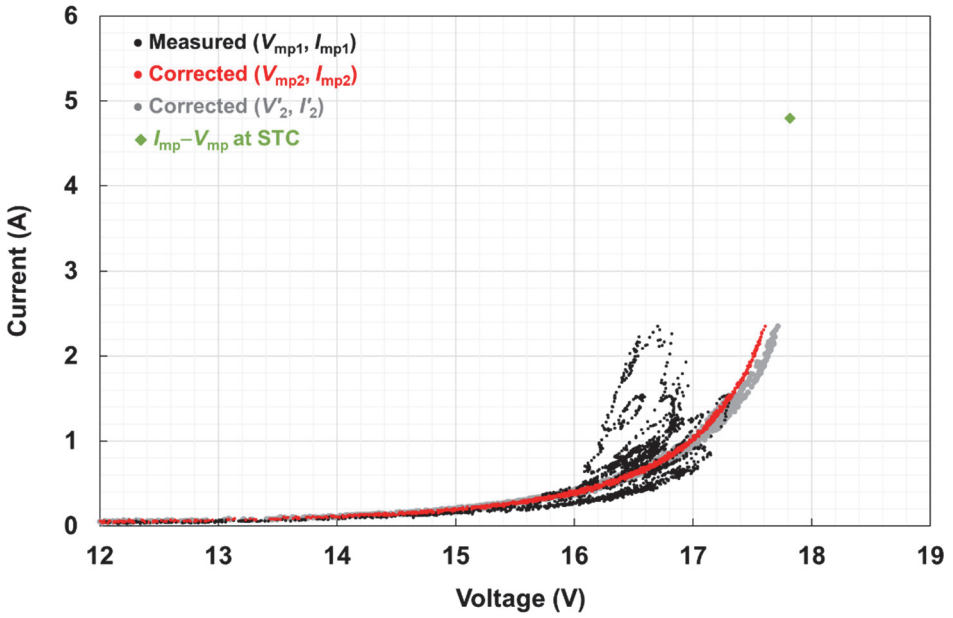

Figure 5.12. The black line (V_{mp1}, I_{mp1}) shows the measured I_{mp}–V_{mp} curve on the same day as Fig. 5.11. The red line (V_{mp2}, I_{mp2}) shows the curve corrected to 25 ºC by Eqs. (4.22) and (4.23). The gray line is the V'_2 corrected by the previous I–V curve translation Eq. (4.8). Data for the I_{mp}–V_{mp} point at STC is shown in the green diamond.

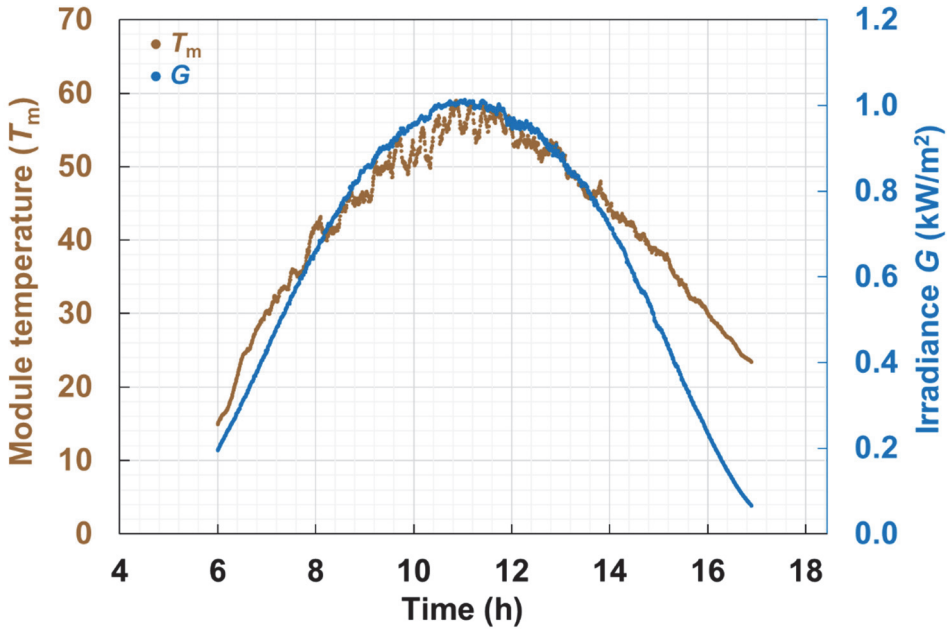

Figure 5.13. Measured T_m and G values for another clear sunny day (April 27, 2015).

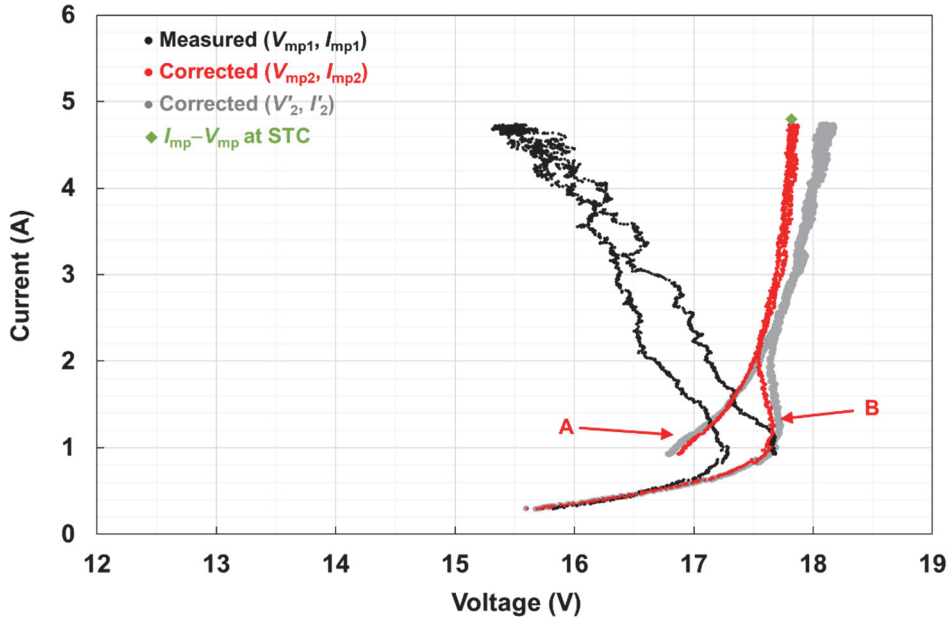

Figure 5.14. The black line (V_{mp1}, I_{mp1}) shows the measured I_{mp}-V_{mp} curve on the same day as Fig. 5.13. The red line (V_{mp2}, I_{mp2}) shows the curve corrected to 25 ºC by Eqs. (4.22) and (4.23). The gray line is the V'_2 corrected by the previous I–V curve translation Eq. (4.8). Data for the I_{mp}–V_{mp} point at STC is shown in the green diamond.

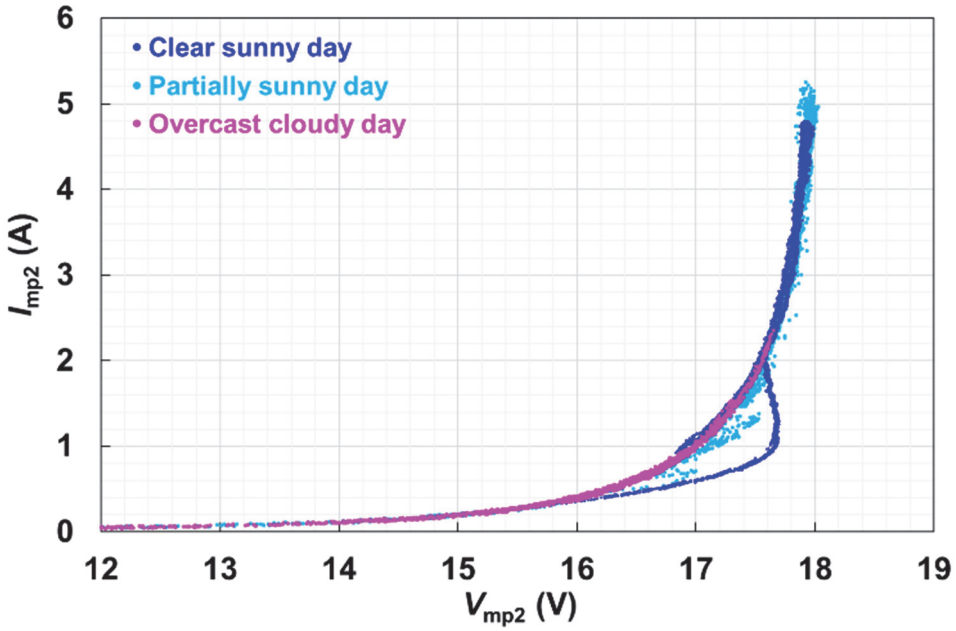

Figure 5.15. Comparison of the I_{mp}–V_{mp} curves after correction to 25 °C on a clear sunny day (blue), a partially sunny day (light blue), and an overcast cloudy day (pink).

5.3.2 Simulation of the partial shading effect

The results of the previous section suggest that the increase in V_{mp} in the corrected I_{mp}–V_{mp} curve is related to the shading effect. The present section uses numerical simulations in order to validate and interpret the shading effect. The *I*–*V* curve of a shaded module is simulated by the series connection of the component cells having different values of photocurrent. The *I*–*V* curve of each cell is represented by Eq. (5.1) [71]. The series connection is expressed by summing up the voltage of each cell at the same current. The basic approach of the simulation is similar to those of previous studies [57, 66, 67]. The new feature in this study is that it focuses on the impact of the partial shade on the mutual relation of the I_{mp} and V_{mp}, or the I_{mp}–V_{mp} curve.

$$I = I_{ph} - I_0\left[\exp^{\left(\frac{q(V+IR_S)}{N_C nkT}\right)} - 1\right] - \frac{V+IR_S}{R_{sh}}\left[1 + a\left(1 - \frac{V+IR_S}{V_{br}}\right)^{-m}\right]. \quad (5.1)$$

Here, I_{ph} is the photocurrent, I_0 is the diode reverse saturation current, q is the electron charge, V is the output voltage, R_s is the series resistance, N_c is the number of series–connected cells in the module, n is the diode ideality factor, k is the Boltzmann's constant, T is the device temperature in Kelvin, and R_{sh} is the shunt resistance, a is the fraction of ohmic current involved in avalanche breakdown, m is the avalanche breakdown exponent, and V_{br} is the junction breakdown voltage. The V_{br} is known to range between -12 V and -30 V for monocrystalline silicon cells [65]. In this section, the simulations are carried out by assuming I_{ph} = 5.262 A (under 1 kW/m^2, 25 °C), $I_0 = 5.50 \times 10^{-9}$ A, R_s = 0.0054 Ω/cell, n = 1.147, R_{sh} = 4.5 Ω/cell, V_{br} = -15 V, T = 25 °C, a = 0.1, and m = 4, unless otherwise specified, which were determined to fit the experimental data. The numerical simulation was carried out on a PV module with 36 cells in series, which has a bypass diode for every 18 cells. The bypass diodes function to protect the string cell reverse bias voltage. It conducts when the reverse bias voltage is larger than its threshold value (0.7 V for silicon). The structure assumed in the simulation is identical to the experimental module as mentioned in section 5.3.1.

Typical simulation results are shown in Fig. 5.16. The I_{ph} of each component cell was determined by considering the uniform shade, as indicated by the brown area in the figure. The irradiance in the shade was assumed to be 0.5 kW/m^2 rather than the typical diffused irradiance of 0.2 kW/m^2, in order to better simulate the situations of slight partial shading by small objects near the modules, wires, and distant objects, which are also often seen in PV systems. The irradiance outside of the shade was assumed to be 1 kW/m^2. Therefore, the I_{ph} of each cell is expressed as the following equation,

$$I_{\mathrm{ph}} = 5.262(1 - x_{\mathrm{c}}) + 2.631x_{\mathrm{c}}. \tag{5.2}$$

Here, the I_{ph} under G =1 kW/m^2, and T = 25 °C, is equal to 5.262 A. The x_c is the ratio of the shaded area in each cell. The relative shaded area in the module x_m was varied from 0 % to 100 %. The I_{ph} of each cell was determined by Eq. (5.2) for each x_m. The resultant I–V curves of the modules are shown in Fig 5.16. The points of (V_{mp}, I_{mp}) corresponding to the I–V curves are shown by red circles. The I_{mp}–V_{mp} curve without shading, or the relation of the I_{mp} and V_{mp} for various irradiance levels without shading, is also shown by the green dashed line in the figure. The simulation results show that the V_{mp} values of the red circles are larger than that of the green dashed curve. These results indicate that the V_{mp} of a shaded module is larger than that without shading, which agree with previous studies [72-74]. Saint-Drenan and Barbier simulated the partial shading effect on array with and without bypass diodes. The effect of bypass diodes on I–V curve is clearly observable. The influence of bypass diodes on the

relationship between maximum power points and shaded fraction, especially for shaded fraction under 50%, is much less marked which shipped to other knee points. A simulation effect of partial shading on the maximum power points of a PV module without bypass diodes was also given higher voltage while the current was set by the shaded cell, which therefore limits the whole module [74]. In this study, a similar increase in the V_{mp} is observed by the simulation for horizontal shading pattern with a module with two bypass diodes, as shown in Fig. 5.17. For the diagonal shading pattern, as shown in Fig. 5.18, the points of (V_{mp}, I_{mp}) show complex trajectory. However, the increase in V_{mp} is observed at least for a certain range of x_c from 20 % to 70 %. An example of the variation of the V_{mp} and I_{mp} by the shading is shown in Fig. 5.19, where one cell in the PV module is shaded; the x_c is equal to 20 %. The V_{mp} and I_{mp} of the shaded cell(s) decrease. However, the V_{mp} of other unshaded cells in the PV module increases, because the I_{mp} of the whole module decreases (ΔI_{mp}), due to the requirement of current continuity of the series–connected cells. As a result, the sum of the V_{mp} of the shaded cell(s) and unshaded cells in the module increases (ΔV_{mp}).

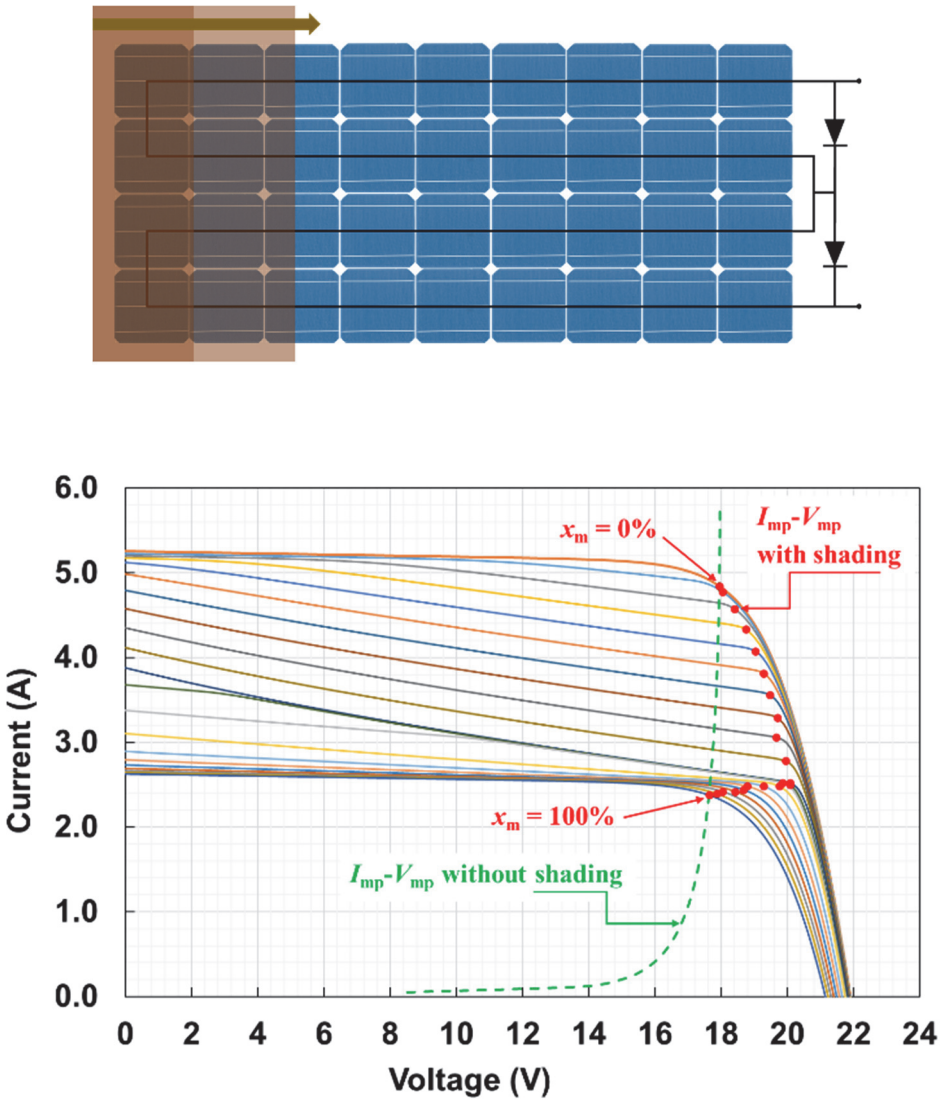

Figure 5.16. Simulation results of the effects of vertical shade pattern on the I–V curve, V_{mp} and I_{mp} at various shading ratios x_c and x_m. The shade is illustrated by the brown area. The curves in the range of x_m = 0 % to 100 % are shown. The points of (V_{mp}, I_{mp}) are shown by red circles. The I_{mp}–V_{mp} curve without the shading effects is also shown by the dashed green lines.

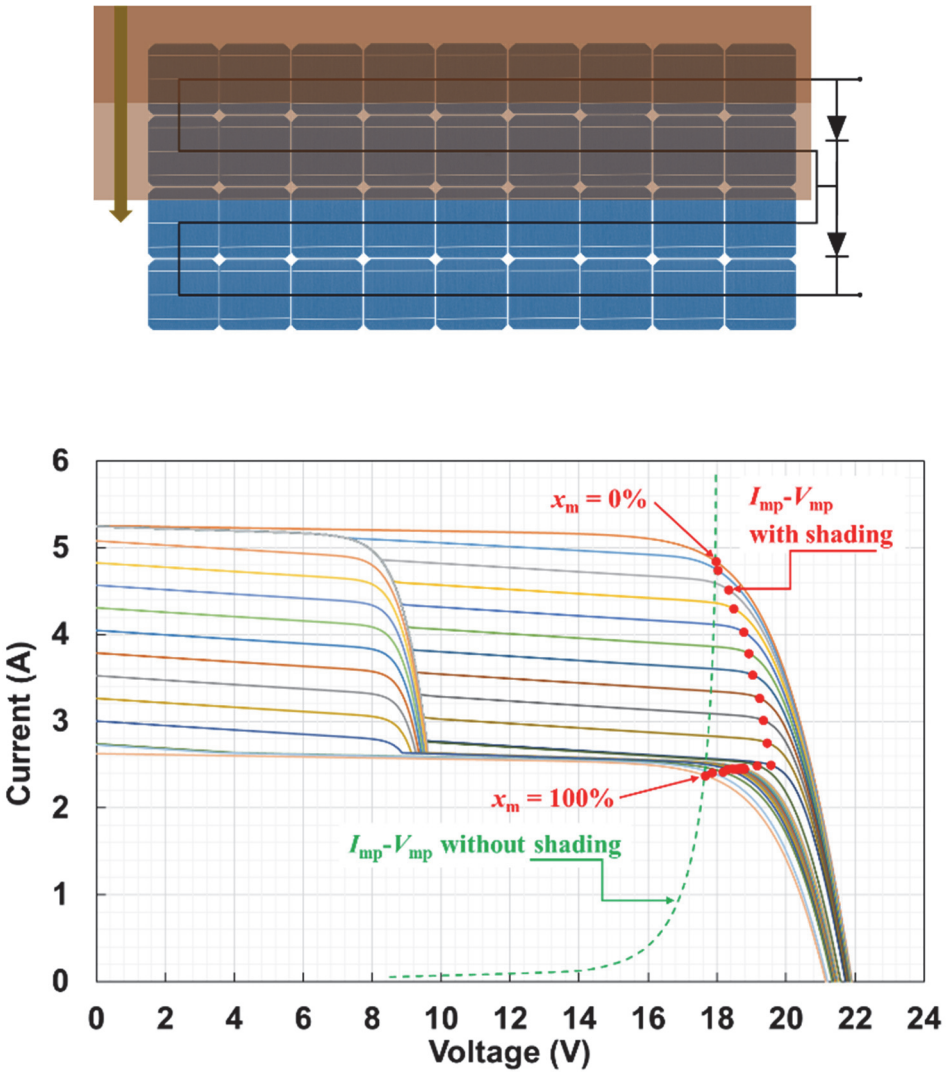

Figure 5.17. Simulation results of the effect of horizontal shading pattern on the *I*–*V* curve, V_{mp} and I_{mp} at various shading ratio x_c and x_m. The shade is illustrated by the brown area. The curves in the range of x_m = 0 % to 100 % are shown. The points of (V_{mp}, I_{mp}) are shown by red circles. The I_{mp}–V_{mp} curve without the shading effect is also shown by the dashed green lines.

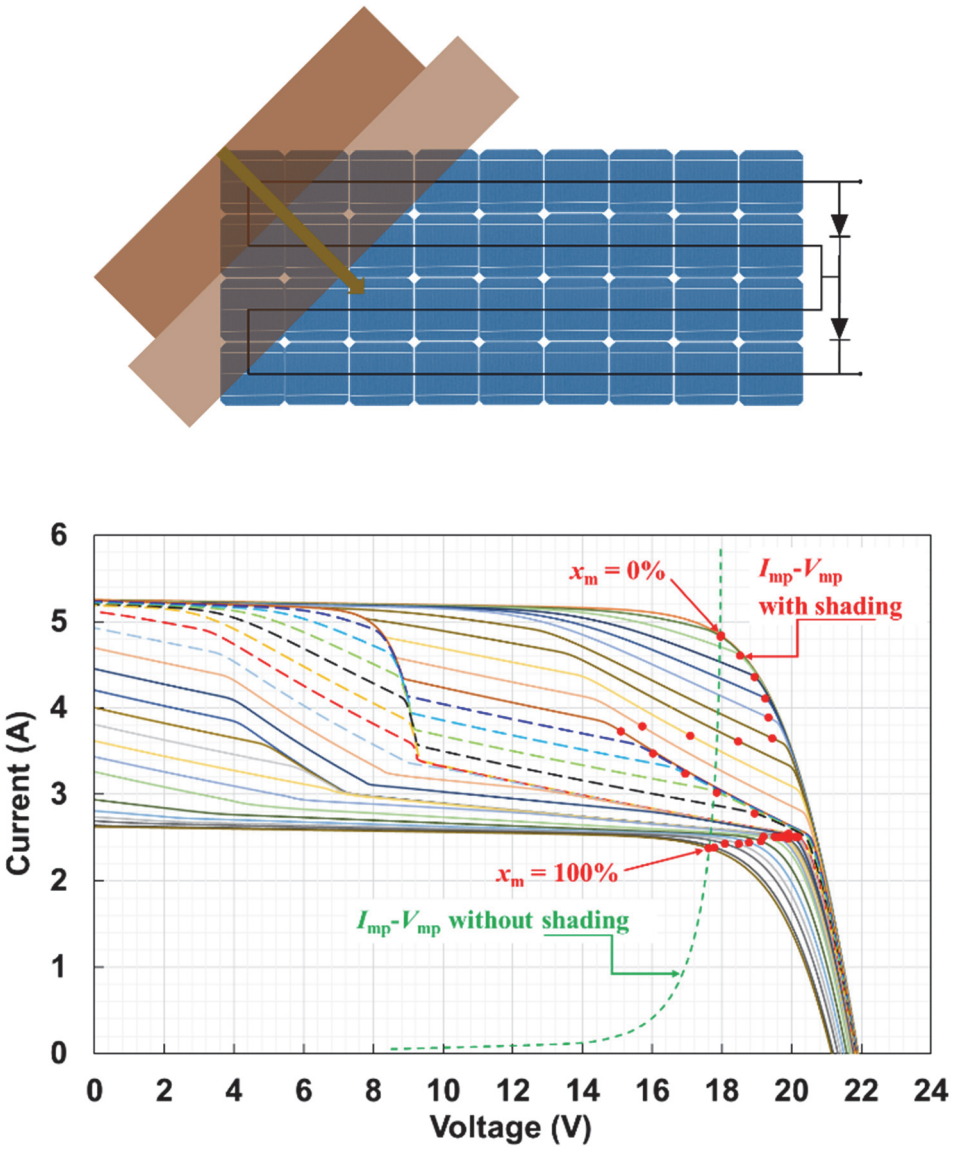

Figure 5.18. Simulation results of the effect of diagonal shading pattern on the *I–V* curve, V_{mp} and I_{mp} at various shading ratio x_c and x_m. The shade is illustrated by the brown area. The curves in the range of x_m = 0 % to 100 % are shown. The points of (V_{mp}, I_{mp}) are shown by red circles. The I_{mp}–V_{mp} curve without the shading effect is also shown by the dashed green lines.

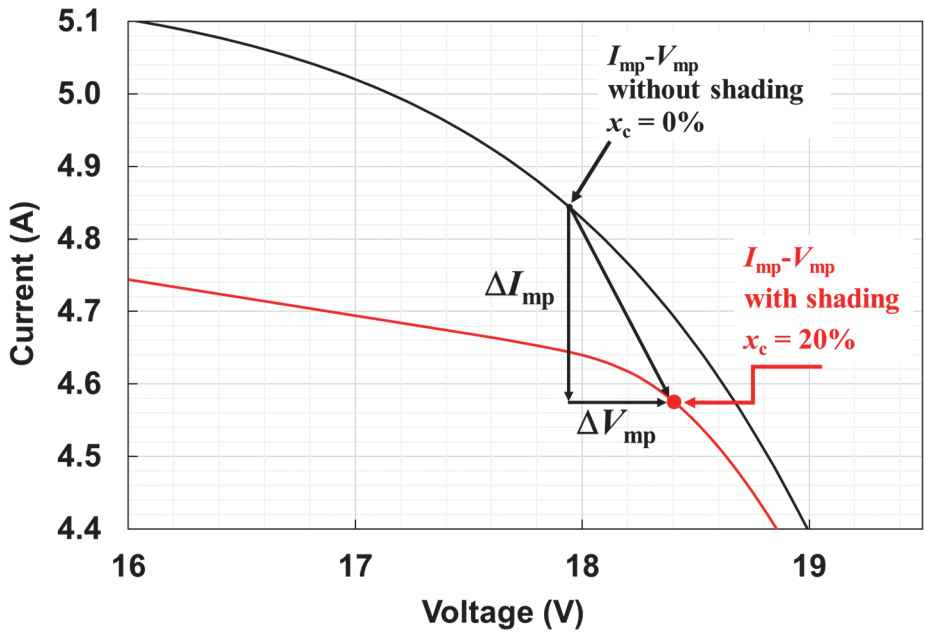

Figure 5.19. An illustration of the variation of the V_{mp} and I_{mp} by the shading. The I–V curves with and without shading are shown by the red and black curves, respectively. The corresponding I_{mp} and V_{mp} are indicated at x_c = 0 % and x_c = 20 %, respectively.

The simulation results above indicate that the shading effect usually leads to increase in the V_{mp} at least in a certain range of x_m. Therefore, it is probable that the appearance of branch B with high V_{mp2} in Fig. 5.8 is caused by the shading effect. In this study, the probable origin of shade after about 3:30 pm is the direct irradiance sensor, which was not used in the present study but was built–in on the rack (Fig. 5.5). Because the top of the sensor is above the surface of the MUT, it probably casts a shadow over the MUT when the solar elevation is low, as shown in Fig. 5.20. Because both the shading ratio and irradiance change in the outdoor environment, the simulation was carried out by varying both of them by using the model shown in Fig. 5.20. One cell in the module was assumed to be shaded, because the shade in other cells is expected to be much smaller than the nearest cell. The irradiance and the ratio of the shaded area in the cell x_c as listed in Table 5.1, were determined by the best–fit to the experimental data. The parameters were assumed to be constant under different irradiances except for the R_{sh}, which is known to show irradiance dependence [75, 76]. In this study, it was assumed to be proportional to $G^{0.9}$ [75]. The photocurrent of each cell was determined as follows:

$$I_{\mathrm{ph}} = G \times 5.262, \tag{5.3}$$

$$I_{\mathrm{ph}} = G \times 5.262(1 - x_{\mathrm{c}}). \tag{5.4}$$

Equations (5.3) and (5.4) express the I_{ph} of cells without and with shading, respectively. The results of the simulation, as shown in Fig. 5.21, indicate that the branch B is well reproduced by the parameter set of Table 5.1. They also suggest that the increase in V_{mp} compared to that without shading is a good indication of the shading effect. It is noted, however, that the x_{c} cannot be uniquely determined from the experiments and simulations at the present stage, since the V_{mp} is dependent not only on the x_{c} but also on other parameters such as the R_{s} and R_{sh}.

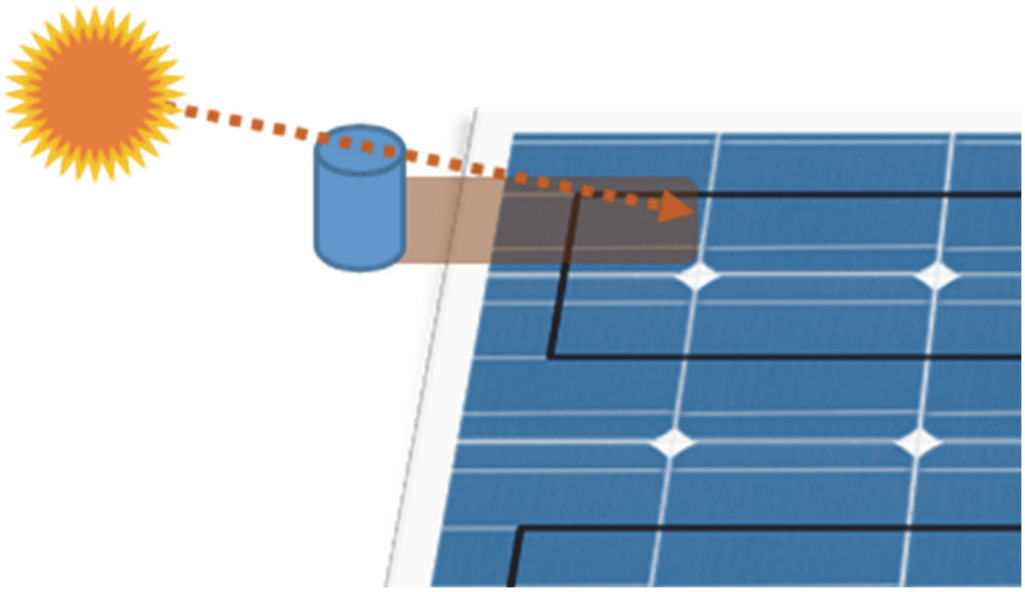

Figure 5.20. Model for simulating the experimental results of Fig. 5.7(b) and Fig. 5.14. The shaded area is shown in brown color.

Table 5.1

Parameters used for the simulation

Time (hh:mm)	Irradiance G without shading (W/m^2)	x_c (%)
15:54	390	5.5
16:00	370	6.9
16:10	330	8.1
16:20	290	9.5
16:30	250	10.5
16:40	210	11.8
16:50	170	12.0
17:00	140	10.7
17:05	120	9.7
17:12	100	8.2
17:16	90	6.2
17:20	80	4.1

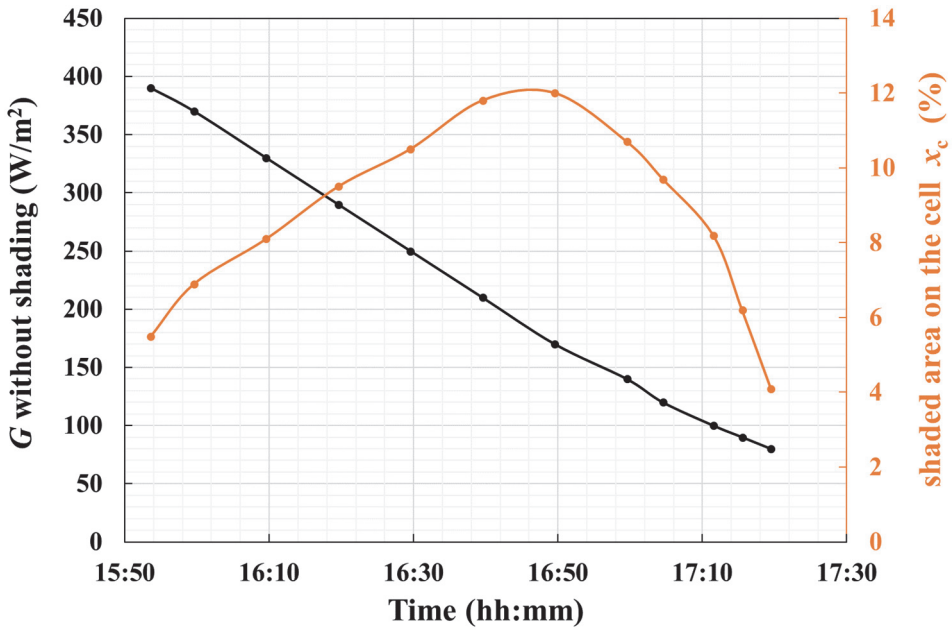

Figure 5.21. Parameters used for the simulation between 15:54 and 17:20, The value of G without shading and the percentage of the shaded area on the cell, are shown on the left and right axes, respectively.

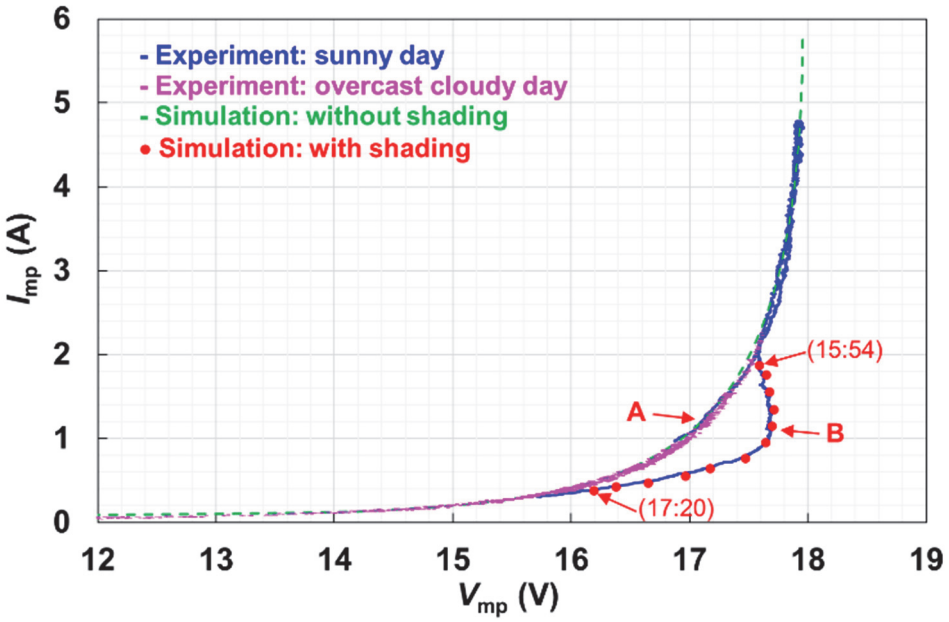

Figure 5.22. Comparison between the experimental results of Fig. 5.15 and the simulation results, based on Table 5.1. The simulation results are shown by red circles.

The present section has clarified that the shading effect can be detected by using the I_{mp}–V_{mp} curve, which is corrected for temperature with Eqs. (4.22) and (4.23). The simulation results as presented in Fig. 5.22, suggest that a slight shade of about 5 – 10 % on a single cell in the module can be detected as the increase in V_{mp} at about 0.7 V, which corresponds to about 4 % of the V_{mp}, compared at the same I_{mp}. The temperature correction is essential, since the V_{mp} usually changes by about 10 % in a day due to the variation of T_m. Therefore, the increase in V_{mp} is difficult to be recognized by the raw time–series data of V_{mp} (as presented in Fig. 5.6) or the I_{mp}–V_{mp} curve before the temperature correction (black line in Fig. 5.8). The shading effect is pronounced on clear sunny days, and is nearly negligible on overcast cloudy days, as demonstrated in Fig. 5.15. Therefore, data on clear sunny days are useful for detecting the shading effect, and data on overcast cloudy days are also important for experimentally defining the reference I_{mp}–V_{mp} curve without shade. The results are also applicable to PV systems which have many modules in series, as long as the shading effect on the I_{mp}–V_{mp} curve is distinguishable. Although the experimental V_{mp} and I_{mp} in this study were determined from the I–V curves, the present method can be used for the continuous monitoring data of V_{mp} and I_{mp} during the MPPT operation without the I–V curve measurements, since the present method uses only the V_{mp}, I_{mp}, G and T_m.

5.4 Chapter Summary

This work investigated a method to detect partial shade on a PV module during the MPPT operation from the experimental V_{mp} and I_{mp}, which are the measurable electrical parameters during MPPT without interrupting the operation. The experimental V_{mp} and I_{mp} were corrected for temperature were done in this study by using a new formula which recently developed [68], in order to reduce the scatter in V_{mp} due to variation of temperature. The experiments and numerical simulations indicate that the corrected experimental I_{mp}–V_{mp} curve shows a clear increase in V_{mp}, if it is affected by the partial shade. The shape of the shaded I_{mp}–V_{mp} curve matches the results with the results of numerical simulations, including the series connection of shaded and unshaded cells. The simulation results of vertical and horizontal partial shading show similar increase in V_{mp}, which indicate that the increase in the V_{mp} is due to the non–uniformity of the photocurrent of the cells. Although the shape of the I_{mp}–V_{mp} curve may be complex when the shading non–uniformity extends to multiple strings by diagonal shade, the increase in V_{mp} is still observed in some ranges of shading ratio. Therefore, the existence of partial shade can be detected by the shift of the I_{mp}–V_{mp} curve toward higher voltage. The result of this study can be used to identify shading effects without I–V curve measurements. It is expected to identify slight shading effect such as x_c = 5 – 10 %, which is difficult to be detected by the raw V_{mp} and I_{mp} data. The present method uses only the V_{mp}, I_{mp}, G, and T_m, and can be used with various kinds of crystalline–silicon PV modules, without advance knowledge of module–specific parameters such as the temperature coefficient. Therefore, the method is expected to be helpful for identifying the partial shading by using the continuous monitoring data of PV systems, and separating the shading effect from other factors such as module degradation and breakage. The present study has clarified the basic approach for characterizing the module performance by using the V_{mp} and I_{mp} from the experiments and simulation results. The application of the present approach to various kinds of situations is an important target for future study, such as identifying the artificial and environmental shading, cell crack, increase in R_s, and PID.

Chapter 6

Detection of cell cracks, increased R_s, and PID degradation of crystalline–silicon PV module by using the I_{mp}, V_{mp}, and T_m

6.1 Introduction

The PV modules and systems operate under various environmental conditions such as temperature, irradiance, and the surrounding environment. Some defects, such as cell cracks and an increase in series resistance (R_s), are caused by mechanical stresses, or solder bond failure, and can affect the reliability of the PV modules and systems. One further degradation is potential–induced degradation (PID) caused by voltage stress. Today, typical system voltage ranges of 700 – 1000 V [32], and the IEC Standard (IEC 61730-1, 2016) has limited the maximum direct–current system voltage of 1500 V [77]. This deterioration would reduce energy production, in some cases resulted in up to 14% drop in performance of modules affected by PID [32]; furthermore, it imposes severe risks on the PV modules and systems over time [33, 34].

Previous studies have proposed several techniques, such as the electroluminescence (EL) [33-35] and *I–V* curve measurement [36], to investigate cell cracks. An investigation of PID using *I–V* curves and EL measurement techniques, was proposed [32, 37]. Although the *I–V* curves or power–voltage (*P–V*) curves are useful for assessing the failure of the PV modules and systems, there is a significant disadvantage as well; the measurements need to interrupt the MPPT operation of the system, and they require additional test equipment, i.e., the *I–V* tester [78, 79] and EL camera [32, 37]. In order to solve the problem, the present study measures the V_{mp} and I_{mp} which are practically the only electrical parameters that can be measured without interrupting the MPPT operation. The present study also firstly utilizes the temperature–corrected I_{mp}–V_{mp} curves instead of the *I–V* curve in order to analyze degradations. Conventionally, the analysis of the V_{mp} is not straightforward, because it significantly fluctuates [28] owing to the variation in module temperature (T_m) and irradiance. Therefore, this chapter has utilized the new formulas that can accurately translate the V_{mp} and I_{mp} for temperature and irradiance, which were recently proposed in [68].

In this study, the effects of degradation, such as, a cell crack, an increase in R_s, and a PID, were investigated by numerical simulations to determine the basic method for detecting degradation by using the I_{mp}–V_{mp} curve. A cell crack on one cell in the module was performed as an inactive area, as shown

in Fig. 6.1. Then, the simulation was performed, as shown in Fig. 6.2, which compared two levels of cell crack. The results illustrated that the V_{mp} is shifted to higher voltage compared with the normal I_{mp}–V_{mp} curve (red line), as shown in the blue dots. However, the power of the module is reduced because the output current of the cracked cells is reduced.

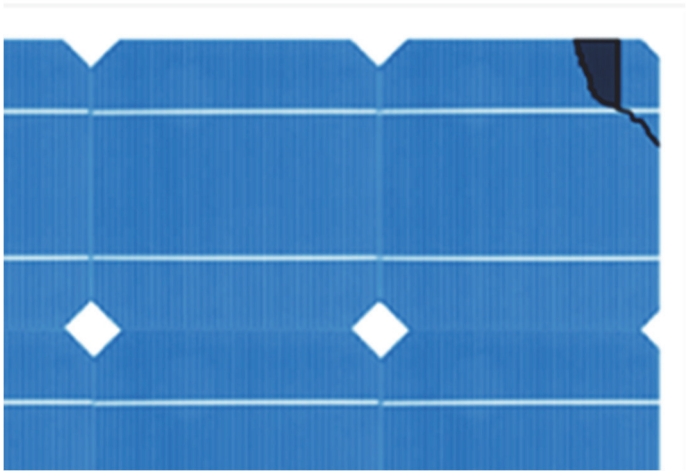

Figure 6.1. Illustration of the inactive area produced by cell cracking.

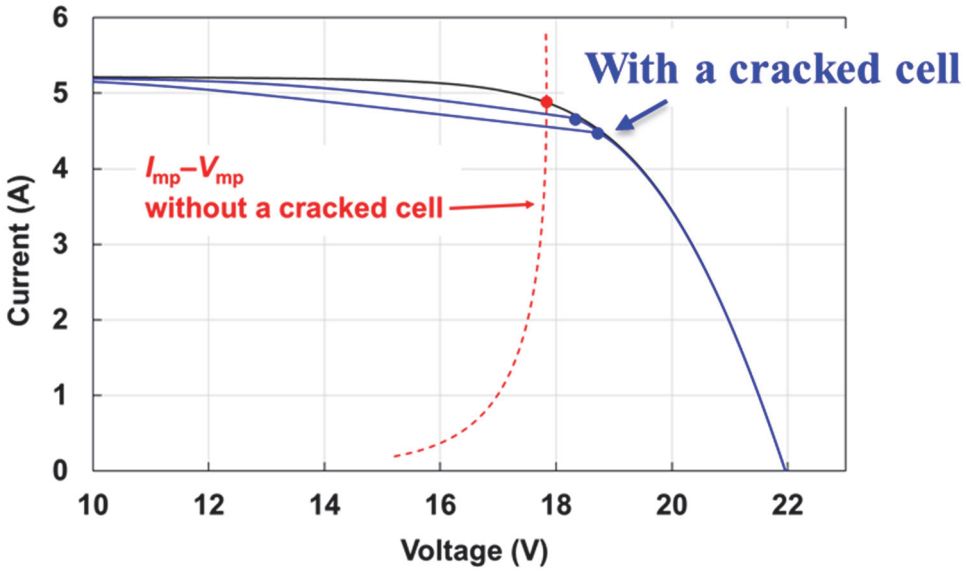

Figure 6.2. Effects of cell crack upon *I*–*V* curve and appearance to higher voltage.

The series resistance can severely affect the PV performance according to the voltage drop. The series resistance has a generally distributed nature, such as emitter sheet resistance, contact resistance, and contact of the front and rear metallization contact. The impact of R_s is to reduce the fill factor and may also reduce the short–circuit current. The R_s is basically shown in series–connect as shown in Fig. 6.3 for a one–diode model equivalent circuit of the solar cell. The effect of an increased in R_s on the *I–V* curve is shown in Fig. 6.4, which reduces the maximum power, fill factor, and V_{mp}.

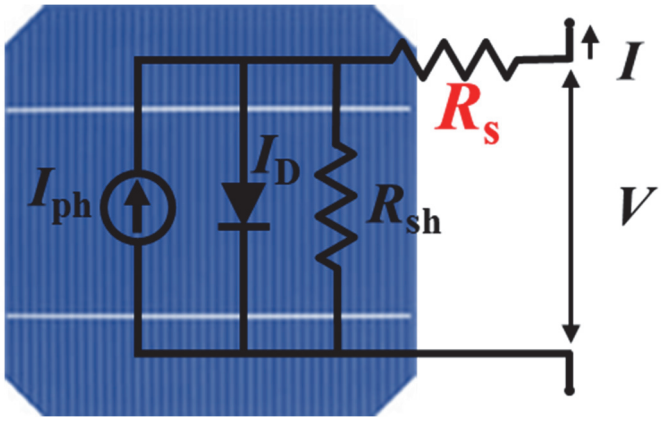

Figure 6.3. Series resistance parameter illustrated by a one–diode equivalent circuit.

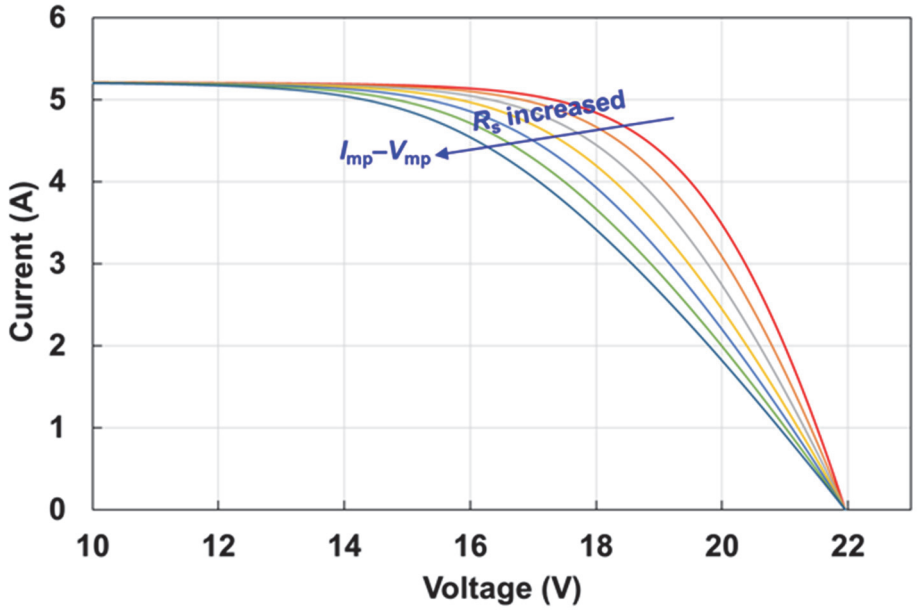

Figure 6.4. Effect of increased in R_s on *I–V* curve and appearance to lower voltage.

The PID presents the potential difference between the active layers, and the grounded metal frames constitute the driving force [37]. This leakage current flow which rather small but not negligible. It depends on the specific technology. This current can have different detrimental impacts on the long–term PV module performance. The PID can lead to significant power loos of the outdoor operating PV modules via shunting of the incorporated PV cell. The PID effect can generally report using EL imaging technique, as shown in Fig. 6.5 [80]. The PID affected PV module revealing different degrees of degradation for the individual cells. Figure 6.6 shows the individual *I–V* curves of cells from two uppermost strings of the module demonstrated from the little degrade (solid lined) to strong degradation and more ohmic characteristics (dashed line).

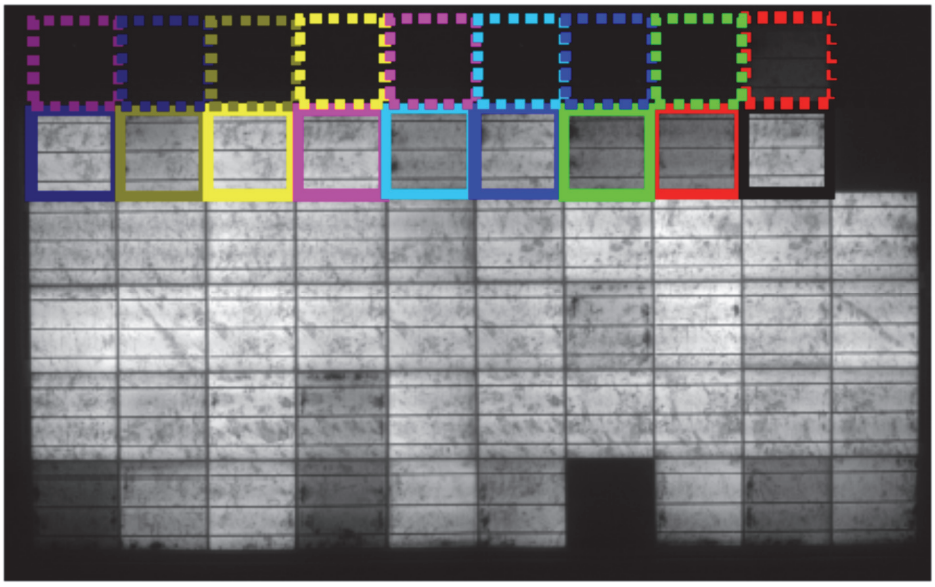

Figure 6.5. EL image of PID affected module [80].

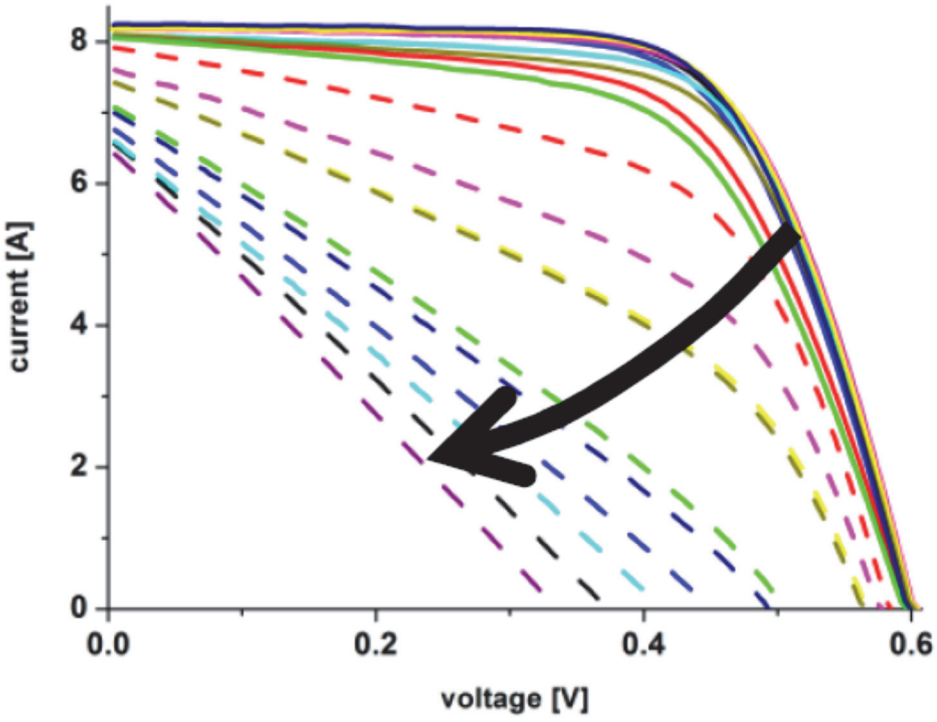

Figure 6.6. *I–V* curve of individual cells undergoing different degrees of PID [80].

6.2 Methods

6.2.1 Temperature correction of V_{mp} and I_{mp}

The V_{mp} and I_{mp} values, which are available without breaking the system's MPPT operation of commercial crystalline silicon PV module, are useful for characterization by using the recent correction formulas [68]. Figure 6.1 shows an example of the correction of V_{mp} and I_{mp} for temperature. Because the experimental timeline data of V_{mp} are strongly affected by the variation of the module temperature (T_m), the measured raw data of the I_{mp}–V_{mp} curve has a rather complex shape, as shown by the black symbols in Fig. 6.1. Therefore, further precise analysis is difficult based on the raw I_{mp}–V_{mp} curve. The measured V_{mp} and I_{mp} are corrected to 25 °C using Eqs. (4.22) and (4.23) [68], which are indicated by red symbols in Fig. 6.7. α is estimated to have a typical value of 0.05 %/K [26, 81]. An advantage of these formulas over the previously proposed ones [26, 68, 82, 83] is that they are applicable to various crystalline silicon PV modules without advanced information of *I–V* curve parameters or diode parameters. Evidently, the variation of V_{mp} due to the fluctuation of the measured module temperature

T_1 is significantly reduced by the temperature correction, and the relation between V_{mp} and I_{mp} (e.g., the I_{mp}–V_{mp} curve) is well defined. The standard deviation, σ, of V_{mp2} in the I_{mp} ranges of 4.6 ± 0.25 A was relative 0.02 V. The variation of V_{mp} in the same range of I_{mp} is approximately ±1 %.

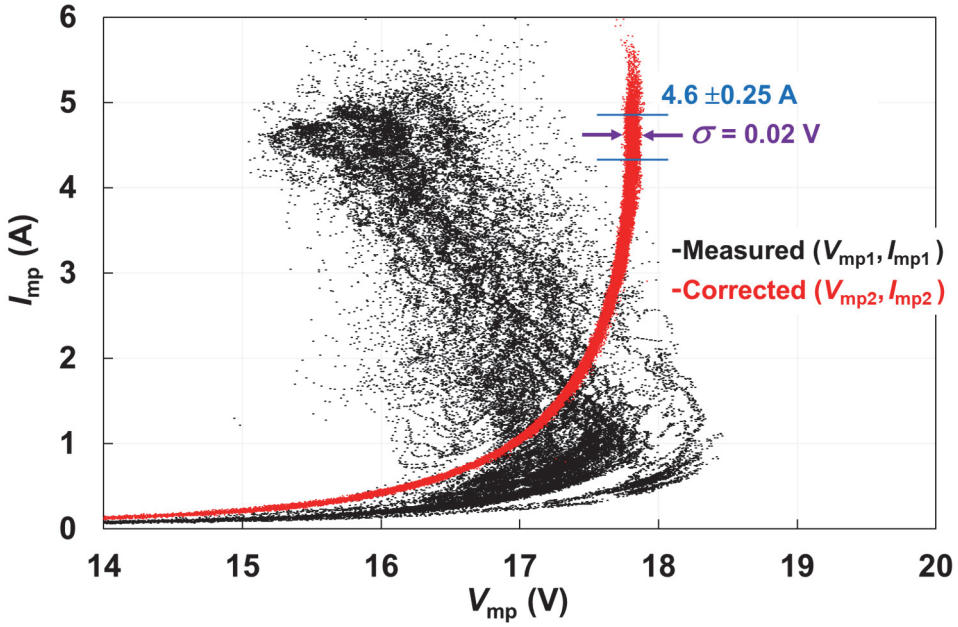

Figure 6.7. Measured V_{mp} and I_{mp} values are shown by the black symbols. The red symbols show the curve corrected to 25 °C using Eqs. (4.22) and (4.23). Details of the experiments are presented in Chapter 4.

6.2.2 Cell crack

Many types of cracks appear on crystalline–silicon PV, which occur in production processes, transportation, installation, thermal stress, improper cleaning, vibration, and maintenance stages [84]. The crack area expands through its operation time and affects the PV module and system performance. In this study, numerical simulation was performed to investigate the possible detection of cell cracks using the I_{mp}–V_{mp} curve. A cracked cell was represented by a cell with a reduced active area, as an example in Fig. 6.8. The output current of a silicon PV cell for simulation in this study was expressed by the Bishops model, Eq. 5.1 [71]. In Eq. 5.1, parameter a is the fraction of ohmic current involved in avalanche breakdown, m is the avalanche breakdown exponent, and V_{br} is the junction breakdown

voltage. V_{br} is known to be in the range between -12 V and -30 V for a mono–crystalline–silicon cell [65]. For the cracked cell, I_{ph} and I_0 were assumed to be proportional to the active area of the cell. Therefore, R_s and R_{sh} are assumed to be inversely proportional to the cell area. The I_{mp} and V_{mp} of a module with one cracked cell were determined from the *I–V* curve of the module, where the output voltage of the module was calculated by the sum of the voltage of the component cells. For the simulation, the total number of series–connected cells in the module was assumed to be 36, with two bypass diodes. A model of a cracked cell for simulation is shown in Fig. 6.8, where the dark area is considered as the inactive area.

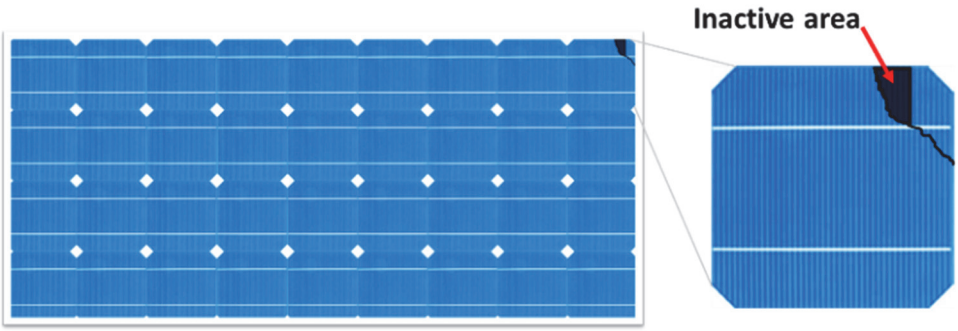

Figure 6.8. Model of a module with a cell with crack. The black line shows a crack on a cell, and a dark area shows an inactive area.

6.2.3 Effect of R_s

A numerical simulation was performed for assessing the degradation with increasing R_s. The I_{mp} and V_{mp} of a module with one cell with increased R_s were determined from the *I–V* curve of the module. A model of a module with an increased R_s is shown in Fig. 6.9, which exhibits the interconnection failure or solder bond failure as an example of increased R_s–based degradation.

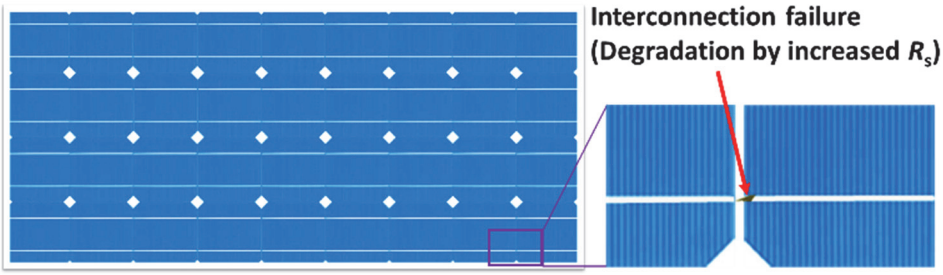

Figure 6.9. Model of a module with a cell with an increased R_s; an interconnection failure is an example of degradation by increased R_s.

6.2.4 Effect of PID

The PID depends on the polarity and voltage level between the cell and ground. Because the PV system is installed with high–voltage levels up to 1000 V, the leakage currents between the cell and ground are presented [37, 85]. The PID has a significant performance degradation by shunting of the cell [80, 86-88]. A numerical simulation was performed to assess the degradation with PID. A model of a module with a PID behavior exhibits in Fig. 6.10, which shows the PID degradation in the brown cells for (a) 1, (b) 9, and (c) 36 cells.

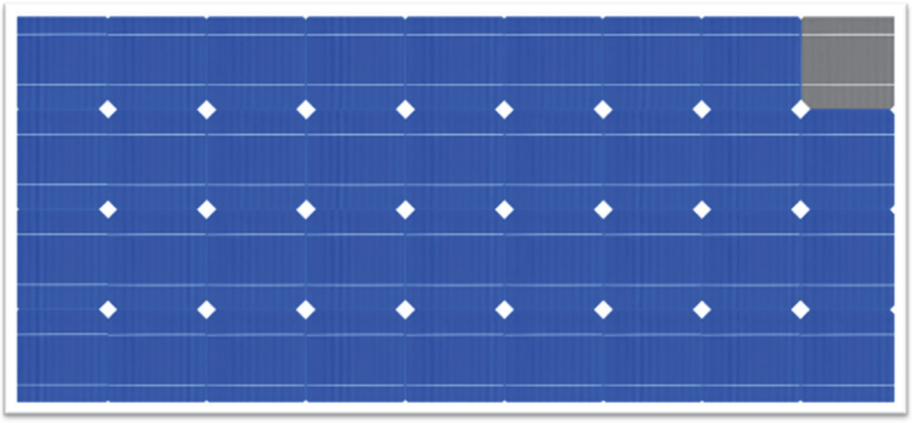

(a), 1–cell PID model

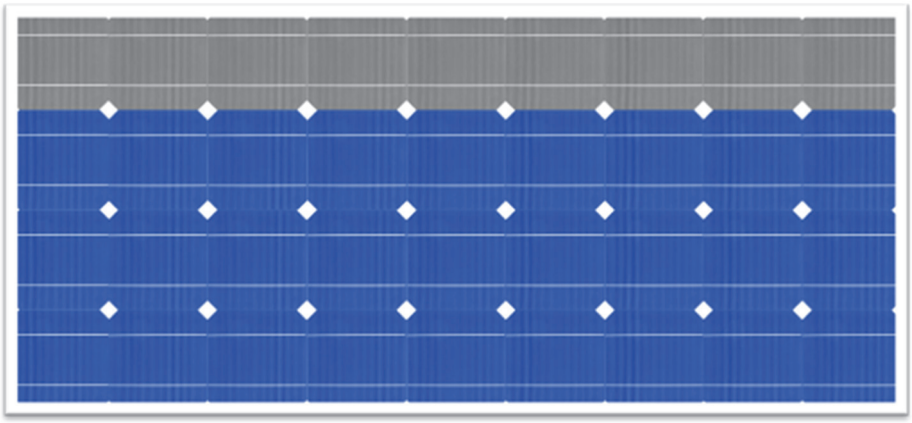

(b), 9–cell PID model

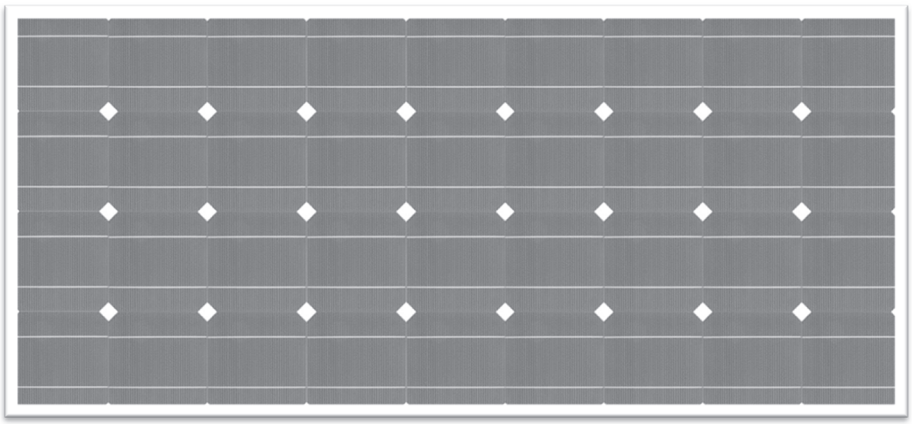

(c), 36–cell PID model

Figure 6.10. Model of a module with PID effect. Brown areas on (a)1 cell, (b) 9 cells, and (c) 36 cells are an example of degradation by PID effect.

6.3 Results and Discussions

6.3.1 Simulation of cell crack effect

The numerical simulations of the I_{mp}–V_{mp} curves of a crystalline–silicon PV module with and without a cracked cell using Eq. (5.1) were carried out, as shown in Fig. 6.11 by the blue lines and red line, respectively. For the cell without a crack, the cell parameters of I_{ph} = 5.262 A at irradiance (G) = 1.0 kW/m^2, $I_0 = 5.3 \times 10^{-9}$ A, R_s = 6.4 mΩ/cell, R_{sh} = 7 Ω/cell, n = 1.147, T = 25 °C, a = 0.1, V_{br} = -30 V, and m = 4 were chosen to fit the experimental data of Fig. 6.7. The results show that the I_{mp}–V_{mp} curve with a cracked cell shifts toward a higher voltage as the ratio of cracked cell increases. A crack of 7 % and 14 % of the cell area resulted in a shift in V_{mp} of approximately 0.18 V and 0.90 V, respectively. Considering the result shown in Fig. 6.7, the experimental scatter in V_{mp} can be suppressed to 0.14 V by the temperature correction. The plots in Fig. 6.11 suggest that a cell crack in the range of 7 – 14 % can be detected by the I_{mp}–V_{mp} curve. This agrees well with the prior simulation an inactive area of more than 8 % of one single cell affects power loss in the PV module [34]. An experiment to perform the cell crack was showed the parallel crack to the busbar, which shows peak potential separated cell area in worst case about 24 % cell area [89]. An example of the V_{mp} and I_{mp} variation by a cracked cell is shown in Fig. 6.12, where one cell in the PV module is 14 % cracked. The V_{mp} and I_{mp} of a cracked cell decrease. However, the V_{mp} of other cells in the module increases because the I_{mp} of the whole module decreases (ΔI_{mp}) due to the current continuity of the series–connected cells. As a result, the sum of the V_{mp} of a cell with crack and the other cells without a crack in the module increase (ΔV_{mp}).

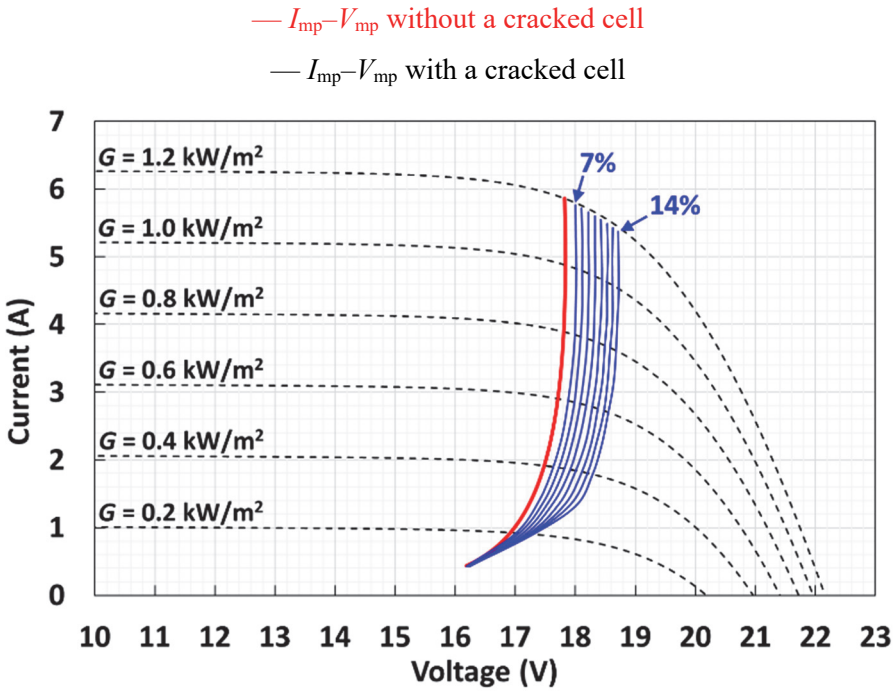

Figure 6.11. The I_{mp}–V_{mp} curves of a PV module with and without cell cracks are represented by the blue lines and red line, respectively. One of the 36 series–connected cells was assumed to have a crack ranging from 7 % to 14 % of the cell area. The *I*–*V* curves of the module under an irradiance range of 0.2 – 1.2 kW/m^2 are also shown by dashed black lines.

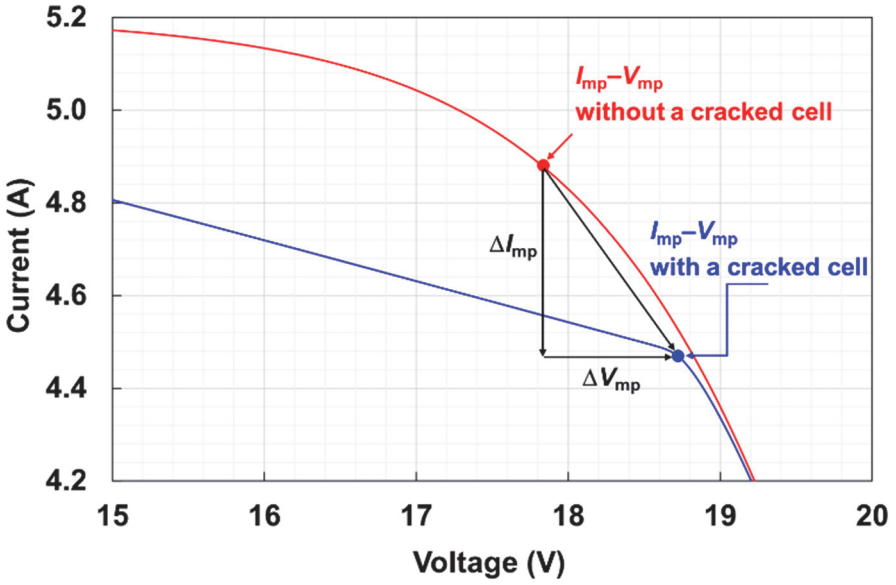

Figure 6.12. An illustration of the V_{mp} and I_{mp} variation by a cracked cell in the module with the 36 series–connected cells, where one cell in the PV module is 14 % cracked. The I–V curves with and without cracked cells are shown by the blue and red curves, respectively.

6.3.2 Simulation of R_s effect

The results of the simulation with and without a cell with an increased R_s are demonstrated by the blue lines and a red line in Fig. 6.13, respectively. The parameters of normal cells (i.e., without an increased R_s) were assumed to be identical to those in Fig. 6.11. The results show that the I_{mp}–V_{mp} curve with an increased R_s shifts toward lower voltages as R_s increases. The shift in V_{mp} is larger for a higher I_{mp} or a higher irradiance. The figure indicates that the shift in V_{mp} at I_{mp} of about 5.66 A amounts to 0.50 – 2.88 V when R_s is increased to 0.1 – 0.6 Ω on one cell. Therefore, the present results suggest that an increase in R_s in the range of 0.1 – 0.6 Ω in one cell can be detected by the I_{mp}–V_{mp} curve.

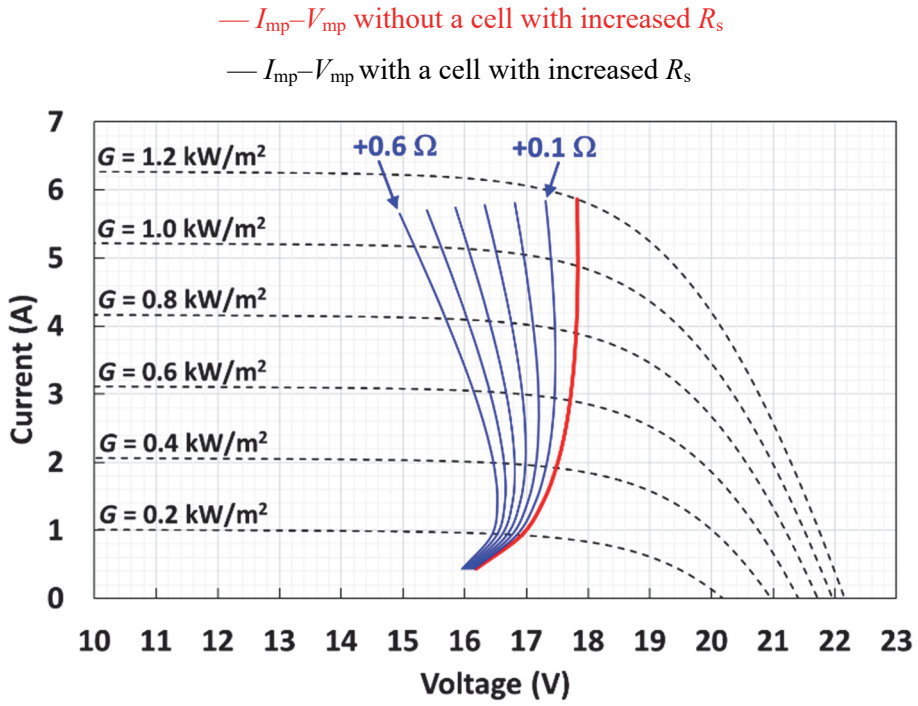

Figure 6.13. The I_{mp}–V_{mp} curves of a PV module with and without an increase in series resistance are represented by the blue lines and red line, respectively. One of the 36 series–connected cells was assumed to have an increased R_s. The *I–V* curves of the module under an irradiance range of 0.2 – 1.2 kW/m^2 are also shown by dashed black lines.

6.3.3 Simulation of PID effect

The PID affects the *I–V* curves of the PV cell from little damage to strong degradation, which are simulated at constant irradiance, as shown in Fig. 6.14. The simulation results of I_{mp}–V_{mp} curves with and without a cell with the PID effect of a cell are illustrated by blue and red lines in Fig. 6.15, respectively. The parameters of normal cells (without PID effect) were assumed to be identical to those in Fig. 6.11. Normally the PID affects the R_{sh} of the PV cell and reduces the *I–V* curve fill factor [32, 90-92]. Therefore, the following simulation results are shown by reducing the R_{sh} in order to illustrate the PID expansion.

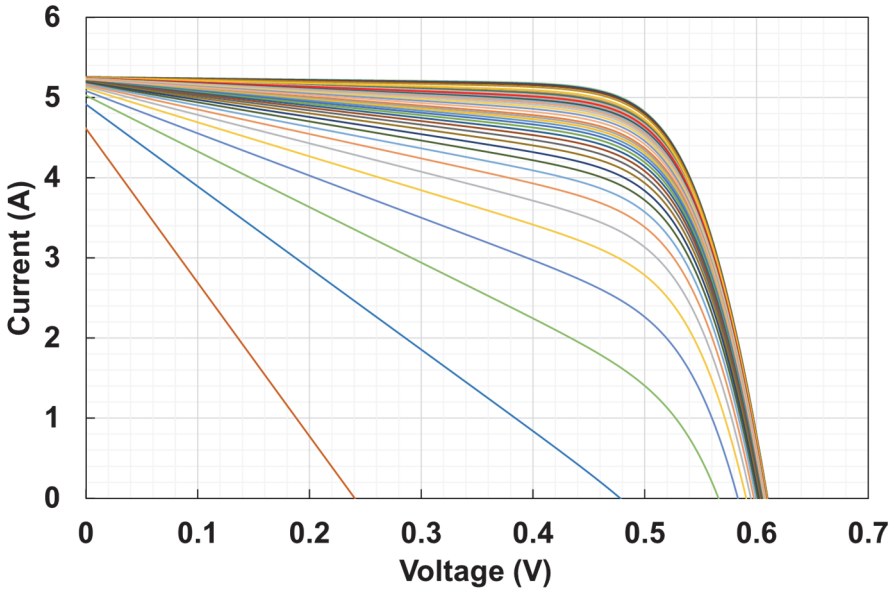

Figure 6.14. The *I–V* curves of a PV cell under PID effects from little damage to strong degradation, which were simulated at constant irradiance.

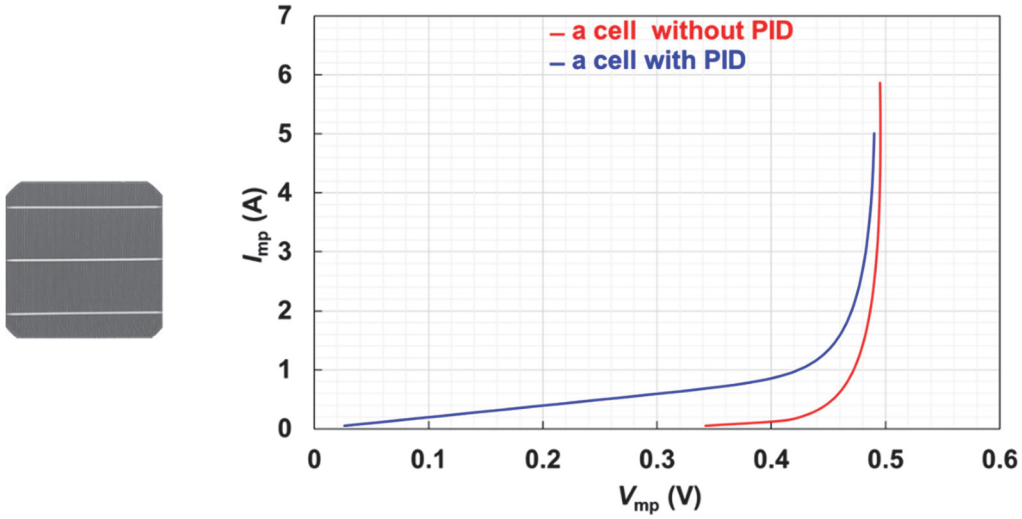

Figure 6.15. I_{mp}–V_{mp} curves of a PV cell with and without PID effect, represented by blue and red line, respectively.

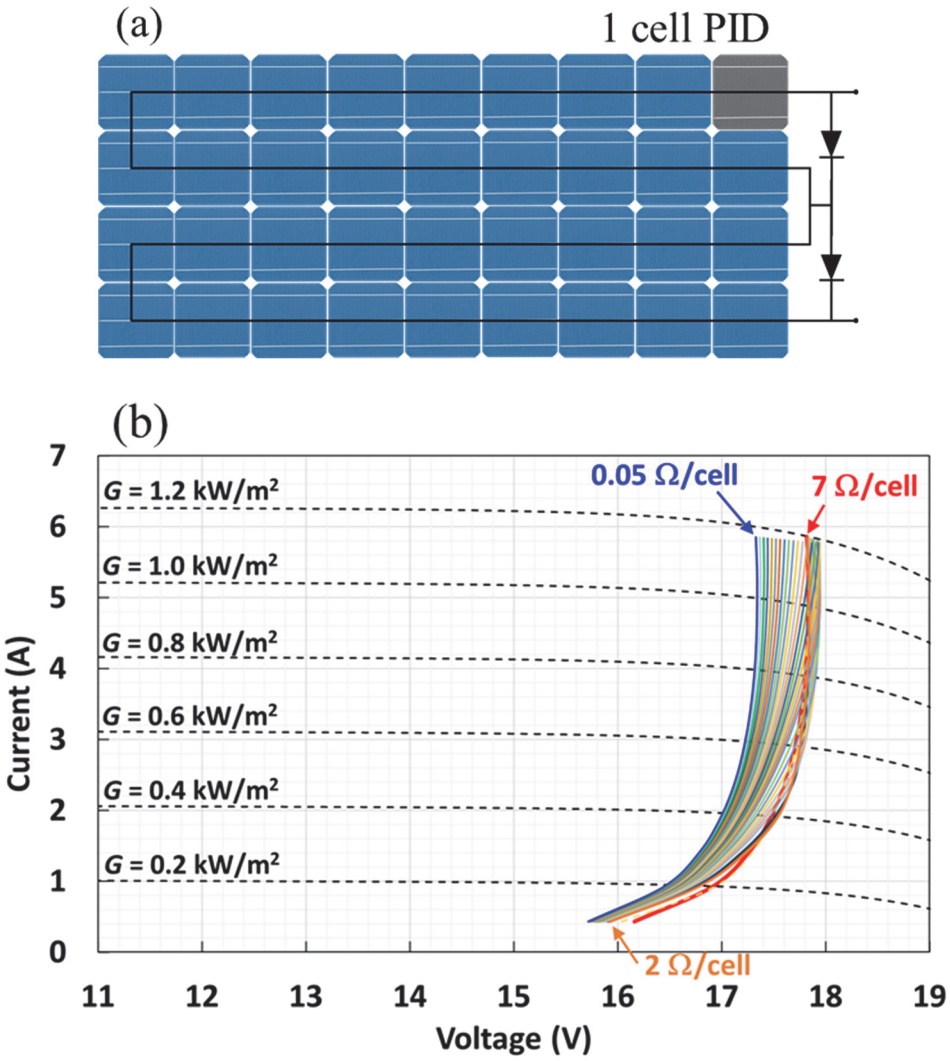

Figure 6.16. One of the 36 series–connected cells was assumed to have a PID. (a) The PID effect is illustrated by the brown area on one cell. (b) The I_{mp}–V_{mp} curves of a PV module with and without PID are represented by color lines and a red line, respectively.

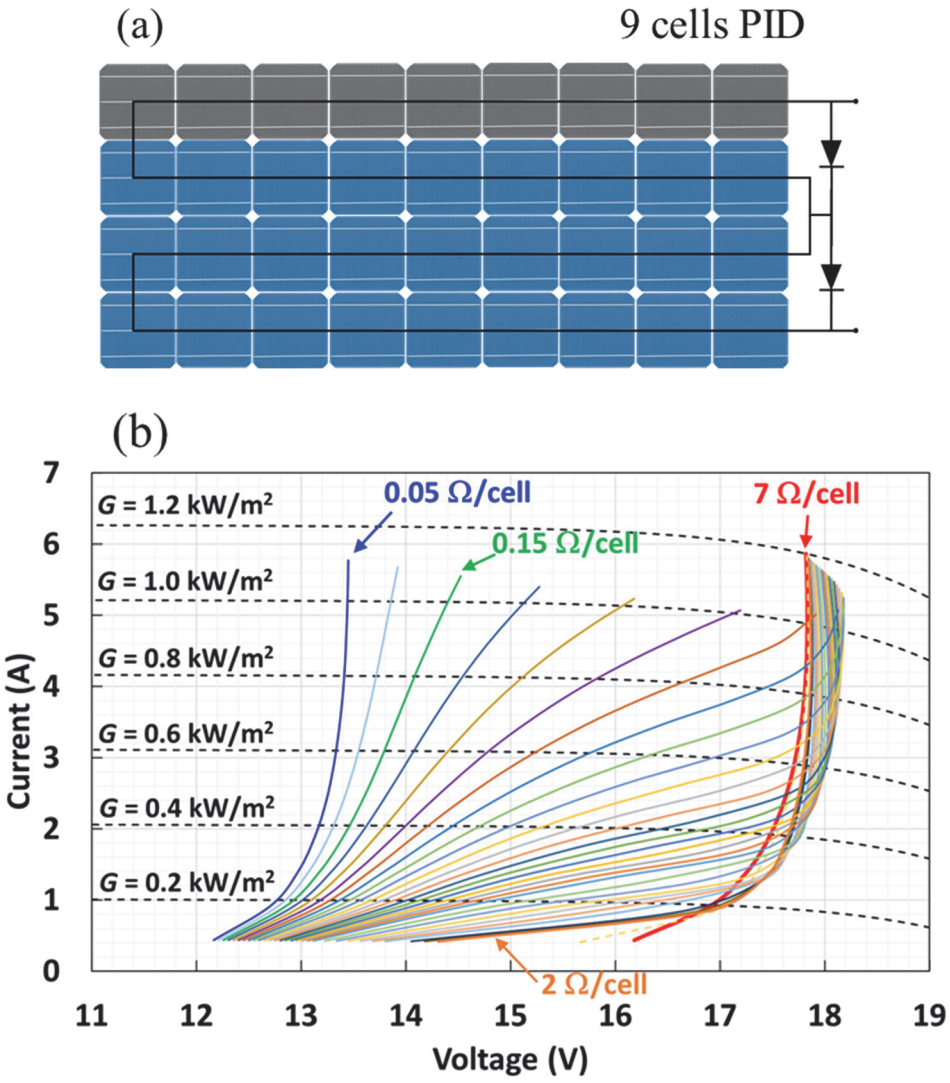

Figure 6.17. Nine of the 36 series–connected cells were assumed to have a PID. (a) The PID effect is illustrated by the brown areas. (b) The I_{mp}–V_{mp} curves of a PV module with and without PID are represented by color lines and a red line, respectively.

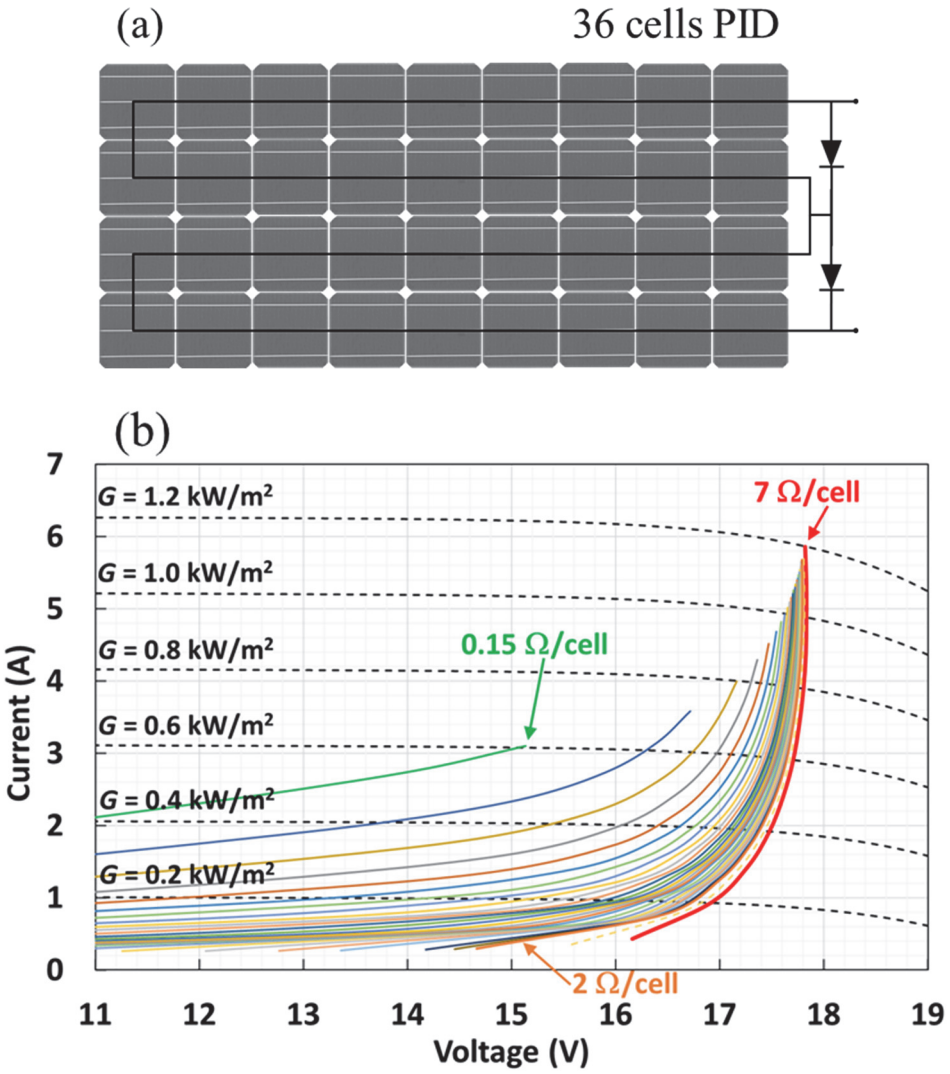

Figure 6.18. The 36 series–connected cells were assumed to have a PID. (a) The PID effect is illustrated by the brown areas. (b) The I_{mp}–V_{mp} curves of a PV module with and without PID are represented by color lines and a red line, respectively.

The I_{mp}–V_{mp} curve of a cell, which has PID, shows that the I_{mp}–V_{mp} curve shifts to a lower voltage, as shown in Fig. 6.15. Then, the case studies for simulations were performed with the 36–cell series–connected PV module, which were varying the PID quantities from 0 % to 99 % of each cell; related to the R_{sh} ranges from 7 Ω/cell to 0.05 Ω/cell. In the case of cell(s) in the module have PID effect, the results of I_{mp}–V_{mp} curves show both increase and decrease in voltages. This results are depended on the PID quantities and irradiance levels, for example, the I_{mp}–V_{mp} curves show both an increase and decrease

in voltage at high irradiance or high I_{mp}, as shown in Figs. 6.16 and 6.17, which are identical with the previous experimental *I–V* measurement after the PID stress test [93]. In Fig. 6.18, when all cells in the module have PID effect, the results show voltage decreases that are identical to a one cell PID effect. However, at low irradiance or small I_{mp}, the results show the voltage shifted to a lower voltage at I_{mp} lower than about 1 A. The results also show that the PID grows more than 70 % on the cells, or the FF of the cells degrade about 13 % due to PID degradation, it can be detected by using I_{mp}–V_{mp} curves.

6.4 Chapter Summary

First, this chapter investigated methods to detect the degradation of a PV module from the temperature–corrected I_{mp}–V_{mp} curve, which is applied for degradation detection, using experimental data. It is an advantage over the *I–V* curve measurement which needs to interrupting the MPPT operation. In this study, the time–series data of experimental I_{mp} and V_{mp} are corrected for temperature using recently developed formulas to reduce the scatter in V_{mp} due to the large variation in the module temperature and to clarify the I_{mp}–V_{mp} curve. The simulation results indicate that the I_{mp}–V_{mp} curve of a module shifts toward high V_{mp} when the existence of a cracked cell in the module has occurred. Therefore, the existence of a cracked cell in the module can be detected by the shift of the I_{mp}–V_{mp} curve toward a higher voltage. It is found that a cell crack in the range of approximately 7 – 14 % in one cell can be detected using the I_{mp}–V_{mp} curve. Second, the results show that the I_{mp}–V_{mp} curve shifts toward lower voltages as R_s increases. The shift in V_{mp} increases for a higher I_{mp} or a higher irradiance. Therefore, an increase in R_s can also be detected from the I_{mp}–V_{mp} curve. An increase in R_s in the range of approximately 0.1 – 0.6 Ω in one cell can be detected using the I_{mp}–V_{mp} curve. In addition, the simulation results also indicate that the I_{mp}–V_{mp} curves are distorted by the PID effect. Although the I_{mp}–V_{mp} curves shift to lower and higher voltage, most of them shift significantly to the lower voltage in the low I_{mp} or low irradiance. The results are applicable not only to a single PV module but also to a PV system where multiple modules are connected in series. The detection sensitivity should vary depending on the PV module type and the measurement conditions of I_{mp} and V_{mp}.

The proposed method can be flexibly used for various types of PV modules and systems, because it uses only the V_{mp}, I_{mp}, and T_m, which can be measured by inexpensive equipment and without interrupting the MPPT operation. Furthermore, the temperature correction formulas in Eqs. (4.22) and (4.23) can be applied to various kinds of crystalline silicon PV modules without advanced knowledge of module–specific parameters, such as the TC. Therefore, this method is useful for identifying the cell

crack, cell degradation which increases R_s, and PID effect by using the time–series data of I_{mp} and V_{mp} from the PV system monitoring. Experimental confirmation of the obtained results and applicability of the proposed method for other degradation modes, such as bypass diode failure, is subjects of future potential studies in this field.

Chapter 7

Thesis Conclusions

This study investigated the temperature and irradiance dependences of I_{mp} and V_{mp} by using experiments and numerical simulations based upon a one–diode model and obtained the new formulas for temperature correction of V_{mp} and I_{mp}. The novelty is that the developed formulas do not require advanced information of TC or diode parameters, and the voltage–dependence of TC is explicitly considered. They don't need to interrupt the PV modules' MPPT operation as it uses only V_{mp}, I_{mp}, and T_m. This study is the first time using the I_{mp}–V_{mp} curve after correction for the temperature to detect the shading effect of the module. Other detections are also studied, such as a cracked cell in the module, an increased in R_s, and PID effects, as its case study. The details of the research conclusions are as follows.

First, the I–V curves were numerically simulated over the ranges of R_s, R_{sh}, I_0, n, and V_{oc}, which are typical to commercial crystalline–silicon PV devices. The I_{mp} was shown to be nearly constant within ±0.02 %/°C for a temperature range between 0 and 70 °C, which qualitatively agrees with indoor and outdoor experimental results. The simulation also showed that the I_{mp} is nearly proportional to irradiance G, and I_{mp}/G is constant within ±1.3 % in the irradiance range between 0.5 and 1.2 kW/m^2, which also agrees with previous experimental studies.

Based on the numerical simulations and experiments, new translation formulas for the temperature and irradiance of V_{mp} and I_{mp}, i.e., Eqs. (4.22) and (4.23), are proposed, wherein the voltage–dependence of TC is explicitly considered. The I_{mp} versus V_{mp} curves, corrected to 25 °C by the formulas, showed good reproducibility with the σ of voltage in the irradiance range of 1.0 ±0.05 kW/m^2 was improved from the 0.07 V (relative 0.38%) of Eq. (4.9) to 0.02 V (relative 0.13%) over many days of data, which confirms the validity of the correction formulas. The importance of the excellent reproducibility of V_{mp2} by using Eq. (4.22) is also shown to agree very well with the I_{mp}–V_{mp} point at STC. The typical value of experimental confirmation of reproducibility for P_{max} is within 0.24 % (σ). The novelty of the current study is that the developed formulas do not require advanced information on the TCs or diode parameters. These results are useful for characterizing the performance of commercial crystalline silicon PV devices by using the I_{mp} and V_{mp} values which can be obtained without interrupting the PV modules' MPPT operation.

Second, based on the aforementioned approach, a method to detect partial shading on a PV module (during MPPT operation) from the experimental I_{mp} and V_{mp}, has been investigated. The experimental I_{mp} and V_{mp} were corrected for temperature by using the developed formulas, in order to reduce the scatter in V_{mp} due to variation of temperature. The experiments and numerical simulations indicate that the corrected experimental I_{mp}–V_{mp} curve shows a clear increase in V_{mp}, under the effect of partial shade. The shape of the shaded I_{mp}–V_{mp} curve matches the results of numerical simulations including the series connection of shaded and unshaded cells. The simulation results for vertical and horizontal partial shading show similar increase in V_{mp}, which indicate that the increase in the V_{mp} is due to the nonuniformity of the photocurrent of the cells. Therefore, the existence of partial shade can be detected by the shift of the I_{mp}–V_{mp} curve toward higher voltage. The results of this study can be used to identify shading effects without *I–V* curve measurements. They are expected to identify slight shading effect of about 5 – 10 %, which is difficult to be detected by the raw I_{mp} and V_{mp} data. The shading effect is a time–dependent, reproducible, and impermanent degradation. This method for detecting the shading effect uses only I_{mp}, V_{mp}, T_m, and G, and it can be used with various kinds of crystalline–silicon modules without advance knowledge of module–specific parameters such as the TC. Therefore, the method is expected to be helpful for identifying the partial shading by using the continuous monitoring data of PV systems, and separating the shading effect from other factors such as module degradation and breakage.

Third, this study is the first to investigate methods of detecting degradation of a PV module from the temperature–corrected I_{mp}–V_{mp} curve, which is applied for degradation detection, using experimental data. Hence, it offers an advantage over *I–V* curve measurements, which needs to interrupt the MPPT operation. In this study, the time–series data of experimental I_{mp} and V_{mp} were corrected for temperature using the recently developed formulas to reduce the scatter in V_{mp} due to the large variation in the module temperature, as well as to clarify the I_{mp}–V_{mp} curve. The simulation results indicate that the I_{mp}–V_{mp} curve of the module is shifted toward high V_{mp} when the existence of a cracked cell is present in the module. Therefore, the existence of a cracked cell in the module can be detected from the shift of the I_{mp}–V_{mp} curve toward higher voltage. It is found that a cell crack in the range of approximately 7 – 14 % in one cell can be detected using the I_{mp}–V_{mp} curve. The results show that the I_{mp}–V_{mp} curve shifts toward lower voltages when R_s increases. The shift in V_{mp} increases for a higher I_{mp} or a higher irradiance. Therefore, the increase in R_s can also be detected from the I_{mp}–V_{mp} curve. An increase in R_s in the range of approximately 0.1 – 0.6 Ω in one cell can be detected using the I_{mp}–V_{mp} curve. In addition, the simulation results also indicate that the I_{mp}–V_{mp} curves are distorted by PID. Although the I_{mp}–V_{mp} curves are shifted to lower and higher voltage, most of them are significantly shifted to lower voltage under low I_{mp} or low irradiance. The proposed method can be flexibly used for various types of PV modules and systems, because it uses only V_{mp}, I_{mp}, and T_m, which can be measured

by inexpensive equipment and without interrupting the MPPT operation. Therefore, this method is useful for identifying the cell crack, increase in R_s, and PID effect, using the time–series data of I_{mp} and V_{mp} obtained from the PV system data monitoring. Experimental confirmation of the obtained results, and the applicability of the proposed method to other degradation modes, such as bypass diode failure, are subjects of future potential studies in this field.

Furthermore, the temperature correction formulas in Eqs. (4.22) and (4.23) can be applied to various kinds of crystalline–silicon PV modules without advanced knowledge of module–specific parameters, such as the TC or diode parameters. The detection sensitivity should vary depending on the type of PV module and the measurement conditions of I_{mp} and V_{mp}. The present study used a conventional silicon BSF PV module. Nearly the same formulas are expected to be applicable to other types such as PERC, backside contact, and heterojunction without modification or with only slight modification in nE_g/q and α. However, the method is applicable not only to a single PV module but also to a PV system in which multiple modules are connected in series, because its deterioration affects to the V_{mp}, whilst the output current of the PV string is the same as the current of the degradation cells/modules. The method's application to PV arrays, in which multiple modules are series–parallel connected, remains a target for future studies.

Once the partial shading is detected by the method of the present study, the source of the shade may be removed in order to improve the PV performance if possible, such as soiling on the module or weeds. When failures such as an increase in R_s, cell crack, or PID are detected, the responsible modules will be identified and replaced if necessary. As a result, PV modules or PV systems deteriorations, such as outages, energy production problems, low energy production, and severed risk, can be prevented and fixed in time.

References

[1] IEA (2020), World Energy Outlook 2020, IEA, Paris https://www.iea.org/reports/world-energy-outlook-2020

[2] REN21. 2020. Renewables 2020 Global Status Report (Paris: REN21 Secretariat)

[3] Jäger-Waldau A. Snapshot of Photovoltaics–February 2020. Energies. 2020, 13(4), 930. https://doi.org/10.3390/en13040930

[4] IEA-PVPS T1-39, 2021. Snapshot of Global PV markets 2021. IEA-PVPS Task 1 report. https://iea-pvps.org/snapshot-reports/snapshot-2021.

[5] IEA-PVPS T1-38, 2020. Trends in Photovoltaic Applications 2020. IEA-PVPS Task 1 report.

[6] Andreani L. C., Bozzola A., Kowalczewski P., LiscidinM. i, Redorici L., Silicon solar cells: toward the efficiency limits. Advances in Physics: X, 2019, Vol. 4, No. 1, pp. 125-148.

[7] Luque A., Hegedus S., Handbook of Photovoltaic Science and Engineering, Second Edition, John Wiley & Sons Ltd, West Sussex, UK, 2011.

[8] IEC 60904-3, 2016. Photovoltaic devices – Part 3: Measurement principles for terrestrial photovoltaic (PV) solar devices with reference spectral irradiance data, 2016.

[9] Cuce E., Cuce P. M., Karakas I. H., Bali T., An accurate model for photovoltaic (PV) modules to determine electrical characteristics and thermodynamic performance parameters. Energy Conversion and Management, 2017, Vol. 146, 205-216.

[10] Cuce P. M., Cuce E., A novel model of photovoltaic modules for parameter estimation and thermodynamic assessment. International Journal of Low-Carbon Technologies, 2012, Vol. 7, 159-165.

[11] Achouby H. E., Zaimi M., Ibral A., Assaid E.M., New analytical approach for modeling effects of temperature and irradiance on physical parameters of photovoltaic solar module. Energy Conversion and Management, 2018, Vol. 177, 258-271.

[12] Wang J. C., Su Y. L., Shieh J. C., Jiang J. A., High-accuracy maximum power point estimation for photovoltaic arrays. Solar Energy Materials & Solar Cells, 2011, Vol. 95, 843–851.

[13] Zaimi M., Achouby H. E., Ibral A., Assaid E. M., M Maliki. S. E., Saadani R., Temporal monitoring of temperature and incident irradiance for predicting photovoltaic solar module peak power and efficiency using analytical expressions of model physical parameters, 6th International Renewable and Sustainable Energy Conference (IRSEC), Rabat, Morocco, 2018, 1-7.

[14] Zaimi M., Achouby H. E., Ibral A., Assaid E. M., Determining combined effects of solar radiation and panel junction temperature on all model-parameters to forecast peak power and photovoltaic yield of solar panel under non-standard conditions, Solar Energy, 2019, Vol. 191, 341-359.

[15] Anderson A. J., Photovoltaic Translation Equations: A New Approach. NREL/TP-411-20279, 1996.

[16] Batzelis E. I., Simple PV Performance Equations Theoretically Well Founded on the Single-Diode Model. IEEE Journal of photovoltaics, 2017, Vol. 7, No. 5, 1400-1409.

[17] King B. H., Hansen C. W., Riley D., Robinson C. D., Pratt L., Procedure to Determine Coefficients for the Sandia Array Performance Model (SAPM). Sandia report, SAND2016-5284, 2016.

[18] King D. L., Boyson W. E., Kratochvil J. A., Photovoltaic Array Performance Model. Sandia report, SAND2004-3535, Unlimited Release, 2004.

[19] King D. L., Eckert P. E., Characterizing (rating) the performance of large photovoltaic arrays for all operating conditions. The 25th IEEE PVSC, Washington, D.C., May 13-17, 1996, 1385–1388.

[20] King D. L., Kratochvil J. A., Boyson W. E., Temperature Coefficients for PV Modules and Arrays: Measurement Methods, Difficulties, and Results. The 26th IEEE PVSC, Anaheim, California, September 29- October 3, 1997.

[21] Whitaker C. M., Townsend T. U., Newmiller J. D., King D. L., Boyson W. E., Kratochvil J. A., Collier D. E., Osborn D. E., Application and validation of a new PV performance characterization method. The 26th IEEE PVSC, Anaheim, CA, 1997, 1253–1256.

[22] Wurfel P., Physics of Solar Cells: From Principles to New Concepts. WILEY-VCH Verlag GmbH & Co. KGaA, Weinheim, 2005, 167-169.

[23] Sze S. M., Ng K. K., Physics of Semiconductor Devices. 3rd ed., John Wiley & Sons, Inc. New Jersey, 2006, 720-725.

[24] Wenham S. R., Green M. A., Watt M. E., Corkish R., Applied Photovoltaics, 2nd ed., UNSW Centre for Photovoltaic Engineering, 2006.

[25] IEC 60891: 2009. Photovoltaic devices – Procedures for temperature and irradiance corrections to measured I–V characteristics, 2009.

[26] Hishikawa Y., Doi T., Higa M., Yamagoe K., Ohshima H., Takenouchi T., Yoshita M., Voltage-Dependent Temperature Coefficient of the I-V Curves of Crystalline Silicon Photovoltaic Modules. IEEE Journal of photovoltaics, 2018, Vol. 8, No. 1, 48-53.

[27] Kasu M., Abdu J., Hara S., Choi S., Chiba Y., Masuda A., Temperature dependence measurements and performance analyses of high-efficiency interdigitated back-contact, passivated emitter and rear cell, and silicon heterojunction photovoltaic modules. Japan Journal of Applied Physics, 2018, Vol. 57, 08RG18-1 to 08RG18-7.

[28] Sun X., Chavali R.V.K., Alam M.A., Real-time monitoring and diagnosis of photovoltaic system degradation only using maximum power point - the Suns-Vmp method. Progress in Photovoltaics Res Appl., 2018, 1–12.

[29] Sun X., Chavali R.V.K., Alam M.A., In-Situ Self-Monitoring of Real-Time Photovoltaic Degradation Only Using Maximum Power Point – the Suns-Vmp Method. Applied Physics, Cornell University, eprint arXiv:1802.01206, 2018.

[30] Gallardo-Saavedra, S., Hernandez-Callejo, L., Alonso-Garcia, M.d.C., Santos, J. D., Morales-Aragones, J. I., Alonso-Gomez, V., Moreton-Fernandez, A., Gonzalez-Rebollo, M. A., Martinez-Sacristan, O., Nondestructive characterization of solar PV cells defects by means of electroluminescence, infrared thermography, I–V curves and visual tests: Experimental study and comparison. Energy 205, 2020, 117930.

[31] Ballestin-Fuertes J., Munoz-Cruzado-Alba J., Sanz-Osorio J. F., Hernandez-Callejo L., Alonso-Gomez V., Morales-Aragones J. I., Gallardo-Saavedra S., Martinez-Sacristan O., Moreton-Fernandez A., Novel utility-scale photovoltaic plant electroluminescence maintenance technique by means of bidirectional power inverter controller. Appl. Sci. 10 (9), 2020, 3084.

[32] Kwembur I.M., Crozier McCleland J.L., van Dyk E.E., Vorster F.J., Detection of potential induced degradation in mono and multi-crystalline silicon photovoltaic modules. Physica B: Phys. of Cond. Matt. 581, 2020, 411938.

[33] Kontges M., Kunze I., Kajari-Schroder S., Breitenmoser X., Bjorneklett B., Quantifyying the risk of power loss in PV modules due to micro cracks. The 25th European Photovoltaic Solar Energy Conference, 2010, 1-8.

[34] Kontges M., Kunze I., Kajari-Schroder S., Breitenmoser X., Bjorneklett B., The risk of power loss in crystalline silicon based photovoltaic modules due to micro-cracks. Sol. Energy Mat.&Sol. Cells 95, 2011, 1131-1137.

[35] Gade V., Shiradkar N., Paggi M., Opalewski J., Predicting the long term power loss from cell cracks in PV modules. The 42nd IEEE Photovoltaic Specialist Conference (PVSC), 2015, 1-6.

[36] Haque A., Bharath K.V.S., Khan M.A., Khan I., Jaffery Z.A., Fault diagnosis of photovoltaic modules. Energy Sci. Eng. 7, 2019, 622-644.

[37] Pingel S., Frank O., Winkler M., Daryan S., Geipel T., Hoehne H., Berghold J., Potential induced degradation of solar cells and panels. The 35th IEEE Photovoltaic Specialists Conference (PVSC), Honolulu, HI, 2010, 2817-2822.

[38] Messenger R., Ventre J., Photovoltaic systems engineering, CRC Press, Boca Raton, FL, 2003.

[39] Seapan M., Hishikawa Y., Yoshita M., Okajima K., Temperature and Irradiance Dependence of Current and Voltage at Maximum Power of Crystalline Silicon Photovoltaic Modules, The 46th IEEE PVSC, Chicago, IL, USA, June 16-21, 2019, 2583-2587.

[40] Moser D., Pichler M., Dimitrova M. N., Filtering Procedures for Reliable Outdoor Temperature Coefficients in different Photovoltaic Technologies. Journal of Solar Energy Engineering, vol. 136, 2014, 1-10.

[41] Drouiche I., Harrouni S., Arab A. H., A new approach for modeling the aging PV module upon experimental I-V curves by combining translation method and five-parameters model. Electric Power Systems Research, vol. 163, 2018, 231-241.

[42] Ma T., Yang H., Lu L., Development of a model to simulate the performance characteristics of crystalline silicon photovoltaic modules/strings/arrays. Solar Energy, vol. 100, 2014, 31-41.

[43] Sera D., Teodorescu R., Rodriguez P., PV panel model based on datasheet values. IEEE International Symposium on Industrial Electronics, Vigo, Spain, 2007, 2392-2396.

[44] Cuce E., Cuce P. M., Bali T., An experimental analysis of illumination intensity and temperature dependency of photovoltaic cell parameters. Applied Energy, vol. 111, 2013, 374-382.

[45] Fukabori A., Takenouchi T., Matsuda Y., Tsuno Y., Hishikawa Y., Study of highly precise outdoor characterization technique for photovoltaic modules in terms of reproducibility. Japan Journal of Applied Physics, vol. 54, 2015, 08RG06-1 to 08RG06-6.

[46] Hishikawa Y., Doi T., Higa M., Yamagoe K., Ohshima H., Precise outdoor PV module performance characterization under unstable irradiance. IEEE J. Photovoltaics 6 (5), 2016, 1221-1227.

[47] Hishikawa Y., Doi T., Higa M., Yamagoe K., Ohshima H., Masuda K., Wakabayashi H., Precise outdoor PV module performance measurements at various irradiance levels. The 43rd IEEE Photovoltaic Specialists Conference (PVSC), Portland, OR, USA, 2016, 3680-3684.

[48] Singh P., Singh S. N., Lal M., Husain M., Temperature dependence of I-V characteristics and performance parameters of silicon solar cell, Solar Energy Materials & Solar Cells, vol. 92, 2008, 1611–1616.

[49] Singh P., Ravindra N. M., Temperature dependence of solar cell performance – an analysis, Solar Energy Materials & Solar Cells, vol. 101, 2012, 36–45.

[50] Green M. A., Solar cells: operating principles, technology, and system applications, Englewood Cliffs, NJ, Prentice-Hall, 1982.

[51] Bensalem S., Chegaar M., Herguth A., Band gap dependence with temperature of semiconductors from solar cells electrical parameters. Current Applied Physics, vol. 17, 2017, 55-59.

[52] Varshni Y. P., Temperature dependence of the energy gap in semiconductors. Physica, vol. 34, 1967, 149-154.

[53] Thurmond C. D., The standard thermodynamic functions for the formation of electrons and holed in Ge, Si, GaAs, and Gap. Journal of The Electrochemical Society, vol. 122, no. 8, 1975, 1133-1141.

[54] Alsayid B. A., Alsadi S. Y., Jallad J. S., Dradi M. H., Partial shading of PV system simulation with experimental results. Smart grid and Renew. Energy 4, 2013, 429-435.

[55] Bai J., Cao Y., Hao Y., Zhang Z., Liu S., Cao F., Characteristic output of PV systems under partial shading or mismatch conditions. Sol. Energy 112, 2015, 41-54.

[56] Kawamura H., Naka K., Yonekura N., Yamanaka S., Kawamura H., Ohno H., Naito K., Simulation of I-V characteristics of a PV module with shaded PV cells. Sol. Energy Mater. Sol. Cells 75, 2003, 613-621.

[57] Mahammed I. H., Arab A. H., Berrah S., Bakelli Y., Khennene M., Oudjana S. H., Fezzani A., Zaghba L., Outdoor study of partial shading effects on different PV modules technologies. Energy Procedia 141, 2017, 81-85.

[58] Sun Y., Chen S., Xie L., Hong R., Shen H., 2014. Investigating the impact of shading effect on the characteristics of a large-scale grid-connected PV power plant in Northwest China. Hindawi, International Journal of Photoenergy 2014, 1-9.

[59] Xenophontos A., Bazzi A. M., Model-based maximum power curves of solar photovoltaic panels under partial shading conditions. IEEE J. Photovoltaics 8 (1), 2018, 233-238.

[60] Meyer E. L., Dyk E. E., The effect of reduces shunt resistance and shading on photovoltaic module performance. The 31st IEEE PVSC, Lake Buena Vista, FL, USA, 3-7 Jan., 2005, 1331-1334.

[61] Alonso-Garcia M. C., Ruiz J. M., Herrmann W., Computer simulation of shading effects in photovoltaic arrays. Renewable Energy 31, 2006, 1986-1993.

[62] Gallardo-Saavedra S., Karlsson B., Simulation, validation and analysis of shading effects on a PV system. Sol. Energy 170, 2018, 828-839.

[63] Hemza A., Abdeslam H., Rachid C., Aoun N., Simplified methods for evaluating the degradation of photovoltaic and modeling considering partial shading, Measurement, 138, 2019, 217-224.

[64] Fialho L., Melicio R., Mendes V.M.F., Figueiredo J., Collares-Pereira M., Effect of shading on series solar modules: simulation and experimental results. Procedia Technology 17, 2014, 295-302.

[65] Bressan M., Basri Y.E., Galeano A.G., Alonso, C., A shadow fault detection method based on the standard error analysis of I–V curves. Renew. Energy 99, 2016, 1181-1190.

[66] Galeano A. G., Bressan M., Vargas F. J., Alonso C., 2018. Shading ratio impact on photovoltaic modules and correlation with shading patterns. Energies 2018, 11, 852.

[67] Jung T. H., Ko J. W., Kang G. H., Ahn H. K., Output characteristics of PV module considering partially reverse biased conditions. Sol. Energy 92, 2013, 214-220.

[68] Seapan M., Hishikawa Y., Yoshita M., Okajima K., Temperature and irradiance dependences of the current and voltage at maximum power of crystalline silicon PV devices. Sol. Energy 204, 2020, 459-465.

[69] Hishikawa Y., Yamagoe K., Ohshima H., Tsuno Y., Kojima H., New technology for precise outdoor PV module performance measurement. The 42nd IEEE Photovoltaic Specialist Conference (PVSC), New Orleans, LA, USA, 2015, 1-6.

[70] Wurfel P., Physics of Solar Cells: From Basic Principles to Advanced Concepts. WILEY-VCH Verlag GmbH & Co. KGaA, Weinheim, 2009, 172-182.

[71] Bishop J. W., Computer simulation of the effects of electrical mismatches in photovoltaic cell interconnection circuits. Sol. Cells 25, 1988, 73-89.

[72] Deline C., Dobos A., Janzou S., Meydbray J., Donovan M., A simplified model of uniform shading in large photovoltaic arrays. Sol. Energy 96, 2013, 274-282.

[73] Ghasemi M. A., Foroushani H. M., Parniani M., Partial shading detection and smooth maximum power point tracking of PV arrays under PSC. IEEE Trans. on power electronics 31 (9), 2016, 6281-6292.

[74] Saint-Drenan Y., Barbier T., Data-analysis and modelling of the effect of inter-row shading on power production of photovoltaic plants. Sol. Energy 184, 2019, 127-147.

[75] Ruschel C. S., Gasparin F. P., Costa E. R., Krenzinger A., Assessment of PV modules shunt resistance dependence on solar irradiance. Sol. Energy 133, 2016, 35-43.

[76] Hansen C. W., Parameter estimation for single diode models of photovoltaic modules. Sandia report SAND2015-2065, Albuquerque, USA, 2015.

[77] IEC 61730-1, 2016. Photovoltaic (PV) module safety qualification – Part 1: Requirements for construction, https://webstore.iec.ch/.

[78] Crozier J.L., Dyk Eev., Vorster F.J., Identification and characterisation of performance limiting defects and cell mismatch in photovoltaic modules. J. Energy South. Afr. 26(3), 2015, 19-26.

[79] Swanson R., Cudzinovic M., DeCeuster D., Desai V., Jörn Jürgens, Kaminar N., Mulligan W., Rodrigues-Barbarosa L., Rose D., Smith D., Terao A., Wilson K., The surface polarization effect in high-efficiency silicon solar cells. 15th International PVSEC, Shangai, China, 2005.

[80] Schutze M., Junghanel M., Koentopp M.B., Cwikla S., Friedrich S., Muller J.W., Wawer P., Laboratory study of potential induced degradation of silicon photovoltaic modules. The 37th IEEE Photovoltaic Specialists Conference, 19-24 June 2011, Seattle, WA, USA, 2011, 000821- 000826.

[81] Wenham S.R., Green M.A., Watt M.E., Corkish R., Sproul A., Applied Photovoltaics. London: Routledge, 2011.

[82] Seapan M., Hishikawa Y., Yoshita M., Okajima K., Detection of shading effect by using the current and voltage at maximum power point of crystalline silicon PV modules. Sol. Energy 211, 2020, 1365-1372.

[83] Hishikawa Y., Takenouchi T., Higa M., Yamagoe K., Ohshima H., Yoshita M., Translation of solar cell performance for irradiance and temperature from a single I–V curve without advance information of translation parameters. IEEE J. Photovoltaics 9(5), 2019, 1195-1201.

[84] Bdour M., Dalala Z., Al-Addous M., Radaideh A., Al-Sadi A., A comprehensive evaluation on type of microcracks and possible effects on power degradation on photovoltaic solar panels. Sustainability 12, 2020, 6416.

[85] del Cueto J.A., Trudell D., Sekulic W., Capabilities of the high voltage stress test system at the outdoor test facility. Presented at the DOE Solar Energy Technologies, NREL/CP-520-38955, 2005.

[86] Taubitz C., Schutze M., Koentopp M.B., Towards a kinetic model of potential-induced shunting. The 27th European Photovoltaic Solar Energy Conference and Exhibition, 2012, 3172-3176.

[87] Taubitz C., Krober M., Schutze M., Koentopp M.B., Kinetic description and modeling of potential induced degradation. The 28th European Photovoltaic Solar Energy Conference and Exhibition, 2013, 3321-3323.

[88] Taubitz C., Schutze M., Krober M., Koentopp M.B., Potential induced degradation: Model calculations and correlation between laboratory tests and outdoor occurrence. The 29th European Photovoltaic Solar Energy Conference and Exhibition, 2014, 2490-2494.

[89] Kajari-Schroder S., Kunze I., Kontges M., Criticality of cracks in PV modules. Energy Procedia 27, 2012, 658-663.

[90] Islam M.A., Hasanuzzaman M., Rahim N.A., A comparative investigation on in-situ and laboratory standard test of the potential induced degradation of crystalline silicon photovoltaic modules. Renewable Energy, 127, 2018, 102-113.

[91] Koentopp M.B., Krober M., Taubitz C., Toward a PID standard: Understanding and modeling of laboratory tests and field progression. IEEE J. Photovoltaics 6(1), 2016, 252-257.

[92] Negel H., Metz A., Wangemann K., Crystalline Si solar cells and modules featuring excellent stability against potential-induced degradation. The 26th European Photovoltaic Solar Energy Conference and Exhibition, 2011, 3107-3122.

[93] Spataru S. V., Sera D., Hacke P., Kerekes T., Teodorescu R., Fault identification in crystalline silicon PV modules by complementary analysis of the light and dark current-voltage characteristics. Prog. Photovolt. Appl. 24, 2015, 517-532.

Acknowledgement

I am blessed and thankful that this research would not have been possible without the support and help of individuals and organizations. I would like to thank you with all sincerity to all of them.

I am indebted to my supervisor, Professor Keiichi Okajima, for guidance, supervision, and support throughout the program. I would like to thank Ms. Tomoko Nishizaki for helping and guidance while I was studying at the Department of Risk Engineering, University of Tsukuba, Tsukuba.

I am also highly indebted to Dr. Yoshihiro Hishikawa for supervision, guidance, and research support. I would like to thank Dr. Masahiro Yoshita for valuable comments on my pre-defense and the final defense, and for supporting my research at the Renewable Energy Research Center, National Institute of Advanced Industrial Science and Technology (AIST), and the staff of the AIST who have helped me in supporting and assistance. Apart from that, the data in this research was supported in part by NEDO under METI.

I would also like to express my highest gratitude to Professor Masayoshi Ishida, Professor Kazuhiko Kato, and Professor Yutaro Akimoto for their valuable comments on my pre-defense and the final defense, which had motivated me to improve my research.

Finally, I would also like to thank the Royal Thai Government for their financial support until the completion, and the King Mongkut's University of Technology Thonburi, Thailand, for my employer.

Publications

Journals

1. Manit Seapan, Yoshihiro Hishikawa., Masahiro Yoshita, Keiichi Okajima, Temperature and irradiance dependences of the current and voltage at maximum power of crystalline silicon PV devices. Solar Energy 204, 2020, pp. 459-465.

2. Manit Seapan, Yoshihiro Hishikawa., Masahiro Yoshita, Keiichi Okajima, Detection of shading effect by using the current and voltage at maximum power point of crystalline silicon PV modules. Solar Energy 211, 2020, pp. 1365-1372.

Peer–reviewed international conference

1. Manit Seapan, Yoshihiro Hishikawa., Masahiro Yoshita, Keiichi Okajima, Detection of cell cracks and increased series resistance of crystalline silicon photovoltaic modules by using voltage and current at maximum power point. Proceedings of 12th International Conference on Applied Energy (ICAE2020), Vol. 9, Part 1, Thailand/Virtual, 2020, pp. 1-4.

International conference

1. Manit Seapan, Yoshihiro Hishikawa., Masahiro Yoshita, Keiichi Okajima, Temperature and Irradiance Dependence of Current and Voltage at Maximum Power of Crystalline Silicon Photovoltaic Modules, The 46th IEEE PVSC, Chicago, IL, USA, June 16-21, 2019, pp. 2583-2587.